

ELECTRONIC RAMAN SPECTROSCOPY

OF IRON DOPED MgO

by

ALAIN POIRIER

A Thesis

submitted to the Faculty of Graduate Studies and Research

in partial fulfilment of the requirements

for the degree of

Doctor of Philosophy

Department of Physics
McGill University
Montreal, Quebec, Canada

© August 1982

ELECTRONIC RAMAN SPECTROSCOPY

OF IRON DOPED MgO

ABSTRACT

The nearby excited states of Fe^{2+} in MgO have been observed by Raman spectroscopy for the first time. We observed an A_{1g} impurity mode (185 cm^{-1}) and an electronic transition at $110.5 \pm .8 \text{ cm}^{-1}$ which we associate with the first excited states of the ferrous ion, Γ_{3g} and Γ_{4g} , previously observed by far infra-red optical absorption.

Crystal field theory and group theory are used to characterize the energy levels and the wavefunctions of the ferrous ion. The observed reduction in the spin-orbit splitting of the energy levels is accounted for by solving the Jahn-Teller Hamiltonian in the approximation of the cluster model.

Uniaxial stress applied to the $\text{MgO}:\text{Fe}^{2+}$ samples produced a shift in the observed electronic transitions. The stress Hamiltonian is solved from which is extracted the experimental value of the strain coupling coefficient to E_g deformation ($V_2 = 7140 \pm 1800 \text{ cm}^{-1}$) which led, ultimately, to the Jahn-Teller coupling coefficients and to the Jahn-Teller energies ($(E_{JT})_E = 80 \text{ cm}^{-1}$, and $3/2(E_{JT})_T = 150 \text{ cm}^{-1}$) pertinent to the ferrous ion in MgO .

RESUME

Les premiers états excités du Fe^{2+} dans le MgO ont été observés par la spectroscopie Raman pour la première fois. Nous observons un mode d'impureté de type A_{1g} (185 cm^{-1}) ainsi qu'une transition électronique à $110.5 \pm .8 \text{ cm}^{-1}$ que nous associons au premier état excité de l'ion ferreux, Γ_{3g} et Γ_{4g} , déjà observé par absorption optique de l'infrarouge lointain.

La théorie du champ cristallin et la théorie des groupes ont été utilisées pour déterminer les niveaux d'énergies et les fonctions d'ondes correspondantes de l'ion ferreux. La séparation réduite des niveaux d'énergies spin-orbit qui est observée s'explique en résolvant l'Hamiltonian Jahn-Teller dans l'approximation du modèle du cluster.

Un stress uniaxial appliqué aux échantillons de $\text{MgO}:\text{Fe}^{2+}$ produit un déplacement des transitions électroniques observées. L'Hamiltonian du stress est résolu; ce qui permet d'extraire la valeur expérimentale du coefficient de couplage aux déformations de type E_g ($V_2 = 7140 \pm 1800 \text{ cm}^{-1}$) ainsi que les coefficients de couplage Jahn-Teller et les énergies Jahn-Teller ($(E_{JT})_E = 80 \text{ cm}^{-1}$ et $3/2 (E_{JT})_T = 150 \text{ cm}^{-1}$) pertinent à l'ion ferreux dans le MgO .

ACKNOWLEDGEMENTS

I wish to express my appreciation to my thesis supervisor, Dr. D. Walsh, for his stimulating guidance and numerous enlightening discussions throughout the course of this work. I wish to thank Dr. L.A. Boatner for providing us with high quality iron doped MgO crystals. I express my gratitude to Mr. J. Auclair, research assistant, and Mr. F. VanGills, technician, for their help and advice. The financial support from NSERC of Canada in the form of a Post Graduate Scholarship, and from McGill University is also acknowledged.

I am grateful for the excellent work done by Miss D. Monton in typing this manuscript.

GLOSSARY

CONSTANTS

Bohr magneton
Boltzmann's constant
Electron charge
Gyromagnetic factor
Mass of electron
Planck's constant
Vacuum permittivity
Vacuum permeability
Velocity of light in vacuum

SYMBOLS

$\beta = -9.2741 \times 10^{-24} \text{ J} \cdot \text{tesla}^{-1}$
 $k = 1.380 \times 10^{-23} \text{ J} \cdot \text{K}^{-1}$
 $e = 1.602 \times 10^{-19} \text{ C}$
 $g_e = 2.0023$
 $m_e = 9.11 \times 10^{-31} \text{ Kg}$
 $h = 6.626 \times 10^{-34} \text{ J} \cdot \text{S}$
 $\epsilon_0 = 8.8542 \times 10^{-12} (\text{A} \cdot \text{S}^2)^2 \cdot \text{kg}^{-1} \cdot \text{m}^{-3}$
 $\mu_0 = 4\pi \times 10^{-7} (\text{A} \cdot \text{S})^{-2} \cdot \text{kg} \cdot \text{m}$
 $c = 2.998 \times 10^8 \text{ m} \cdot \text{s}^{-1}$

UNITS

Angstroms
Centimeter
Coulomb
Electron-volt
Gram
Kelvin (degrees)
Kilogram
Meter
Micrometer
Millimeter
Newton
Photon counts per second

SYMBOLS

$\text{\AA} = 10^{-10} \text{ M}$
 $\text{CM} = 10^{-2} \text{ M}$
 C
 $\text{eV} = 1.6 \times 10^{-19} \text{ J}$
 G
 K
 $\text{KG} = 10^3 \text{ G}$
 M
 $\mu = 10^{-6} \text{ M}$
 $\text{MM} = 10^{-3} \text{ M}$
 $\text{N} = 1 \text{ KG} \cdot \text{M} \cdot \text{S}^{-2}$

UNITS

Pound per square inch

Second

Volt

Wavenumber

TERMS

Acoustic paramagnetic resonance

Aluminum oxide

Collective normal coordinates

Divalent iron

Divalent magnesium

Divalent oxygen

Electron paramagnetic resonance

Ferric oxide

Ham reduction factors

Hamiltonian

Jahn-Teller

JT coupling coefficients

Magnesium oxide

Microwave acoustic attenuation

Mode effective angular frequencies

Mode effective masses

Octahedral symmetry

Orthorhombic symmetry

Spin-orbit parameter

Strain coupling coefficients

SYMBOLS

PSI

S

V

 $\text{CM}^{-1} = 1.240 \times 10^{-4} \text{ eV}$ ABBREVIATIONS

APR

 Al_2O_3 Q_n Fe^{2+} Mg^{2+} O^{2-}

EPR

 Fe_2O_3 $K_E \text{ \& } K_T$

H

JT

 $V_E \text{ \& } V_T$

MgO

MAA

 $\omega_E \text{ \& } \omega_T$ $\mu_E \text{ \& } \mu_T$ O_h D_{2d} λ $V_2 \text{ \& } V_3$

TERMS

Tetragonal symmetry

Trigonal symmetry

Trivalent chromium

ABBREVIATIONS

D_{4h}

D_{3d}

Cr^{3+}

LIST OF FIGURES

<u>FIGURE</u>		<u>PAGE</u>
2-1	The oxygen ions occupy the vertices of an octahedron	11
2-2	$5D$ level is split into $5E_g$ and $5T_{2g}$ levels and spin-orbit energy levels	18
3-1	The different collective displacements Q_N	28
3-2a	Electrons are distributed over five d-orbitals	37
3-2b	The maximum total electron spin distribution $d^4 d\gamma^2$	37
3-3	Two types of molecular bonds are formed	39
3-4	Potential energy surface for $T_{2g} \times e_g$	42
3-5	Four possible distortions of the cluster: $T_{2g} \times t_{2g}$	45
3-6	Relative magnitude of $\gamma(T_2)$, $\gamma(T_1)$ and $\gamma(E)$ for increasing Jahn-Teller coupling strength	48
3-7	The vibronic energy levels for $T_{2g} \times t_{2g}$	61

<u>FIGURE</u>		<u>PAGE</u>
3-8	Calculation by perturbation theory of the shift in the spin-orbit energy levels compared with a direct numerical diagonalization of the energy matrix	66
3-9	Calculation by perturbation theory of the Ham reduction factors compared with a direct numerical diagonalization of the energy matrix	69
3-10	The reduction factors K_E and K_T versus the strength of the Jahn-Teller coupling	71
3-11	Perturbation calculation of the shift in the spin-orbit energy levels	72
3-12	The reduction factors K_E and K_T versus the strength of the Jahn-Teller coupling	74
3-13	Perturbation calculation of the shift in the spin-orbit energy levels	75
3-14	Perturbation calculation of the electronic g-factor versus the strength of the Jahn-Teller coupling for two sets of parameters	76
4-1	Frequency distribution function and projected density of states for phonons in MgO	84
4-2	Schematic of the experimental set-up	86
4-3	Details of the stress apparatus	89
4-4	Pressure sensor calibration	90

FIGUREPAGE

4-5	The Raman scattering of a photon	94
4-6	Allowed Raman transitions for different crystal symmetry	98
4-7	Electronic Raman spectrum of MgO:Fe^{2+} taken at liquid He temperature with 200 mW of laser power (18834 cm^{-1})	100
4-8	Electronic Raman spectrum of MgO:Fe^{2+} under tetragonal stress	106
4-9	Electronic Raman spectrum of MgO:Fe^{2+} under trigonal stress	108
4-10	Electronic Raman spectrum of MgO:Fe^{2+} under orthorhombic stress	110
4-11	Electronic Raman spectrum of MgO:Fe^{2+} under orthorhombic stress	111
5-1	Tetragonal deformation of the octahedron	117
5-2	Trigonal deformation of the octahedron	119
5-3	Orthorhombic deformation of the octahedron	121
5-4	Best fit to the electronic Raman transitions under tetragonal stress	133
5-5	Best fit to the electronic Raman transitions under trigonal stress	136

FIGURE

PAGE

5-6	Best fit to the electronic Raman transitions under orthorhombic stress	138
5-7	Best fit to the electronic Raman transitions under orthorhombic stress	140

TABLE OF CONTENTS

	<u>PAGE</u>
ABSTRACT	iii
ACKNOWLEDGEMENTS	v
GLOSSARY	vi
LIST OF FIGURES	ix
CHAPTER 1	1
INTRODUCTION	
CHAPTER 2	4
ENERGY LEVELS OF THE FERROUS ION	
2.1 The free ion	4
2.1.1 The central field approximation	4
2.1.2 The electron interaction	6
2.1.3 The weak crystalline field case	8
2.2 The crystalline electric field	9
2.2.1 Group theoretical predictions	9
2.2.2 The octahedral electric field	12
2.3 The spin-orbit interaction	19
2.3.1 The spin-orbit Hamiltonian	19
2.3.2 The energy levels and associated functions	22
CHAPTER 3	25
THE JAHN-TELLER EFFECT	
3.1 The electron-phonon coupling	25
3.1.1 The Jahn-Teller theorem	25
3.1.2 The quasi-molecular model	26
3.1.3 The Jahn-Teller Hamiltonian	31
3.2 The weak Jahn-Teller effect	36
3.2.1 The molecular orbitals	36
3.2.2 $T_{2g} \times e_g$	38
3.2.3 $T_{2g} \times t_{2g}$	44
3.2.4 $T_{2g} \times (e_g + t_{2g})$	46
3.3 The experimental evidences	49
3.3.1 The orbital reduction factors	50
3.3.2 The Ham reduction factors	52
3.3.3 The g-factor	57
3.4 Calculations by perturbation theory	59
3.4.1 The vibronic functions	59
3.4.2 The reduction in the spin-orbit splitting	63
3.4.3 Reduced Ham factors	67

	<u>PAGE</u>
CHAPTER 4	THE EXPERIMENTAL RESULTS
4.1	The literature review 77
4.1.1	The direct evidence 77
4.1.2	The inferred evidence 79
4.1.3	The vibrational spectrum of MgO crystal 81
4.1.4	The g-factor 83
4.2	The experimental set-up 85
4.2.1	The Raman system 85
4.2.2	The stress apparatus 88
4.2.3	The iron doped MgO samples 91
4.3	The electronic Raman effect 93
4.3.1	The scattering tensor 93
4.3.2	Selection rules and symmetry of the transitions 97
4.4	The Raman spectrum of iron doped MgO crystal 99
4.4.1	The electronic Raman transition 99
4.4.2	The electronic Raman transitions under uniaxial stress 104
CHAPTER 5	THE UNIAXIAL STRESS
5.1	Ham's phenomenological approach 112
5.1.1	The strain components 112
5.1.2	The stress Hamiltonian 122
5.1.3	The effect of uniaxial stress 125
5.2	The interpretation of the experimental results 128
5.2.1	The procedure 128
5.2.2	The fit to the experimental results 132
CHAPTER 6	CONCLUSION 151
APPENDIX A	154
APPENDIX B	156
APPENDIX C	158
APPENDIX D	160
APPENDIX E	162
APPENDIX F	165
REFERENCES	171

CHAPTER 1

INTRODUCTION

Since the discovery of the laser in 1960, the field of spectroscopy has improved greatly in the refinements of techniques and in the wealth of applications. One of these, Raman spectroscopy, has attracted physicists again as a result of the high photon density achieved by a laser, making possible the detection of very weak Raman signals via photon-counting equipment. Nowadays, Raman spectroscopy provides a powerful tool to study electronic energy levels and vibrational states of atoms and molecules, and complements infrared spectroscopy whose transition selection rules are different.

In this thesis, we apply electronic Raman spectroscopy to the study of a transition metal ion, the ferrous ion, substituting for divalent magnesium ion in single crystals of MgO. The $\text{MgO}:\text{Fe}^{2+}$ complex presents a good example of a dynamical Jahn-Teller (JT) effect, i.e., the electron-phonon coupling at the ferrous ion site reduces the electronic orbital angular momentum leading to a reduced spin-orbit splitting of the energy levels and a reduced electronic g-factor. By applying different uniaxial stresses to the $\text{MgO}:\text{Fe}^{2+}$ samples, we can determine the strain coupling coefficients which lead to the JT coupling coefficients and the corresponding JT energies. Existing and future theories pertinent to this JT

problem rely on accurate experimental values of these coefficients. In spite of many efforts over recent years, in the field of Raman spectroscopy, no electronic transitions for MgO:Fe^{2+} have been reported.

In the following chapter, the reader is introduced to crystal field theory and to some basic applications of group theory. Explicit calculations show how the combined effect of electron-electron interactions, ligand-electron and spin-orbit interactions lead from the free ion energy levels to the spin-orbit energy levels and the corresponding wavefunctions. These results are essential to solve the JT Hamiltonian and the stress Hamiltonian as will be shown in chapters 3 and 5.

The concept of a JT effect, the different types of JT coupling and the JT Hamiltonian are discussed in chapter 3. Calculations are explicitly carried out which demonstrate the expected reduction in the spin-orbit splitting and the electronic g-factor due to the dynamical JT effect. Particularly, the Ham reduction factors are presented in a new way which emphasises their origin and the necessity of such coefficients.

The literature review of the most important research of the MgO:Fe^{2+} complex is given in chapter 4. A description of the experimental set-up together with information relative to the MgO samples and their preparation for the stress experiment is also given. The theory and concept of Raman spectro-

copy is introduced and the experimental Raman spectra of the MgO:Fe^{2+} samples taken at liquid He temperature with and without uniaxial stress are presented.

In chapter 5, the theory and concept of stress and strain is established leading to an expression for the stress Hamiltonian. The splitting of the energy levels for increasing stress are explicitly calculated and fitted to the experimental data. The interpretation of the experimental results follows.

The last chapter summarizes the research presented in this thesis. The salient results are the value of the strain coupling coefficient to E_g deformations, i.e., V_2 , the corresponding JT coupling coefficients and JT energies, i.e. $(E_{JT})_E$ and $(E_{JT})_T$.

Any calculations or information relevant to the completeness of the thesis but not essential to the logical development of the thesis have been relegated to the appendices.

CHAPTER 2

Energy levels of the ferrous ion

2.1 The free ion

2.1.1 The central field approximation

The ferrous ion is considered as a point nucleus of charge $+Ze$ surrounded by N electrons, each of mass M and charge $-e$. For the case of $MgO:Fe^{2+}$, the ferrous ion replaces Mg^{2+} in the crystal lattice of MgO and interacts with its surrounding neighbors. The Hamiltonian of such a system is

$$H = -\frac{\hbar^2}{2m} \sum_{i=1}^N \Delta_i - \sum_{i=1}^N \frac{Ze^2}{r_i} + \frac{1}{2} \sum_{i \neq j}^N \frac{e^2}{r_{ij}} + \sum_{i=1}^N V(r_i) + \sum_{i=1}^N H_{so}^{(i)} \quad (2.1-1)$$

where the different energies involved are defined to be

$-\frac{\hbar^2 \Delta_i}{2m}$ the kinetic energy of the i^{th} electron;

$-\frac{Ze^2}{r_i}$ the Coulomb energy of interaction between the nucleus and the i^{th} electron;

$\frac{e^2}{r_{ij}}$ the Coulomb energy of interaction between the i^{th} and j^{th} electron;

$V(r_i)$ the Coulomb energy of interaction between the i^{th} electron and the ligand;

$H_{so}^{(i)}$ the energy of the spin-orbit interaction of the i^{th} electron.

To obtain the energy levels of the system, the Schrödinger equation

$$H\Phi = E\Phi \tag{2.1-2}$$

must be solved for E . Due to the complexity of the interactions, the Schrödinger equation, Eq. (2.1-2), cannot be solved analytically for $N > 1$. Therefore, we have to make simplifying assumptions that will take into account the relative magnitude of the energy terms in Eq. (2.1-1). The first such simplification is the central field approximation which is known in the literature as the Slater theory of atoms and ions.

The electron-electron interaction in Eq. (2.1-1) prevents a separation of the variables in the Schrödinger equation. This constraint may be relaxed if we separate the total Hamiltonian, Eq. (2.1-1), into two parts assuming that an electron, moving around the ion, feels a potential that can be approximately reproduced by a function $-U(r_i)/e$. In doing so, we neglect the spin-orbit interaction and the electron-ligand interaction for simplicity. This approximation will be justified in subsection 2.1.2. The Hamiltonian,

within the central-field approximation, can be written as

$$H = H_0 + H_1 \quad (2.1-3)$$

where

$$H_0 = \sum_{i=1}^N \left(\frac{-\hbar^2}{2m} \Delta_i + U(r_i) \right)$$

$$H_1 = \sum_{i=1}^N \left(\frac{-Ze^2}{r_i} - U(r_i) \right) + \frac{1}{2} \sum_{i \neq j}^N \frac{e^2}{r_{ij}}$$

Now we can solve the simpler Schrödinger equation obtained by replacing H for H_0 in Eq. (2.1-2), i.e.,

$$H_0 \Phi = E_0 \Phi \quad (2.1-4)$$

The Schrödinger equation, Eq. (2.1-4), can be separated into one-electron equations by choosing Φ as a product of one-electron functions and E_0 as a sum of one-electron energies. The resulting one-electron Schrödinger equation differs from its equivalent expression for the hydrogen atom by the potential $-U(r_i)/e$ substituting for $-e^2/r$. Consequently, the one-electron functions can be expressed in the same form as hydrogenic functions differing mainly by the radial part which depends on the central potential $U(r)$. Thus, the one-electron functions can be written as

$$\Phi(nlm_l) = R_{nl}(r) Y_{lm_l}(\theta, \varphi) \quad (2.1-5)$$

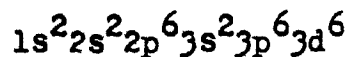
where the radial part is $R_{nl}(r)$ and the angular part is given in term of the well-known spherical harmonics $Y_{lm_l}(\theta, \varphi)$. We must account for the spin of the electrons by multiplying the N orbital functions by N spin functions. Because of the Pauli exclusion principle and the fact that two electrons cannot be distinguished, the product of N one-electron functions and their corresponding spin functions must be antisymmetrised.

The resulting functions, which are still solutions of the Schrödinger equation, are given by the famous Slater determinantal functions whose general expression is given by

$$\Psi = (N!)^{-1/2} \sum_P (-1)^P P \prod_{i=1}^N \Phi_i(n_i | m_i, m_s)$$

where P is a permutation operator which simultaneously interchanges the spatial and spin coordinates of any pair of electrons; p is the parity of the permutation.

For the ferrous ion, the energies E_0 , Eq. (2.1-4), are degenerate with respect to m_l and m_s , the projection along the z-axis of the orbital and spin angular momentum, respectively, but not with respect to the angular momentum itself. The different energies E_0 can be distinguished by what is called the electronic configuration



written more simply $3d^6$ for the ferrous ion. There exists 210 determinantal functions which describe the states available to the six 3d-electrons implying that $E_0(3d)$ is also 210-fold degenerate.

2.1.2 The electron interaction

We are interested in the $3d^6$ configuration in which all but the six 3d-electrons are in closed shells. These six 3d-electrons are responsible for most of the chemical and physical properties of the ferrous ion. So, we are concerned in characterizing their available states, the corresponding energies and wave functions.

The degeneracy of $E_0(3d)$ can be lifted if we account for the electron-electron interaction by solving the perturbation potential H_1 , Eq. (2.1-3). The first summation in H_1 simply shifts the unperturbed energy $E_0(3d)$ and the second summation involving the distance between two electrons (r_{ij}) correlates the electrons and splits the unperturbed energy. In fact, we define

$$H' = \frac{1}{2} \sum_{ij}^N \frac{e^2}{r_{ij}} \quad (2.1-6)$$

which commutes with the total orbital angular momentum L and the total spin angular momentum S (see Appendix A). Using states which are linear combinations of determinantal functions labeled by the quantum numbers $LSM_L M_S$, it is shown in Appendix A that the matrix elements of H' vanish if the following conditions are satisfied for the $|LSM_L M_S\rangle$ states when calculating the matrix elements of H' ,

$$M_L \neq M'_L$$

$$L \neq L'$$

$$M_S \neq M'_S$$

$$S \neq S'$$

Moreover, the matrix elements of H' are also independent of M_L and M_S . Therefore, the secular determinant of the electron-electron interaction breaks up into smaller determinants each labeled by a pair of quantum numbers LS and are $(2L+1)(2S+1)$ -fold degenerate. The resulting energy levels are designated by what is called a term, $2S+1L$. Usually, the three Hund's rules are used to classify empirically in an increasing order

of magnitude these free ion energy levels. For the ferrous ion, Hund's rules are unapplicable except for the ground state, 5D , the least energetic levels (or terms) being:

5D	(0 cm^{-1})
3H 3P 3F 3G	(20000 cm^{-1})
1I 3D 1G	(30000 cm^{-1})
etc.	(2.1-7)

2.1.3 The weak crystalline field case

So far, we have neglected electron-ligand interaction and spin-orbit interaction in the total Hamiltonian, Eq. (2.1-1). This fact can be understood since the ferrous ion belongs to the transition metal series among which elements two cases can be distinguished with regard to the relative magnitude of the energy terms of the total Hamiltonian. The two cases are

(i) the strong crystalline field case,

$$\sum_I V(r_i) > \frac{1}{2} \sum_{i,j}^N \frac{e^2}{r_{ij}} > \sum_{i=1}^N H_{so}(i)$$

(ii) The weak crystalline field case,

$$\frac{1}{2} \sum_{i,j}^N \frac{e^2}{r_{ij}} > \sum_I V(r_i) > \sum_{i=1}^N H_{so}(i)$$

For the first transition metal series, to which the ferrous ion belongs, the electron-electron interaction and electron-ligand interaction are of the same order of magnitude. Consequently, the first transition metal series cannot be unambiguously attributed to case (i) or (ii), whereas the second and third transition metal series definitely belong

to case (i). Calculations and experimental results have shown, however, that the ferrous ion energy levels are well described by case (ii). Therefore, we were perfectly allowed in this section to treat the ferrous ion as a free ion. In the subsequent sections, the electron-ligand interaction and spin-orbit interaction are accounted for sequentially using perturbation theory.

2.2 The crystalline electric field

2.2.1 Group theoretical predictions

When the ferrous ion is embedded in the MgO crystal, i.e., Fe^{2+} substitutes for Mg^{2+} , the ferrous ion can no longer be considered as a free ion. In fact, the ion interacts with its surrounding neighbors, the ligands, through Coulomb interaction. In $\text{MgO}:\text{Fe}^{2+}$, the ferrous ion is surrounded by six oxygens ions (ligands) forming ionic bonds with them. We are interested in the changes the electronic system of the central ion (Fe^{2+}) undergoes under the influence of the electric field produced by the ligands. We assume the Coulomb energy of the interaction between the i^{th} electron of the central ion and the ligands to be more important than the spin-orbit interaction of the i^{th} electron, according to subsection 2.1.3.

The ligands generate an inhomogeneous electric field that destroys the isotropy of the previously free ion. Hence, the symmetry group is reduced from that of the full three-

dimensional group plus inversion (spherical) to the subgroup associated with the ligands configuration: The reduction in dimensionality of the irreducible representation causes the degeneracy associated with the full spherical symmetry to be lifted. In fact, the oxygen ions occupy the vertices of an octahedron, Fig. 2.1, the ferrous ion being at the center, hence lowering the site symmetry from spherical to octahedral (O_h). Moreover, from group theory, we know the highest irreducible representation dimensionality of O_h symmetry is three (four for ions having odd number of electrons). The crystalline electric field affects only the motion of the electrons, i.e., operates on the orbital part of the wave functions and not on the spin part of the wave functions. Since the orbital degeneracy of the ground state (5D) is five, which does not exist under O_h symmetry, the ground state of the ferrous ion must split. We can decompose the D-states into a linear combination of states that will transform according to the irreducible representations of O_h , i.e.,

$$^5D = ^5E_g + ^5T_{2g}$$

where the subscript "g" signifies that the states are even under inversion. Such a decomposition implies that the ground state splits into a two-fold degenerate orbital state (5E_g) of effective orbital angular momentum¹ $L = 1/2$, and into a three-fold degenerate orbital state ($^5T_{2g}$) of effective orbital angular momentum¹ $L = 1$. The spin degeneracy is not affected by the decomposition. We notice that the effect of

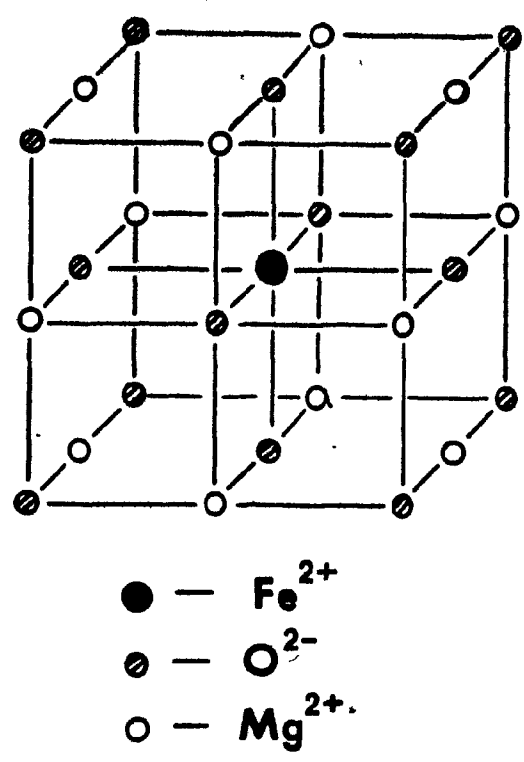


Fig. 2-1

The oxygen ions occupy the vertices of an octahedron surrounding the ferrous ion impurity in the MgO crystal.

the crystal field is to partially reduce the orbital angular momentum in the E_g states and T_{2g} states. In fact, the effective orbital angular momentum is obtained by taking the submatrices of L_x , L_y and L_z in the E_g states and T_{2g} states. For example, the submatrix of the components of L in the T_{2g} states is identical to the corresponding matrices in the P states except each matrix element is multiplied by -1 , yielding $L = -1$. Formally, the Wigner-Eckart theorem can be used to obtain the constant of proportionality between the matrix elements of the orbital angular momentum in the D -states and the matrix elements in a subspace of the D -states.

Group theory indicates kindly that the 5D ground state must split, but does not specify which way it splits and the magnitude of the splitting. To obtain this information, we rely on ligand field theory². In this thesis, the Mulliken notation is employed to label the orbital states and the Bethe notation to label the spin-orbit states. The notations are specified in Table 2.1.

2.2.2 The octahedral electric field

In order to find out which way the ground state splits and the corresponding splitting, we must find an expression for the Coulomb energy of the interaction between the i^{th} electron and the ligands. Assuming a spatial charge distribution $\rho(\vec{R})$ for a given ligand ion, e.g. O^{2-} , we obtain the wanted expression for the Coulomb energy directly from

OCTAHEDRAL SYMMETRY O_h				
MULLIKEN NOTATION	BETHE NOTATION	IDENTITY	INVERSION	BASIS FUNCTIONS
A_{1g}	Γ_{1g}	1	1	$x^2+y^2+z^2$
A_{2g}	Γ_{2g}	1	1	$(x^2-y^2)(y^2-z^2)(z^2-x^2)$
E_g	Γ_{3g}	2	2	$(2z^2-x^2-y^2), \sqrt{3}(x^2-y^2)$
T_{1g}	Γ_{4g}	3	3	S_x, S_y, S_z
T_{2g}	Γ_{5g}	3	3	YZ, XZ, XY
A_{1u}	Γ_{1u}	1	-1	$\Gamma_{2g} \times \Gamma_{2u}$
A_{2u}	Γ_{2u}	1	-1	XYZ
E_u	Γ_{3u}	2	-2	$\Gamma_{3g} \times \Gamma_{2u}$
T_{1u}	Γ_{4u}	3	-3	X, Y, Z
T_{2u}	Γ_{5u}	3	-3	$\Gamma_{5g} \times \Gamma_{1u}$

TABLE 2.1

the classical electrostatic potential

$$\begin{aligned} V(\bar{r}_i) &= \sum_k q_k V'(\bar{r}_i) \\ V'(\bar{r}_i) &= \int \frac{\rho(\bar{R}) d\tau_R}{|\bar{R}-\bar{r}|} \end{aligned} \quad (2.2-1)$$

where \bar{R} is a vector pointing from the central ion (Fe^{2+}) to a point having $\rho(\bar{R})$ at (R, Θ, Φ) and \bar{r} is a vector locating the electron at (r, θ, φ) . Using the well-known expansion in spherical harmonics,

$$\frac{1}{|\bar{R}-\bar{r}|} = \sum_{\lambda=0}^{\infty} \frac{4\pi}{2\lambda+1} \frac{r_{<}^{\lambda}}{r_{>}^{\lambda+1}} \sum_{x=-\lambda}^{\lambda} Y_{\lambda,x}(\theta, \varphi) Y_{\lambda,x}^*(\Theta, \Phi)$$

we can write the electrostatic potential as,

$$V'(\bar{r}_i) = \sum_{\lambda=0}^{\infty} \sum_{x=-\lambda}^{\lambda} \left[\frac{4\pi}{2\lambda+1} \int \frac{\rho(\bar{R})}{R^{\lambda+1}} Y_{\lambda,x}^*(\Theta, \Phi) d\tau_R \right] r^{\lambda} Y_{\lambda,x}(\theta, \varphi) \quad (2.2-2)$$

where $r_{<} = r$ and $r_{>} = R$ since MgO is an ionic crystal. Obviously $V'(\bar{r})$ will have the same symmetry as $\rho(\bar{R})$, i.e., the octahedral symmetry, Fig. 2.1. The effect of $V'(\bar{r})$ on the energy levels of the free ferrous ion is obtained by perturbation theory to first order. The calculations involve integrals of the form,

$$\langle \varphi_i | \sum_k V(r_k) | \varphi_j \rangle$$

where φ_i is a product of one-electron functions which we use because $V(r_k)$ is a one-electron operator. Consequently, the matrix elements of the electrostatic potential are proportional to a sum of one-electron terms involving three spherical harmonics which are functions of the electron coordinates. Because of these spherical harmonics, the matrix elements will

be zero unless certain conditions of symmetry are satisfied. The imposition of these conditions will considerably reduce the number of terms in the expansion of the electrostatic potential, Eq. (2.2-2), and will make the calculations tractable.

The addition theorem for spherical harmonics states that this product of spherical harmonics is non-zero if $\lambda \leq 2L$, where $L = 2$ for 3d-electrons. Moreover, from parity considerations, λ must be even and we obtain the restrictions,

$$\lambda = 0, 2, 4 \quad (2.2-3)$$

Besides, the electrostatic potential must be invariant for all symmetry operations which belongs to O_h . The first invariance requirement concerns a rotation of the coordinate system by $\pi/2$ about a four-fold symmetry axis, i.e.

$$C_4 V'(r) = V'(r) \quad (2.2-4)$$

This invariance requirement restricts the λ values to $\pm 4n$, in Eq. (2.2-2), where n is a positive integer (including zero). Moreover, a mirror reflexion in the XZ-plane must leave $V'(\vec{r})$ unchanged, i.e.,

$$\sigma_{XZ} V'(r) = V'(r) \quad (2.2-5)$$

This condition imposes that $A_{4,4} = A_{4,-4}$ where,

$$A_{\lambda,\lambda} = \frac{4\pi}{2\lambda+1} \int \frac{\rho(R)}{R^{\lambda+1}} Y_{\lambda,\lambda}^*(\Theta,\Phi) d\tau_R \quad (2.2-6)$$

Finally, a rotation of the coordinate system by $2\pi/3$ about the three-fold axis of the octahedron must bring $V'(r)$ into itself, i.e.,

$$C_3 V'(r) = V'(r) \quad (2.2-7)$$

which implies that $A_{2,0} = 0$ and $A_{4,4} = \sqrt{\frac{5}{14}} A_{4,0}$.

Owing to the constraints, Eq. (2.2-3) to Eq. (2.2-5) and Eq. (2.2-7), the expression for the electrostatic potential, Eq. (2.2-2), can be simplified to

$$V'_{Oh}(\vec{r}) = A_{00}Y_{00} + A_{40}r^4 \left[Y_{40} + \sqrt{\frac{5}{14}} (Y_{4,4} + Y_{4,-4}) \right]$$

In order to get an explicit expression for $V'_{Oh}(r)$, it is usual to approximate the ligand charge distribution to point charge. Therefore, the k^{th} ligand has a charge $-q_k$ and the coordinates (R_k, Θ_k, Φ_k) so that we can rewrite Eq. (2.2-6) as,

$$A_{\lambda,x} = \frac{4\pi}{2\lambda+1} \sum_k \frac{-q_k}{R_k^{\lambda+1}} Y_{\lambda,x}^*(\Theta_k, \Phi_k) \quad (2.2-8)$$

For the case of $\text{MgO}:\text{Fe}^{2+}$, all the ligands have the same charge (or $-q$) and the same distance from the central ion (R). Thus, in the point charge approximation, the electrostatic potential can be expressed as,

$$V''_{Oh}(r) = \frac{3}{\sqrt{\pi}} a_0 Y_{00} + \frac{21}{4\sqrt{\pi}} a_4 r^4 \left[Y_{40} + \sqrt{\frac{5}{14}} (Y_{4,4} + Y_{4,-4}) \right]$$

where $a_0 = -4\pi q/R$ and $a_4 = -4\pi q/9R^5$.

Once again, we rely on perturbation theory to obtain the effect of the ligand field on the energy levels of the 5D ground state. The work is simplified by the choice of appropriate wave functions which are symmetry adapted linear combinations of one-electron 3d-wave functions, Eq. (2.1-6). These wave functions must transform the same way as the states they describe. Since the ground state is orbitally five-fold degenerate, we look for five such wave functions which will

give rise to E_g states and T_{2g} states. The wave functions³ are,

$$\Psi(^5E_{g\theta}) = R_{3d}(r) Y_{20}(\theta, \varphi) \quad (2.2-9a)$$

$$\Psi(^5E_{g\epsilon}) = R_{3d}(r) \cdot 1/\sqrt{2} [Y_{22}(\theta, \varphi) + Y_{2-2}(\theta, \varphi)] \quad (2.2-9b)$$

$$\Psi(^5T_{2g\xi}) = R_{3d}(r) \cdot 1/\sqrt{2} [Y_{21}(\theta, \varphi) + Y_{2-1}(\theta, \varphi)] \quad (2.2-9c)$$

$$\Psi(^5T_{2g\eta}) = R_{3d}(r) \cdot 1/\sqrt{2} [Y_{21}(\theta, \varphi) - Y_{2-1}(\theta, \varphi)] \quad (2.2-9d)$$

$$\Psi(^5T_{2g\zeta}) = R_{3d}(r) \cdot 1/\sqrt{2} [Y_{22}(\theta, \varphi) - Y_{2-2}(\theta, \varphi)] \quad (2.2-9e)$$

Using wave functions, we can easily carry on the perturbation calculations and, according to group theoretical predictions, we find out that the 5D ground state is split with the $^5T_{2g}$ states lowest, Fig. 2.2. The energy separation between the 5E_g states and $^5T_{2g}$ states is defined as,

$$\Delta = 10 Dq = \frac{-5A_{40}}{7\sqrt{\pi}} \langle r^4 \rangle \quad (2.2-10)$$

Dq is a parameter frequently used in ligand field theory to estimate the strength of the electrostatic potential or ligand field. In fact, an experimental estimate for Dq can be obtained from the separation of the ion spectral lines which, when substituted in the previous equations, compensate for the point charge approximation.

Tanabe and Sugano⁴ calculated the effect of crystalline electric field of octahedral symmetry on the free ion energy levels of $3d^N$ configuration. Their diagrams give the distribution of energy levels relative to the ground state as a function of Dq/B , where B is one of Racah parameters³. For the case of $MgO:Fe^{2+}$, it has been determined experimentally⁴

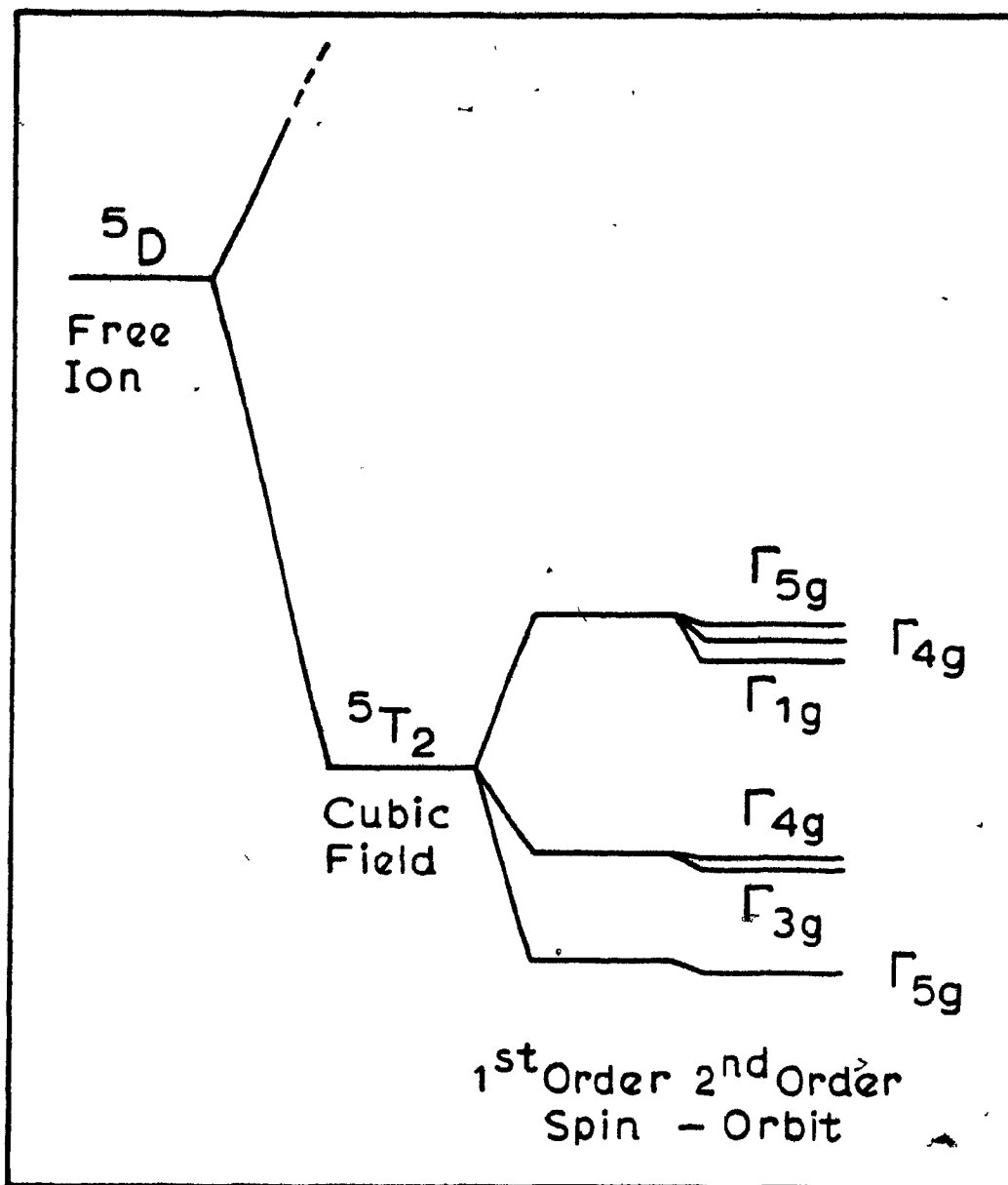


Fig. 2-2

Expected energy levels according to crystal field theory for $3d^6$ ion (Fe^{2+}).

that $Dq = 934 \text{ cm}^{-1}$ and $B = 917 \text{ cm}^{-1}$. These values determine the relative energies of the split components for the terms ($2S+1L$), Eq. (2.1-8), via Tanabe and Sugano diagram⁹ for $3d^6$ ions.

2.3 The spin-orbit interaction

2.3.1 The spin-orbit Hamiltonian

Up to now, we have neglected the spin angular momentum of individual electrons, according to the weak field case, subsection 2.1.3. In fact, this means that we have treated the problem non-relativistically. Relativistic corrections can be made using Dirac's equation for an electron moving in the potential $U'(r)$ of the nucleus. The electron moving in the electrostatic field of the nucleus, given by

$$\vec{E} = -\frac{1}{q} \frac{dU'(r)}{dr} \frac{\vec{r}}{r} \quad (2.3-1)$$

will feel, in its own frame of reference, a magnetic field

$$\vec{B} = \frac{-1}{c^2} \cdot \vec{v} \times \vec{E} \quad (2.3-2)$$

which interacts with the electron intrinsic magnetic moment

$$M_s = \frac{qS}{m_e} \quad (2.3-3)$$

where \vec{v} is the speed of the electron (small compared with the speed of light), q and m_e are the charge and the mass of the electron, respectively. Thus, we can rewrite the magnetic field, Eq. (2.3-2), using equation (2.3-1),

$$\vec{B} = \frac{1}{qc^2} \frac{1}{r} \frac{dU'(r)}{dr} \frac{\vec{p} \times \vec{r}}{m_e}$$

where $\vec{v} = \vec{p}/m_e$ has been used. The spin-orbit Hamiltonian is

expressed as

$$\begin{aligned} H_{so} &= -M_s B \\ &= \frac{1}{m_e c^2} \frac{1}{r} \frac{dU(r)}{dr} \bar{L} \cdot \bar{S} \end{aligned} \quad (2.3-4)$$

where $\bar{p} \times \bar{r} = -\bar{L}$, the orbital angular momentum, has been used. A summation over all the electrons of the central ion results in the well-known Russell-Saunders coupling expressed as

$$\sum_{i=1}^N H_{so}(i) = \sum_{i=1}^N \xi(r_i) \bar{L}_i \cdot \bar{S}_i \quad (2.3-5)$$

where we use the definition⁵

$$\xi(r_i) = \frac{1}{m_e c^2} \frac{1}{r_i} \left. \frac{dU(r)}{dr} \right|_{r=r_i}$$

Equation (2.3-5) can be written in operator equivalent form as

$$\sum_i H_{so}(i) = -\lambda \mathbf{L} \cdot \mathbf{S} \quad (2.3-6)$$

where L is the total effective orbital angular momentum for $5T_{2g}$ states, S is the total spin angular momentum and λ is the spin-orbit coupling parameter which is equal to its free ion value given by

$$\lambda = -\frac{1}{4} \int R_{3d}(r) \xi(r) R_{3d}(r) dr \quad (2.3-7)$$

For the ferrous ion, the accepted value⁶ $\lambda = -100 \text{ cm}^{-1}$ is affected by spin-orbit interaction to distant terms with $S = 1$, Eq. (2.1-7), by any expansion of the electron orbitals ($R_{3d}(r)$) and by covalency effect. We follow Ham in neglecting all these effects, but covalency effect which will be accounted for in chapter 3. A negative sign is assumed for the spin-orbit coupling parameter if the ion has a shell which is more than half-filled as is the case for $3d^6$ ions.

We must also account for spin-orbit interaction between ${}^5T_{2g}$ states and 5E_g states by second-order perturbation theory, and for the slightly weaker spin-spin interaction. Both are represented by the operator equivalent^{7,8}

$$\xi (L \cdot S) + \mu (L \cdot S)^2 + \rho (L_x^2 S_x^2 + L_y^2 S_y^2 + L_z^2 S_z^2) \quad (2.3-8)$$

The parameters ξ, μ, ρ (including the effect of spin-spin interaction) are given to the accuracy of second-order perturbation theory^{7,8} by,

$$\xi = -2 \text{ cm}^{-1}$$

$$\mu = -2 \text{ cm}^{-1}$$

$$\rho = +6 \text{ cm}^{-1}$$

The total spin-orbit Hamiltonian, Eq. (2.3-6) and Eq. (2.3-7), can be written in the operator equivalent form,

$$H_{so}({}^5T_{2g}) = \xi (L \cdot S) + \mu (L \cdot S)^2 + \rho \left\{ L_z^2 S_z^2 + \frac{1}{8} ([L_+^2 + L_-^2] [S_+^2 + S_-^2] + [L_+ L_- + L_- L_+] \cdot [S_+ S_- + S_- S_+]) \right\}$$

where $\xi = \xi - \lambda$. We have used the raising and lowering operators defined as,

$$L_{\pm} = L_x \pm i L_y$$

$$S_{\pm} = S_x \pm i S_y$$

Before we solve the secular equation for the spin-orbit interaction, it is instructive to analyse the group theoretical predictions for an orbital state (T_{2g}) coupled to a spin state ($S = 2$). Evidently, the resulting ${}^5T_{2g}$ states are fifteen-fold degenerate which is not allowed for octahedral symmetry since the highest irreducible representation (for ions with even

number of electrons) has a dimensionality of three. Therefore, we must decompose the ${}^5T_{2g}$ reducible representation into the irreducible representations of O_h using Koster's⁹ multiplication table. In doing so, we obtain the splitting of the ${}^5T_{2g}$ states under the effect of spin-orbit interaction. The following decomposition results

$$\Gamma_{5g} \times \Gamma(S=2) = \Gamma_{1g} + \Gamma_{3g} + 2\Gamma_{4g} + 2\Gamma_{5g}$$

The Bethe notation, Table 2.1, is used for spin-orbit states. Table 2.1 also gives the degeneracy of these irreducible representations of O_h and indicates the transformation properties of the spin-orbit states in terms of the coordinates x, y, z and various bilinear combinations of the coordinates. Therefore, group theory predicts that the spin-orbit Hamiltonian Eq. (2.3-8), splits the ${}^5T_{2g}$ states into six sets of states (or energy levels).

2.3.2 The energy levels and associated functions

The spin states must be coupled explicitly to the T_{2g} states, Eq. (2.2-9c) to Eq. (2.2-9e), to give the fifteen spinors

$$\left[|T_{2g}\xi; m_s\rangle, |T_{2g}\eta; m_s\rangle, |T_{2g}\zeta; m_s\rangle \right] \quad (2.3-9)$$

where $s = -2, -1, 0, 1, 2$. We can solve the secular equation resulting from the matrix representation of $H_{so}({}^5T_{2g})$ using the spinors defined in (2.3-9). After a lengthy but simple calculation we obtain the eigenvalues (energy levels) regrouped according to their $J = L + S$ values, i.e.,

$$J = 1: \quad E(a\Gamma_5) = -3\xi + 9\mu + \frac{27}{5}\rho \quad (2.3-10a)$$

$$J = 2: \quad E(\Gamma_3) = -\xi + \mu + 2\rho \quad (2.3-10b)$$

$$E(a\Gamma_4) = -\xi + \mu + 3\rho \quad (2.3-10c)$$

$$J = 3: \quad E(\Gamma_1) = 2\xi + 4\mu + 2\rho \quad (2.3-10d)$$

$$E(b\Gamma_4) = 2\xi + 4\mu + 4\rho \quad (2.3-10e)$$

$$E(b\Gamma_5) = 2\xi + 4\mu + \frac{28}{5}\rho \quad (2.3-10f)$$

where the energy levels are labeled as $E(\Gamma_i)$ according to the representation of the state. The degeneracies are the same as the irreducible representation that labels the state and indicates its transformation properties. So, these results corroborate the group theoretical predictions and represent the crystal field predictions for the spin-orbit energy levels, Fig. 2.2.

By infrared optical absorption or as shown in this thesis by Raman spectroscopy, it is possible to observe electronic transitions among some of these spin-orbit levels. Consequently, the energy of the expected transitions, as predicted by crystal field theory, are:

$$E(\Gamma_3) - E(a\Gamma_5) = 192 \text{ cm}^{-1} \quad (2.3-11a)$$

$$E(a\Gamma_4) - E(a\Gamma_5) = 198 \text{ cm}^{-1} \quad (2.3-11b)$$

$$E(\Gamma_1) - E(a\Gamma_5) = 480 \text{ cm}^{-1} \quad (2.3-11c)$$

$$E(b\Gamma_4) - E(a\Gamma_5) = 492 \text{ cm}^{-1} \quad (2.3-11d)$$

$$E(b\Gamma_5) - E(a\Gamma_5) = 501 \text{ cm}^{-1} \quad (2.3-11e)$$

The corresponding normalized eigenfunctions are listed in Appendix B. They differ in a few respects from the published functions being linear combinations of them.

Figure 2.2 summarizes the effect of the crystalline electric field and the spin-orbit interaction on the 5D ground state of the free ion, according to crystal field theory² and perturbation theory.

CHAPTER 3

The Jahn-Teller effect

3.1 The electron-phonon coupling

3.1.1 The Jahn-Teller theorem

It is usual, as we did in chapter 2, to consider the motion of the electrons and the nucleus of an atom to be decoupled. Owing to their smaller mass, the electrons move much faster than the nucleus, so that the electrons rearrange themselves adiabatically around the nucleus for any displacement of the nucleus. This is the Born-Oppenheimer¹⁰ approximation for non-degenerate states, and the corresponding Born-Oppenheimer product state is represented by a direct product of a purely electronic function and a vibrational function.

In 1937, Jahn and Teller¹¹ established, for non-linear molecules with an orbitally degenerate ground state, that a molecule would spontaneously distort in order to lower its symmetry and, in so doing, would lift the degeneracy of its ground state and attain a new equilibrium state. The next year, Jahn¹² extended the theorem to include spin effects showing that a molecule would spontaneously distort if the ground state has a degeneracy other than Kramers degeneracy: this is the Jahn-Teller (JT) theorem.

Due to the presence of phonons, the crystal lattice is not a rigid entity as we assumed in chapter 2. Since the strength and symmetry of the crystalline electric field depend on the central ion-ligand configuration, we expect interesting effects to occur to the electronic energy levels from the relative motion of the ligands and the central ion. In 1939, Van Vleck^{13,14} adapted the Jahn-Teller theorem to the paramagnetic impurities in crystals having a degenerate ground state. He showed that the impurity's environment would distort with no more than the zero point amplitude of a typical vibration mode being necessary to reach a new nuclear configuration of lower symmetry and lower energy. Consequently, when the coupled motion of electrons and nucleus is no longer negligible, which occurs for ions with degenerate ground states other than Kramer states, the Born-Oppenheimer approximation breaks down and the JT effect appears - a direct consequence of the JT theorem.

3.1.2 The quasi-molecular model

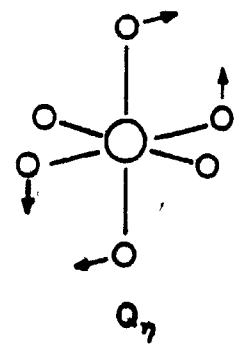
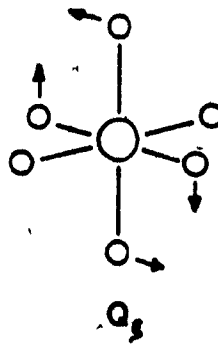
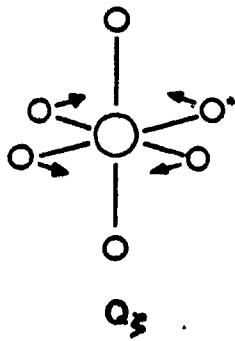
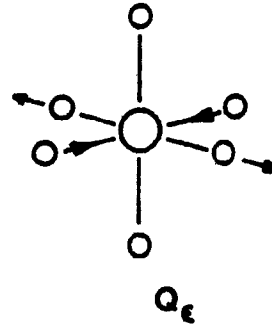
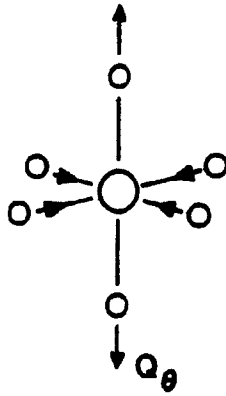
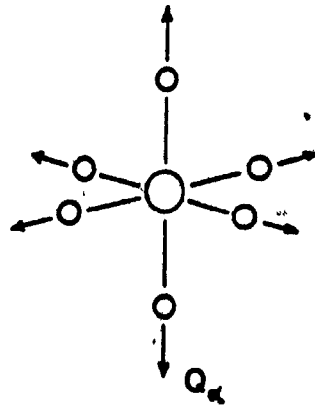
When a JT impurity ion is placed at an atomic site of a certain symmetry, it is coupled to a continuous spectrum of lattice modes via the Coulomb interaction with its neighbors. This many-frequency problem was first tackled by Sloncjewski¹⁵ for an E_g -electronic state and, due to the difficulty of the problem, his treatment is complicated to follow and to assess in physical terms. In fact, approximations must be made which reduce the number of lattice modes of importance in the JT interaction. Such an approximation is the construction of

local modes, i.e., localized vibrations with well defined symmetries centered on the impurity ion which was first developed by Cloizeaux¹⁶ in the harmonic theory of lattice vibrations using generalized Wannier functions in complex energy bands. A relation between the crystal normal modes and the local modes can be established, so that we can define local mode effective frequencies in terms of the various frequencies and wavevectors of the crystal normal modes. Several authors^{17,18,19} have treated the multi-mode full-lattice problem and they all agree to the fact that the local mode effective frequency model is a very good approximation for weak electron-phonon interaction. In fact, O'Brien¹⁸, Halperin and Englman¹⁹, have shown that the displacements of the ion neighbors are well localized around the impurity ion, i.e., the strain field around the ion decreases as R^{-2} , where R measures the distance from the ion. So, they concluded that well-localized modes can be used instead of the phonon continuum to describe the effect of electron-phonon coupling on the electronic energy levels. This is essentially the quasi-molecular model (or cluster model) used by Van Vleck^{13,14} and which will be used in this thesis.

The quasi-molecular model considers the central ion and its nearest neighbors as a separate entity in the crystal lattice. Hence, we consider only the vibrations of the octahedron shown in Fig. 3.1 and we neglect any explicit effect of the surrounding lattice. The quasi-molecular model

Fig. 3-1

The different collective displacements of the oxygen ions surrounding the ferrous impurity in MgO crystal. These displacements represent the effective normal modes of vibration of the cluster model. Their transformation-properties are outlined in Table 3.1.



COLLECTIVE COORDINATES	TRANSFORMATION PROPERTIES		DISPLACEMENTS
Q_α	A_{1g}	$x^2 + y^2 + z^2$	$\frac{1}{\sqrt{6}} [x_1 - x_4 + y_2 - y_5 + z_3 - z_6]$
Q_ϵ	E_g	$\sqrt{3} [x^2 - y^2]$	$\frac{1}{2} [x_1 - x_4 - y_2 + y_5]$
Q_θ		$3z^2 - r^2$	$\frac{1}{2\sqrt{3}} [2z_3 - 2z_6 - x_1 + x_4 - y_2 + y_5]$
Q_5	T_{2g}	yz	$\frac{1}{2} [z_2 - z_5 + y_3 - y_6]$
Q_7		xz	$\frac{1}{2} [x_3 - x_6 + z_1 - z_4]$
Q_5		xy	$\frac{1}{2} [y_1 - y_4 + x_2 - x_5]$

TABLE 3.1

has the advantages of simplicity and intuitive appeal over the multi-mode full-lattice model where there has been more emphasis on mathematical sophistication than on the prediction of observable effects.

The six ligands located at the vertices of the octahedron have each three degrees of freedom for a total of eighteen degrees of freedom for the octahedron. These degrees of freedom can be classified into fifteen degrees of vibrations (A_{1g} , E_g , T_{2g} , $2T_{1u}$ and T_{2u}) and three degrees of rotation (T_{1g}) where the subscript "g" is used for collective even displacements under inversion and "u" for odd displacements under inversion. From group theory, it is a well-known rule that the only operators giving non-zero matrix elements among T_{2g} -states, e.g., the ground state of the ferrous ion, are those transforming as one of the irreducible representations of the direct product

$$T_{2g} \times T_{2g} = A_{1g} + E_g + T_{1g} + T_{2g}$$

Of these, only the operators transforming as E_g and T_{2g} representations of O_h can lift the ground state degeneracy (see chapter 5) and, consequently, lead to a JT effect. The symmetry of the electronic operators and the vibrational modes being linked through the invariance of the JT Hamiltonian (section 3.1.3), we conclude that only vibrational modes transforming as the E_g and T_{2g} representations will interact with the T_{2g} states via the JT interaction.

If a system of coordinates (X_k, Y_k, Z_k) is attached to the K^{th} ligand, we can form a linear combination of ligand displacements that will transform according to the E_g or T_{2g} representations. This linear combination of displacements is a unitary transformation of the (X_k, Y_k, Z_k) coordinates into the Q_n collective coordinates which define the local modes of vibration. Table 3.1 gives the mode symmetry, the collective coordinates (Q_n) and their transformation properties. Figure 3.1 depicts the different collective displacements.

3.1.3 The Jahn-Teller Hamiltonian

The lattice phonons will slightly displace the ligands from their mean positions ($Q_n = 0$) at the vertices of the octahedron. These displacements being small with regard to the lattice spacing, we can expand the Coulomb energy of interaction between the i^{th} electron and the ligands (Eq. (2.2-1)) into a Taylor series in terms of the collective coordinates Q_n , i.e.,

$$\sum_i q_i V'(r, Q) = \sum_i q_i \left[V'_{Oh} + \sum_N \left(\frac{\partial V'}{\partial Q_N} \right) Q_N + \frac{1}{2} \sum_{NM} \left(\frac{\partial^2 V'}{\partial Q_N \partial Q_M} \right) Q_N Q_M + \dots \right] \quad (3.1-1)$$

where the partial derivatives are evaluated at $Q_{n,m} = 0$. Therefore the electrostatic potential can be separated into a static contribution V'_{Oh} obtained in chapter 2 and a dynamical part which depends on Q_n and which is responsible for the electron-phonon interaction. In Appendix C, it is shown that we can neglect the second-order terms in the Taylor expansion (Eq. (3.1-1)) owing to the weak JT coupling coefficients,

Eq. (3.1-9). To completely define $V'(r, Q)$, we need an explicit expression for the partial derivative $(\partial V'/\partial Q_n)$ which can be obtained from the crystal field potential, Eq. (2.2-2), rewritten as

$$V'(\bar{r}, \bar{R}) = \sum_{\lambda=0,2,4} \sum_{x=-\lambda}^{\lambda} \frac{4\pi}{2\lambda+1} \sum_k \frac{a_k}{R_k^{\lambda+1}} r^{\lambda} Y_{\lambda,x}(\theta, \varphi) \quad (3.1-2)$$

where

$$a_k = q_k Y_{\lambda,x}^*(\Theta_k, \Phi_k) \quad (3.1-3)$$

and k labels the ligand ions on the octahedron. To differentiate expression (3.1-2) with respect to Q_n , we must express the collective coordinates in terms of R_k , the ion-ligand separation. If we choose Q_o , Table 3.1, as an example and we make the following change of variables,

$$\begin{aligned} r_k &= R_k - R_o & ; k &= 1, 2, 3 \\ r_k' &= -R_k' + R_o & ; k &= 4, 5, 6 \end{aligned}$$

where r_k stands for x_k , y_k or z_k , R_o is the ion-ligand separation at rest and R_k measures the distance between the displaced ligand and the central ion. Hence, we can rewrite Q_o as

$$Q_o = \frac{1}{2\sqrt{3}} \left[2(R_3 + R_6) - (R_1 + R_4) - (R_2 + R_5) \right]$$

where Q_o is expressed in terms of variables having the same origin of coordinates. Now, we can get an expression for the partial derivatives in Eq. (3.1-1) using for example

$$\begin{aligned} \frac{\partial}{\partial Q_o} &= \sum_k \left(\frac{\partial Q_o}{\partial R_k} \right) \frac{\partial}{\partial R_k} \\ &= \sum_k c_k^o \frac{\partial}{\partial R_k} \end{aligned} \quad (3.1-4)$$

with $c_1 = c_2 = c_4 = c_5 = -1/2\sqrt{3}$ and $c_3 = c_6 = 1/\sqrt{3}$. In a more general way the partial derivatives can be expressed, using Eq. (3.1-4) and Eq. (3.1-2), as

$$\left(\frac{\partial V}{\partial Q_N}\right)_{Q_N=0} = \sum_{\lambda, x} \frac{4\pi}{2\lambda+1} \sum_k^{-(\lambda+1)} \frac{c_k^N a_k}{R_0^{\lambda+1}} r_i^\lambda Y_{\lambda, x}(\theta_i, \phi_i) \quad (3.1-5)$$

If we carry on the summation over k, x and λ , in Eq. (3.1-5), and use the expressions for the Tesseral harmonics in terms of cartesian coordinates (see Appendix C), we obtain for the particular case of $Q_n = Q_0$,

$$\left(\frac{\partial V}{\partial Q_0}\right)_{Q_0=0} = \frac{-q}{4\pi\epsilon_0 R_0^2} \cdot \frac{1}{2\sqrt{3}} \left[\frac{9}{R_0^2} (3z_i^2 - r_i^2) + \frac{25}{16R_0^4} (35z_i^4 - 30z_i^2 r_i^2 + 3r_i^4) - \frac{35}{16R_0^4} (x_i^4 - 6x_i^2 y_i^2 + y_i^4) \right] \quad (3.1-6)$$

The Coulomb energy of the ion-ligand interaction results after a summation of the energy $q_i V(r_i, R)$ over all the electrons of the central ion. The summation, because of equations (3.1-1) and (3.1-6), involves terms like

$$\sum_i q_i (3z_i^2 - r_i^2)$$

which can be transformed easily into electronic operators by Stevens' operator equivalent method²⁰. This method is applicable for evaluating matrix elements of the crystalline potential between wavefunctions characterized by one particular value of angular momentum, i.e., Stevens operator equivalent method applies within the $^5T_{2g}$ states of the ferrous ion. This method is a direct consequence of the Wigner-Eckart theorem^{21, 22} which

stipulates that the matrix elements of the components of angular momentum are proportional to the matrix elements of any tensor, in a specified subspace of J , e.g., the ground state of the ferrous ion. Since, in the simple octahedral group, the orbital angular momentum transforms as the cartesian coordinates, i.e., T_4 or T_1 , we can replace x, y and z by the operator equivalent L_x, L_y and L_z , respectively. The non-commutation of the components of angular momentum is accounted for by replacing bilinear combinations of L_x, L_y and L_z divided by the total number of combinations. As an example, following Stevens' method, the summation over the electrons of the central ion can be transformed as

$$\sum_i q_i (3z_i^2 - r_i^2) = \alpha_L q \langle r^2 \rangle [3L_z^2 - L(L+1)] \quad (3.1-7)$$

where $\alpha_L = -2/21$ for $3d^6$ ions.

The MgO crystal being a purely ionic crystal, the electrons are well localized around the ferrous ion so that

$$\left[\beta_L \frac{\langle r^4 \rangle}{R_0^4} \right] \cdot \left[\alpha_L \frac{\langle r^2 \rangle}{R_0^2} \right]^{-1} \ll 1$$

where $\beta_L = 2/63$ is a coefficient similar to α_L , but related to the higher order terms of Eq. (3.1-6). Therefore, we can neglect the last two terms in Eq. (3.1-6). The partial derivative, Eq. (3.1-6), is rewritten using Eq. (3.1-7) as

$$\begin{aligned} \left(\frac{\partial V'}{\partial Q_0} \right)_{Q_0=0} &= \frac{2\sqrt{3}}{7} \cdot \frac{q}{4\pi\epsilon_0 R_0^2} \cdot \frac{\langle r^2 \rangle}{R_0^2} \cdot \frac{1}{2} [3L_z^2 - L(L+1)], \\ &= V_E E_0 \end{aligned} \quad (3.1-8)$$

where we define the JT coupling coefficient to E_g -modes of vibration,

$$V_E = \frac{2\sqrt{3}}{7} \frac{q}{4\pi\epsilon_0 R^2} \frac{\langle r^2 \rangle}{R^2} \quad (3.1-9)$$

and E_g is defined by Eq. (3.1-10a). Consequently, for each collective coordinate Q_n , we can derive an expression for the partial derivative similar to Eq. (3.1-8) and we can define an associated electronic operator that transforms as the irreducible representation of the mode of vibration. The electronic operators are

$$\text{Eg-REPRESENTATION: } E_g = \frac{1}{2} [3L_z^2 - L(L+1)] \quad (3.1-10a)$$

$$E_e = \frac{\sqrt{3}}{2} [L_x^2 - L_y^2] \quad (3.1-10b)$$

$$\text{T}_{2g}\text{-REPRESENTATION: } T_g = L_y L_z + L_z L_y \quad (3.1-10c)$$

$$T_\gamma = L_z L_x + L_x L_z \quad (3.1-10d)$$

$$T_\xi = L_x L_y + L_y L_x \quad (3.1-10e)$$

We have obtained that the partial derivative with respect to Q_n , in Eq. (3.1-1), transforms the same way as its associated Q_n , so that the summation over the electrons of the central ion

$$\sum_i q_i \sum_N \left(\frac{\partial V}{\partial Q_N} \right) Q_N$$

transforms as the bilinear combinations of the type $(Q_g^2 + Q_e^2)$ and $(Q_g^2 + Q_\gamma^2 + Q_\xi^2)$ which are invariant under the symmetry operations belonging to the octahedral group. This invariant is the JT Hamiltonian expressed as,

$$H_{JT} = V_E (Q_g E_g + Q_e E_e) + V_T (Q_g T_g + Q_\gamma T_\gamma + Q_\xi T_\xi) \quad (3.1-11)$$

where V_T is the JT coupling coefficient to the T_{2g} -modes of vibration which can be defined by an expression similar to Eq. (3.1-9). The point charge approximation leading to the expressions for V_E and V_T based on crystal field theory appear too crude and give no accordance with experiments. Angular overlap model²³ or linear combination of atomic orbitals²⁴ (LCAO) method give more consistent values to the experimental results. In all cases, the quality of the quasi-molecular model is much improved when V_E and V_T become parameters determined experimentally in a similar fashion to Dq , Eq. (2.2-10), in crystal field theory. Accordingly, we determine the JT coupling coefficients experimentally via the strain coupling coefficients as shown in chapter 5.

3.2 The weak Jahn-Teller effect

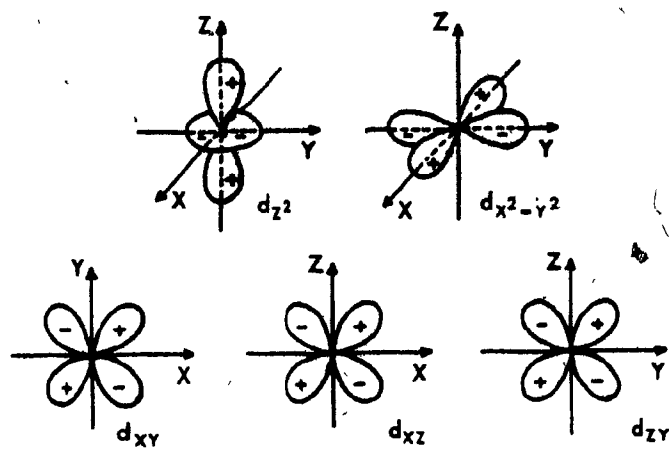
3.2.1 The molecular orbitals

The six 3d-electrons of the ferrous ion are distributed over the five d-orbitals pictured in Fig. 3.2a. The crystalline electric field distinguishes two sets of orbitals: the two d_{xy} orbitals for E_g -states and the three d_e orbitals for T_{2g} -states which lie lowest in energy. The ferrous ion assumes the high spin configuration, i.e., the maximum total spin momentum given by $d_e^4 d_{xy}^2$, Fig. 3.2b. In this configuration, the electrons are spread over the d_{xy} and d_e orbitals to minimize the Coulomb energy of interaction between them, the energy being further reduced by the quantum mechanical exchange energy which is null for spin pairing.

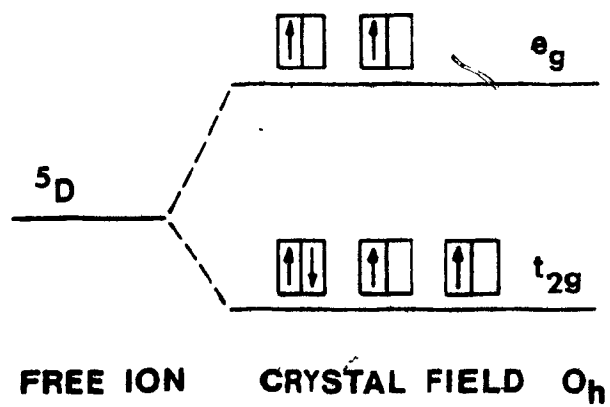
Fig. 3-2

(a) The electrons are distributed over five d-orbitals. The two upper charge distributions transform as E_g symmetry, whereas the three lower charge distributions transform as T_{2g} symmetry.

(b) High-spin configuration of the ground state of the ferrous ion ($3d^6$) constructed from one-electron crystal field states.



(a)



(b)

The oxygen ligand (O^{2-}) has its s-orbital and its p-orbitals occupied, and form molecular bonds with the central ion (Fe^{2+}). Two types of molecular bonds are formed, as depicted in Fig. 3.3:

(i) the σ -bonding which is formed between the 2s and $2p_{\sigma}$ orbitals of the oxygen ion and the d_{γ} -orbitals of the ferrous ion.

(ii) the π -bonding between the $2p_{\pi}$ orbitals of the oxygen ion and the d_{π} -orbitals of the ferrous ion.

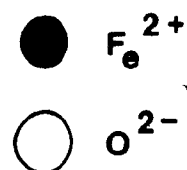
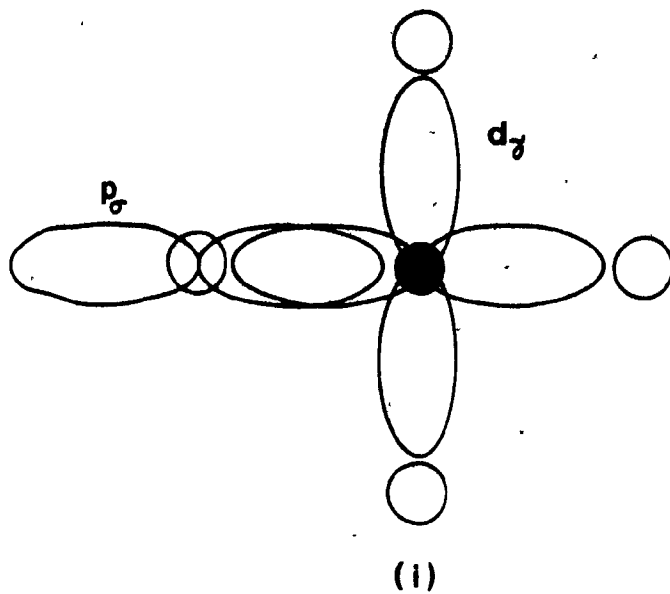
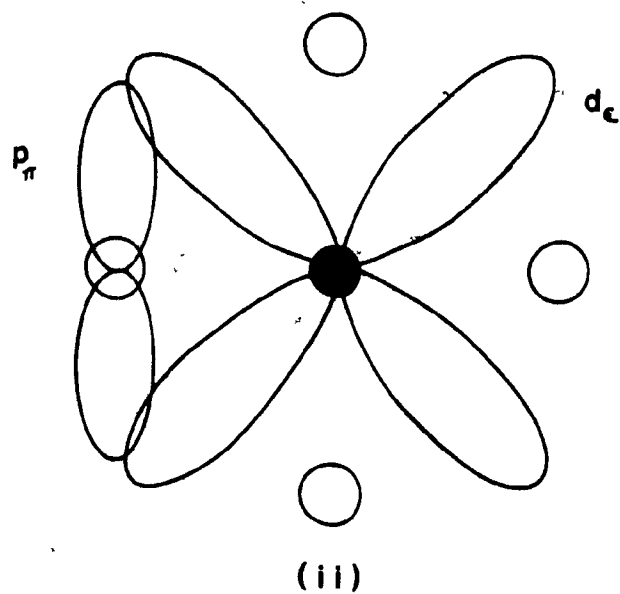
The σ -bonding is known to be very strong in octahedral complexes. This phenomenon explains the occurrence of strong JT effect for E_g -states, whereas the π -bonding being weak in octahedral complexes leads to weak JT effect for T_{2g} -states. To first order, the spin-orbit interaction mixes the d_{π} -orbitals, but this situation has no consequences on the previous conclusion.

3.2.2 $T_{2g} \times e_g$

In order to introduce the definition of the JT energy in terms of the JT coupling coefficients, V_E and V_T , and the concept of reduction coefficient (γ), we choose to study the heuristic case of an orbital triplet state (T_{2g}) coupled to a doubly degenerate vibrational mode (e_g). Subsection 3.2.4 discusses the general case of coupling to two different local modes pertinent to the ferrous ion in MgO .

Fig. 3-3

Two types of molecular bonds are formed, as discussed in the text. In (i), d_{xy} is identical with $d_{x^2-y^2}$ (Fig. 3-2a). Only one oxygen ion is shown with its p-orbital, for clarity.

σ -BONDING π -BONDING

In this particular case, we consider the octahedron formed by the ligands as an harmonic oscillator with its equilibrium position given by $Q_o = Q_e = 0$. The energy of the electron-phonon interaction includes a kinetic term, an elastic term and a JT term, respectively given by

$$H_K + H_{EL} + H_{JT} = 1/2 \mu_E (P_o^2 + P_e^2) \cdot I + \mu_E \omega_E^2 / 2 (Q_o^2 + Q_e^2) \cdot I + V_E (Q_o E_o + Q_e E_e) \quad (3.2-1)$$

where p_n is the momentum conjugate to Q_n , μ_E and ω_E denote, respectively, the effective mass and angular frequency for E_g -modes and I is the identity matrix. As stipulated by the JT theorem, the electron-phonon interaction (H_{JT}) lowers the energy of the harmonic oscillator and distorts the atomic site, i.e., displaces the equilibrium positions of the harmonic oscillators. In minimizing equation (3.2-1), we obtain the new equilibrium positions:

$$\begin{aligned} \text{(i)} \quad & Q_o = Q \quad ; \quad Q_e = -\sqrt{3}Q \\ \text{(ii)} \quad & Q_o = Q \quad ; \quad Q_e = \sqrt{3}Q \\ \text{(iii)} \quad & Q_o = -2Q \quad ; \quad Q_e = 0 \end{aligned} \quad (3.2-2)$$

where

$$Q = \frac{V_E}{2\mu_E \omega_E^2}$$

After substitution of these new equilibrium positions into Eq. (3.2-1), we obtain the corresponding JT energy defined as the shift in energy induced by the JT effect

$$(E_{JT})_E = V_E^2 / 2\mu_E \omega_E^2 \quad (3.2-3)$$

The Hamiltonian, Eq. (3.2-1), is diagonal within the vibronic functions so that the electronic states are not mixed by the electron-phonon interaction. The potential energy surface in Q_e, Q_g -space consists of three disjoint paraboloids, as depicted by Liehr²⁵, Fig. 3.4. In fact, each paraboloid corresponds to a static tetragonal distortion of the cluster along either X, Y or Z-axis, each direction being perfectly equivalent and equally probable. Since the electronic functions centered on each paraboloid are orthogonal to each other, the cluster should undergo a static tetragonal deformation and remain indefinitely in one of the paraboloids. This is schematically what happens for a strong JT effect. Experimentally, the static deformation is not always observed because the spin-orbit interaction, which we have neglected in Eq. (3.2-1), admixes the electronic functions and allows, within certain conditions, the cluster to oscillate between the different paraboloids. In that case, we have a dynamic JT effect, i.e., the JT complex shows a statistical distribution of its states over the various possible distortion states. Experimentally, we observe the time average of the cluster oscillations between equivalent distortion states and, therefore, the JT complex shows a higher macroscopic symmetry than predicted for a static deformation, e.g., O_h symmetry for Fe^{2+} in MgO .

Since the effective orbital angular momentum has non-zero off-diagonal matrix elements and zero diagonal matrix

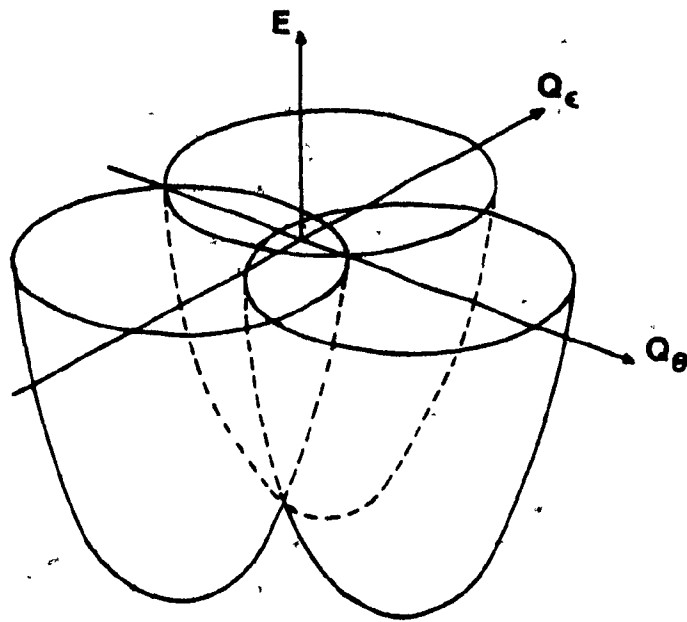


Fig. 3.4

Potential energy surfaces corresponding to an orbital triplet state coupling linearly to a vibrational mode (Q_θ, Q_ϵ) of E_g -symmetry, i.e., $T_{2g} \times e_g$.

elements between the electronic T_{2g} states, these same matrix elements are multiplied by a vibrational overlap integral γ which accounts for the reduced overlap of two paraboloids. Ham²⁶ first conceived a simple analytical approach to this problem using displaced harmonic oscillator wavefunctions to describe the vibrational states. These vibrational states are suitably represented by Glauber states which are effectively displaced harmonic oscillator wavefunctions, as demonstrated by Judd²⁷. The Glauber states simplify appreciably the calculations involved in more complicated problems of this type. In the harmonic approximation, Ham²⁶ showed that the overlap integral γ_E equals to

$$\gamma_E = \exp(-3E_{JT}/2\hbar\omega) \quad (3.2-4)$$

When there is spin-orbit interaction, the dynamic JT effect is established if the zero-point energy ($\hbar\omega$) is large enough to bring the complex in the region where the vibrational functions overlap, i.e., the following inequality condition must be satisfied

$$E_{JT} \leq \hbar\omega \quad (3.2-5)$$

Consequently, a weak JT effect is characterized by a dynamic JT effect and moderately reduced matrix elements of the angular momentum. For the case of strong JT effect, i.e. $E_{JT} \gg \hbar\omega$, the overlap integral tends to zero and the complex is confined to a particular paraboloid.

3.2.3 $T_{2g} \times t_{2g}$

The problem of an orbital triplet state (T_{2g}) coupled to a triply degenerate vibrational mode (t_{2g}) has been treated analytically by Ham²⁶ and Judd²⁷ following two different approaches and is similar in some respects to the previous case of $T_{2g} \times e_g$. We can write the Hamiltonian for such a situation in a similar fashion to equation (3.2-1), i.e.,

$$H_K + H_{EL} + H_{JT} = 1/2\mu_T (P_\xi^2 + P_\eta^2 + P_\zeta^2)\bar{I} + \mu_T\omega_T^2/2(Q_\xi^2 + Q_\eta^2 + Q_\zeta^2)\bar{I} + V_T(Q_\xi T_\xi + Q_\eta T_\eta + Q_\zeta T_\zeta) \quad (3.2-6)$$

where P_n is the momentum conjugate to Q_n , μ_T and ω_T denote, respectively, the effective mass and angular frequency for T_{2g} -modes and \bar{I} is the identity matrix. We can establish four linear combinations of the Q_n which minimize the energy of the Hamiltonian, Eq. (3.2-6), and which represent the four possible trigonal distortions of the cluster, Fig. 3.5. Judd²⁷ obtains easily the equilibrium positions of the displaced harmonic oscillators:

$$\begin{array}{lll} \text{(i)} & Q_{yz} = Q; & Q_{zx} = Q; & Q_{xy} = Q \\ \text{(ii)} & Q_{yz} = Q; & Q_{zx} = -Q; & Q_{xy} = -Q \\ \text{(iii)} & Q_{yz} = -Q; & Q_{zx} = -Q; & Q_{xy} = Q \\ \text{(iv)} & Q_{yz} = -Q & Q_{zx} = Q; & Q_{xy} = -Q \end{array}$$

where

$$Q = \frac{2V_T}{3\mu_T\omega_T^2}$$

The JT energy, as defined in the previous subsection, is obtained after substitution of the equilibrium positions in

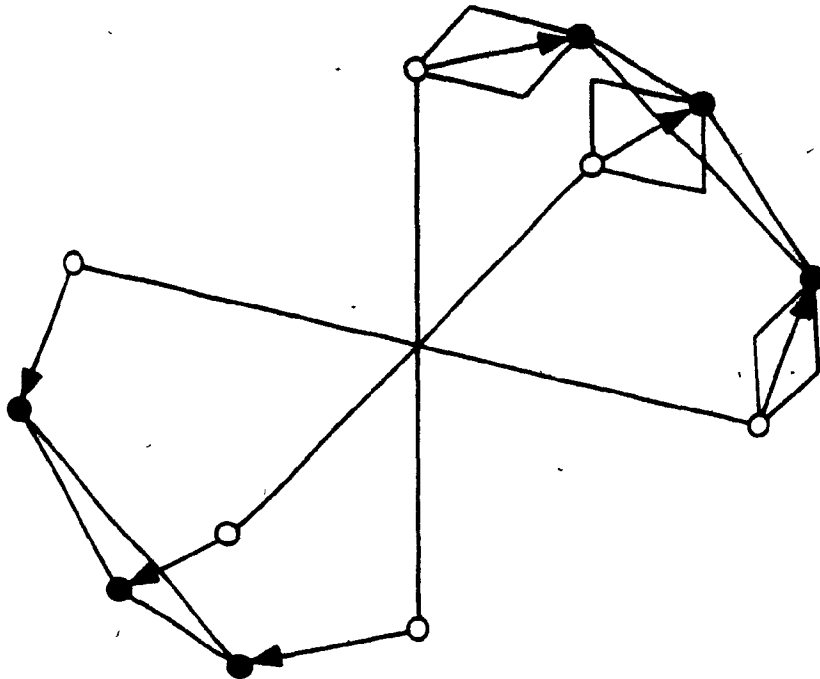


Fig. 3-5

Trigonal distortion of the octahedron formed by the oxygen ions. Each oxygen ions being at the face center of a cube, four such distortions are possible along the four different cube diagonals, resulting from the Jahn-Teller interaction between an orbital T_{2g} state and a t_{2g} vibrational mode.

the Hamiltonian, Eq. (3.2-6),

$$(E_{JT})_T = \frac{2V_T^2}{3\mu_T\omega_T^2} \quad (3.2-7)$$

In this case, the four vibronic functions which characterize the states in each displaced paraboloid are products of linear combination of the T_{2g} -electronic states and Glauber states, and, consequently, allow the complex to tunnel between the possible trigonal distortions. This ability of the oscillator to tunnel introduces a tunneling splitting in the lowered T_{2g} -states and removes the forbidden four-fold degeneracy of the equivalent trigonal distortions. This is the strong JT effect and the resulting potential energy sheets are cubic hypersurfaces which have been depicted by Liehr²⁵.

Due to the reduced overlap of the oscillator vibrational functions and of the purely electronic functions, Judd²⁷ obtains a reduction factor (γ_T) similar to that for γ_E , Eq. (3.2-4),

$$\gamma_T = -(1/3)\exp(-4E_{JT}/3\hbar\omega) \quad (3.2-8)$$

Similarly to the previous case but without having recourse to the spin-orbit interaction, a dynamic JT effect can be established between the four equivalent distortions if condition (3.2-5) is satisfied.

3.2.4 $T_{2g} \times (e_g + t_{2g})$

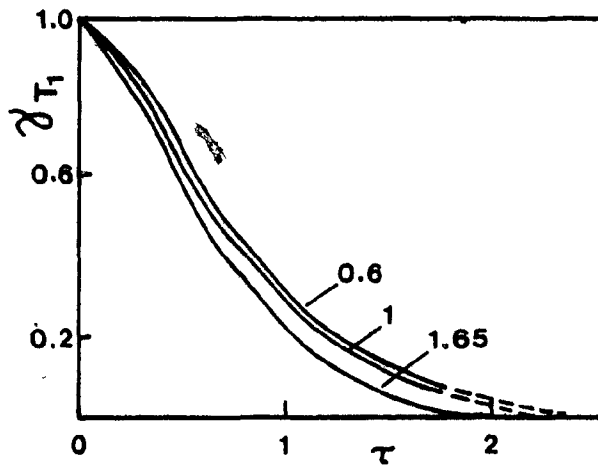
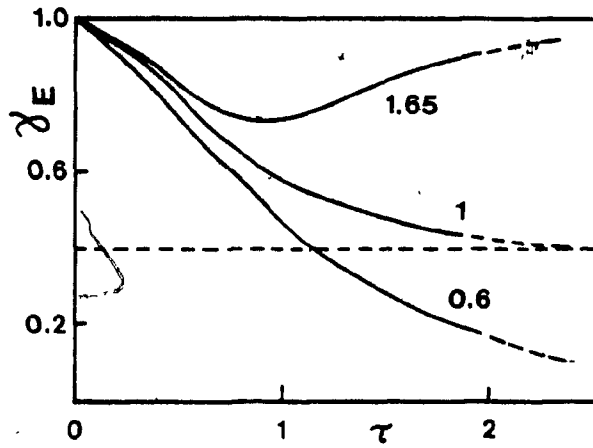
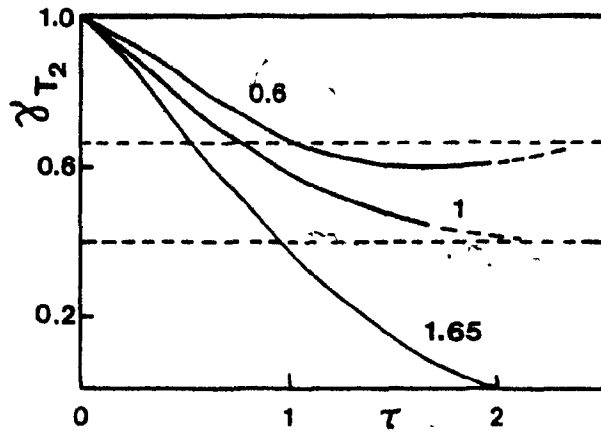
The coupling of electronic T_{2g} -states to the two types

of vibrational modes, introduced in subsection 3.1.2, is much more realistic than the previous cases discussed in subsections (3.2.2) and (3.2.3). This problem is also much more complicated mathematically and no complete detailed analysis of the JT interaction and its physical implications have been offered up to now. Nevertheless, Opik and Pryce²⁸ were able to show that tetragonal and trigonal distortions coexist with saddle points between the minima. They found that the potential energy surface has tetragonal wells of lower energy than the trigonal ones if $(E_{JT})_E > (E_{JT})_T$, Eq. (3.2-3) and (3.2-6). In this case, it is found that the matrix elements of electronic operators transforming as the T_{2g} irreducible representation, between the vibronic functions, are much reduced with respect to matrix elements of operators transforming as the E_g irreducible representation of O_h . For example, a uniaxial tetragonal stress would split a degenerate energy level belonging to these T_{2g} -states, but a uniaxial trigonal stress would be inefficient to split the same energy level. The converse is true if the interaction with T_{2g} -modes is stronger than the interaction with E_g -modes of vibration, i.e., if $(E_{JT})_T > (E_{JT})_E$. Fig. 3.6 shows the relative strength of the reducing factors $\gamma(T_2)$ and $\gamma(E)$ for T_2 -electronic operator and E -electronic operator, respectively.

For the special case of equal coupling with e_g and t_{2g} modes of vibration, i.e., $(E_{JT})_E = (E_{JT})_T$, O'Brien²⁹

Fig. 3-6

Orbital reduction factors $\gamma(T_1)$, $\gamma(E)$ and $\gamma(T_2)$ as a function of the strength of the Jahn-Teller interaction when the coupling is to both e_g and t_{2g} modes of vibration. $\tau = V/(\mu\hbar\omega^3)^{\frac{1}{2}}$ and in each case, three different values (0.6, 1, 1.65) for the ratio $[(E_{JT})_E/\hbar\omega_E]/[(E_{JT})_T/\hbar\omega_T]$ are given which indicates how the JT coupling is shared between e_g and t_{2g} vibrational modes.



proposed a vibronic model called the D-mode model. Assuming that the five vibrational modes are degenerate in energy (D-mode) and that their JT coupling is strong, the powerful symmetry properties of the five dimensional rotation group (R_5) may be used to solve the problem. This technique is elegant and efficient but nevertheless restricted in its application due to the assumption of equal coupling. Recently, an attempt³⁰ has been made to relax the constraint of the D-mode model by assuming degenerate frequencies but different coupling strength.

For small JT coupling strength to e_g and t_{2g} modes of vibration, it is found³¹ that the two types of modes operate independently, i.e., the e_g modes tend to stabilize the tetragonal deformations without competing with the t_{2g} modes which tend to stabilize the trigonal distortions. The potential energy surface is essentially five-dimensional containing various minima, maxima and saddles points. Since the reducing effect of the different modes on the matrix elements of electronic operators are simply additive, we can separate the JT Hamiltonian into two parts including either e_g modes or t_{2g} modes of vibration, and each part is treated by perturbation theory independently from the other. This is the approach that we adopt for the particular case of $MgO:Fe^{2+}$.

3.3 The experimental evidences

3.3.1 The orbital reduction factors

As mentioned in subsection 3.2.2, the matrix elements of the components of the orbital angular momentum or any operator with off-diagonal matrix elements between the orbital states (T_{2g}) are reduced between the vibronic functions from their values in absence of JT effect. This is due to the reduced overlap of the vibrational functions characterizing each distortion of the cluster. These vibrational overlap integrals are called orbital reduction factors. Since the spin-orbit interaction is expressed as a linear function of the orbital angular momentum, Eq. (2.3-6), we expect the spin-orbit splitting of the ${}^5T_{2g}$ -states to be reduced from the predicted crystal field value as well, Eq. (2.3-10a) to (2.3-10f). Therefore, a set of spin-orbit energy levels appearing as predicted by crystal field theory but with a reduced spin-orbit splitting is the signature of a weak or intermediate JT effect. Whereas, a strong JT effect would completely quench a small spin-orbit interaction.

Van Vleck^{32,33} was the first to notice that a strong spin-orbit interaction may stabilize the cluster against weak JT deformations. In fact, the spin-orbit interaction of the T_{2g} orbital states lifts some of the degeneracies (spin-orbit splitting). If, as a result, no degeneracy other than Kramers degeneracies is left, no JT effect is expected (JT theorem). On the other hand, if some degeneracy is left, it may be primarily spin-degeneracy in which case the matrix elements

of the strain operators, see chapter 5, are much reduced and the JT effect is correspondingly weak. Van Vleck^{32,33} has set an inequality relation between the spin-orbit coupling parameter and the JT energy, i.e.,

$$|\lambda| \geq E_{JT} \quad (3.3-1)$$

which establishes when the JT effect is expected to be minimized by the strong spin-orbit interaction. As will be shown in chapter 5, both conditions (3.2-5) and (3.3-1) are satisfied for the T_{2g} -states of the ferrous ion in MgO, so that the assumption of weak JT effect for the ferrous ion in MgO is well justified in accordance with the expectations from the type of molecular bonding. For instance, it is generally found that those systems having an orbital doublet ground state (E_g) are particularly susceptible to JT effect because there is little competition to the electron-phonon interaction from other perturbations, e.g., spin-orbit interaction and trigonal distortions have zero matrix elements between the E_g -orbital states. The opposite is true for the T_{2g} -orbital states.

Stevens³⁴ has shown that if the JT complex is not purely ionic, as assumed by crystal field theory, but that a small charge transfer exists between the central ion and the ligands, the resulting weak covalent bonding reduces the spin-orbit coupling parameter. In fact, the spin-orbit coupling parameter, for a small admixture of d-orbitals from the central

ion and p-orbitals from the ligands, is expressed³⁴ as

$$\lambda = -\frac{1}{4} \zeta_{\pi\pi} = -\frac{1}{4} N_{\pi}^2 (\zeta_d + \frac{\alpha_{\pi}^2}{2} \zeta_p) \quad (3.3-2)$$

where $\zeta_{\pi\pi}$ is the one-electron spin-orbit parameter, Eq. (2.3-7), N_{π} and α_{π} are the normalization factor and the admixture coefficient, respectively, ζ_d and ζ_p are the spin-orbit parameters for a 3d orbital (Fe^{2+}) and for a 2p orbital (O^{2-}), respectively. Ham et al³⁵ estimates, for the case of $\text{MgO}:\text{Fe}^{2+}$, that the covalent bonding is not likely to reduce λ by more than 10% from its free ion value, α_{π}^2 being small. Consequently, the covalent bonding simulates³⁶ the JT effect by reducing λ and, thus, the spin-orbit splitting.

3.3.2 The Ham reduction Factors

We have shown in section 3.1 that electronic operators can be defined following Stevens' operator equivalent method^{20,37} e.g., Eq. (3.1-7). These operators are multiplied by a numerical constant α_L which depends on the configuration of the particular ion (e.g. 3d⁶) and on the total angular momentum of the electrons L (or J). We can determine the matrix elements of these electronic operators³⁸ either in the $^5\text{T}_{2g}$ orbital states characterized by a given value of L, e.g.,

$$\langle \text{LM}_L | \sum_i (3z_i^2 - r_i^2) | \text{LM}_L \rangle = \alpha_L \langle r^2 \rangle \langle \text{LM}_L | (3L_z^2 - L(L+1)) | \text{LM}_L \rangle \quad (3.3-3)$$

or, in the spin-orbit states characterized by a given value of J, e.g.,

$$\langle JM_J | \sum_i (3z_i^2 - r_i^2) | JM_J \rangle = \alpha_J \langle r^2 \rangle \langle JM_J | (3J_z^2 - J(J+1)) | JM_J \rangle \quad (3.3-4)$$

where a numerical value for the coefficients α_L and α_J which depends on the detailed nature of the states can be obtained by returning to the direct integration method of finding matrix elements between single-electron determinantal functions.

The matrix elements of a given Hamiltonian can be obtained easily in the spin-orbit states once the expression of the same Hamiltonian in the orbital states is known. This time-saving calculation technique was first explicitly used by Ham et al³⁵ and can be summarized by the relation

$$H(L) \rightarrow (\alpha_J/\alpha_L) H(J) \quad (3.3-5)$$

where $H(L)$ and $H(J)$ are the Hamiltonians which operate on the orbital states and spin-orbit states, respectively, and α_L , α_J are defined in Eqs. (3.3-3) and (3.3-4), respectively. The ratio of the two constants in (3.3-5) is called the Ham reduction factor which we define as

$$K_{\Gamma}(J) = \alpha_J(\Gamma) / \alpha_L(\Gamma) \quad (3.3-6)$$

where Γ specifies a set of operators belonging as partners to an irreducible representation of O_h . The Ham reduction factors result from a reduced effective orbital angular momentum due to the mixing of the orbital functions and spin functions in the spin-orbit states. The following example shows how to determine the Ham reduction factors for any given L and J value.

Using the Clebsch-Gordon coefficients⁵, we can express the spin-orbit states characterized by a given value of J in terms of states characterized by a given value of L and S , i.e.,

$$|JM_J\rangle = \sum_{M_L=-L}^L \sum_{M_S=S}^S |LS;M_L M_S\rangle \langle LS;M_L M_S | JM_J\rangle \quad (3.3-7)$$

In the case of $MgO:Fe^{2+}$, we have $L = 1$ and $S = 2$ for the ${}^5T_{2g}$ states, and we can select $J = M_J = 1$ for the a_{1g} -states. Consequently, Eq. (3.3-7) gives

$$|1\ 1\rangle = (1/10)^{\frac{1}{2}} |12;10\rangle + (3/10)^{\frac{1}{2}} |12;01\rangle + (6/10)^{\frac{1}{2}} |12;-12\rangle \quad (3.3-8)$$

From Eqs. (3.3-3), (3.3-4) and (3.3-8), we obtain the equality

$$\begin{aligned} \alpha_{J=1} &= \langle 1\ 1 | (3J_z^2 - J(J+1)) | 1\ 1 \rangle = \\ \alpha_{L=1} &= \langle 1 | E_{\theta} | 1 \rangle + \langle 0 | E_{\theta} | 0 \rangle + \langle -1 | E_{\theta} | -1 \rangle \end{aligned} \quad (3.3-9)$$

where E_{θ} is defined in Eq. (3.1-10a) and the label M_L alone has been retained on the right hand side of the equality. The matrix elements in Eq. (3.3-9) can be determined easily and we obtain the result

$$\alpha_{J=1} / \alpha_{L=1} = 1/10$$

The same ratio is obtained for all the electronic operators defined by Eqs. (3.1-10a) to (3.1-10e). Hence, the Ham reduction factors for the spin-orbit ground states of the ferrous ion in MgO are

$$K_E(J=1) = K_T(J=1) = 1/10 \quad (3.3-10)$$

Following exactly the same procedure for the case $J = 2$, $L = 1$ and $S = 2$, we obtain the ratio of the constants $\alpha_{J = 2}$ and $\alpha_{L = 1}$ equals to $-1/6$ establishing the Ham reduction factors for the first two excited states Γ_{3g} and a $\Gamma_{4g'}$

$$K_E(J = 2) = K_T(J = 2) = -1/6 \quad (3.3-11)$$

Ham et al³⁵ specified that equation (3.3-10) also gives the ratio of the matrix elements of the appropriate orbital operator in the a Γ_{5g} ground states to the corresponding matrix elements of the same operator among the orbital triplet states. This assertion is true as long as we compare matrix elements of orbital operators in orbital states and spin-orbit states satisfying $L = J$. For example, we obtain a ratio of $-1/6$ for the appropriate matrix elements of orbital operators in the five D states ($L = 2$, Eq. (2.2-9)) and in the spin-orbit states with $J = 2$, as expected from Eq. (3.3-11).

The Ham reduction factors are perturbed by the weak JT effect. In order to calculate the appropriate corrections via perturbation theory, as demonstrated in section 3.4, we follow Ham et al³⁵ in defining the reduction factors for orbital operators transforming as E_g and T_{2g} representations by representative matrix elements:

(i) $J = 1$ ($a\Gamma_{5g}$ -level)

$$K_E(1) = - \langle \varphi_1(a\Gamma_{5g}) | E_{\theta} | \varphi_1(a\Gamma_{5g}) \rangle = 1/10 \quad (3.3-12a)$$

$$K_T(1) = - \langle \varphi_1(a\Gamma_{5g}) | T_{\eta} | \varphi_2(a\Gamma_{5g}) \rangle = 1/10 \quad (3.3-12b)$$

(ii) $J = 2$ (Γ_{3g} - and Γ_{4g} -level)

$$K_E(2) = (1/3) \langle \varphi_1(\Gamma_{3g}) | E_{\theta} | \varphi_1(\Gamma_{3g}) \rangle = -1/6 \quad (3.3-12c)$$

$$K_T(2) = (-1/3) \langle \varphi_1(a\Gamma_{4g}) | T_{\eta} | \varphi_3(a\Gamma_{4g}) \rangle = -1/6 \quad (3.3-12d)$$

The use of representative matrix elements to define the reduction factors is justified since the factor K_E or K_T comes out naturally when the spin-orbit states are used explicitly to calculate the matrix elements of given orbital operators.

We restrict the analysis to the three levels ($a\Gamma_{5g}$, Γ_{3g} and $a\Gamma_{4g}$) since the higher excited states (Γ_{1g} , $b\Gamma_{4g}$ and $b\Gamma_{5g}$) cannot be observed experimentally for reasons given in chapter 4. The Ham reduction factors are essential to extract the value of the strain coupling coefficients from the experimental results, as demonstrated in chapter 5.

3.3.3 The g-factor

When the MgO:Fe^{2+} sample is placed in a magnetic field H , the electronic angular momentum interacts with the magnetic field and some of the energy levels are split : this is the Zeeman effect⁵. The Hamiltonian of the Zeeman interaction is written

$$H_Z = \beta(L \cdot H + g^0 S \cdot H)$$

where $\beta = e\hbar/2mc$ is the Bohr magneton and $g^0 = 2.0023$ is the gyromagnetic factor. To the accuracy of second-order perturbation theory, the effect of the Zeeman interaction on the ${}^5T_{2g}$ -states is expressed as

$$\begin{aligned} H_Z({}^5T_{2g}) = & (g^0 - 8\lambda/\Delta) \beta S \cdot H - k\beta L \cdot H \\ & - (2\lambda/\Delta) \beta [(L \cdot S)(L \cdot H) + (L \cdot H)(L \cdot S)] \\ & + (12\lambda/\Delta) \beta (L_x^2 S_x H_x + L_y^2 S_y H_y + L_z^2 S_z H_z) \end{aligned} \quad (3.3-5)$$

where the parameter k has been introduced to account for covalency effect and L is the effective orbital angular momentum (cf. subsection 2.2.1). We can define appropriate Ham reduction factors, in analogy with Eq. (3.3-4), so that the Zeeman splitting of the $a\Gamma_{5g}$ ground state is given³⁵ by

$$H_Z(a\Gamma_{5g}) = \beta g(J \cdot H)$$

where

$$g = \left[g^0 - 8\lambda/\Delta \right] K_S - kK_L - \left[2\lambda/\Delta \right] K_A + \left[12\lambda/\Delta \right] K_B \quad (3.3-6)$$

and J is the effective angular momentum defined with respect to the $a\Gamma_{5g}$ vibronic ground state. Within the $a\Gamma_{5g}$ ground state, the Ham reduction factors in equation (3.3-6) are defined³⁵ to be

$$K_L(a\Gamma_{5g}) = i \langle \varphi_2(a\Gamma_{5g}) | L_z | \varphi_3(a\Gamma_{5g}) \rangle \quad (3.3-7a)$$

$$K_S(a\Gamma_{5g}) = i \langle \varphi_2(a\Gamma_{5g}) | S_z | \varphi_3(a\Gamma_{5g}) \rangle \quad (3.3-7b)$$

$$K_A(a\Gamma_{5g}) = i \langle \varphi_2(a\Gamma_{5g}) | (L \cdot S) S_z + L_z (L \cdot S) | \varphi_3(a\Gamma_{5g}) \rangle \quad (3.3-7c)$$

$$K_B(a\Gamma_{5g}) = i \langle \varphi_2(a\Gamma_{5g}) | L_z^2 S_z | \varphi_3(a\Gamma_{5g}) \rangle \quad (3.3-7d)$$

where the $\varphi_i(\Gamma_j)$ are given in Appendix B.

The experimental g -factor in the $a\Gamma_{5g}$ ground state of $MgO:Fe^{2+}$ is found to be reduced from its predicted crystal field value 3.5, Eq. (3.3-6). Ham et al³⁵ have shown that the observed reduction in the ground state g -factor and the spin-orbit splitting are in large part the result of the JT effect, the covalency effect accounting for a maximum of 10% of the observed reduction. For the self-consistency of the model, the reduction in the spin-orbit splitting and of the ground state g -factor must be compatible with the strain

coupling coefficients, determined in chapter 5, which can be related to the JT coupling coefficients. The self-consistency of the model is discussed in chapter 5.

3.4 Calculations by perturbation theory

3.4.1 The vibronic functions

In section 3.2, we have shown that the assumption of a weak JT effect in the ${}^5T_{2g}$ -states of the ferrous ion in MgO is reasonable from a theoretical point of view or from a molecular orbital approach, and Ham came to the same conclusion following his interpretation of Wong's results (see chapter 4). Therefore, we follow Ham in treating the JT Hamiltonian (H_{JT}), Eq. (3.1-11), as a perturbation on the total Hamiltonian, Eq. (2.1-1), including the kinetic energy and the elastic energy associated with the motion of the ligands, Eqs. (3.2-1) and (3.2-6).

Since H_{JT} includes electronic and vibrational operators, vibronic states must be constructed, i.e., states which are symmetry adapted linear combinations of electronic and

and vibrational product states, e.g.,

$$|\Psi^N(\Gamma_j \Gamma_k)\rangle = \sum_{n_\theta, n_\epsilon}^N \sum_i a_i(n_\theta, n_\epsilon) |\varphi_i(\Gamma_j)\rangle |n_\theta, n_\epsilon\rangle \quad (3.4-1)$$

Where Γ_j refers to the representation of the electronic function, Γ_k refers to the representation of the vibronic function, n_θ and n_ϵ are vibrational quantum occupation numbers, and $N = n_\theta + n_\epsilon$. The electronic functions are given in Appendix B and the $a_i(n_\theta, n_\epsilon)$ are coupling coefficients tabulated by Koster et al.⁹ for the octahedral group for the case of one excited quantum of vibration. The Q_n terms in H_{JT} can be converted to a second quantized form by means of the quantum mechanical operators "a[†]" which creates a phonon and "a" which annihilates a phonon, by making the replacement

$$Q_n = (\hbar/2\mu\omega)^{\frac{1}{2}} (a_n^\dagger + a_n) \quad (3.4-2)$$

where $n = e, \epsilon$ or ξ, η, ζ .

We see that the vibrational operator Q_n has non-zero matrix elements only between no-phonon states ($n_n = 0$) and one-phonon states ($n_n = 1$). In the absence of a JT effect, each one-phonon state lies at an energy $\hbar\omega_E$ or $\hbar\omega_T$ above the corresponding no-phonon state depending on which type of mode is excited. Fig. 3.7 shows the vibronic energy levels for $T_{2g} \times t_{2g}$ with several vibrational quanta excited as a function

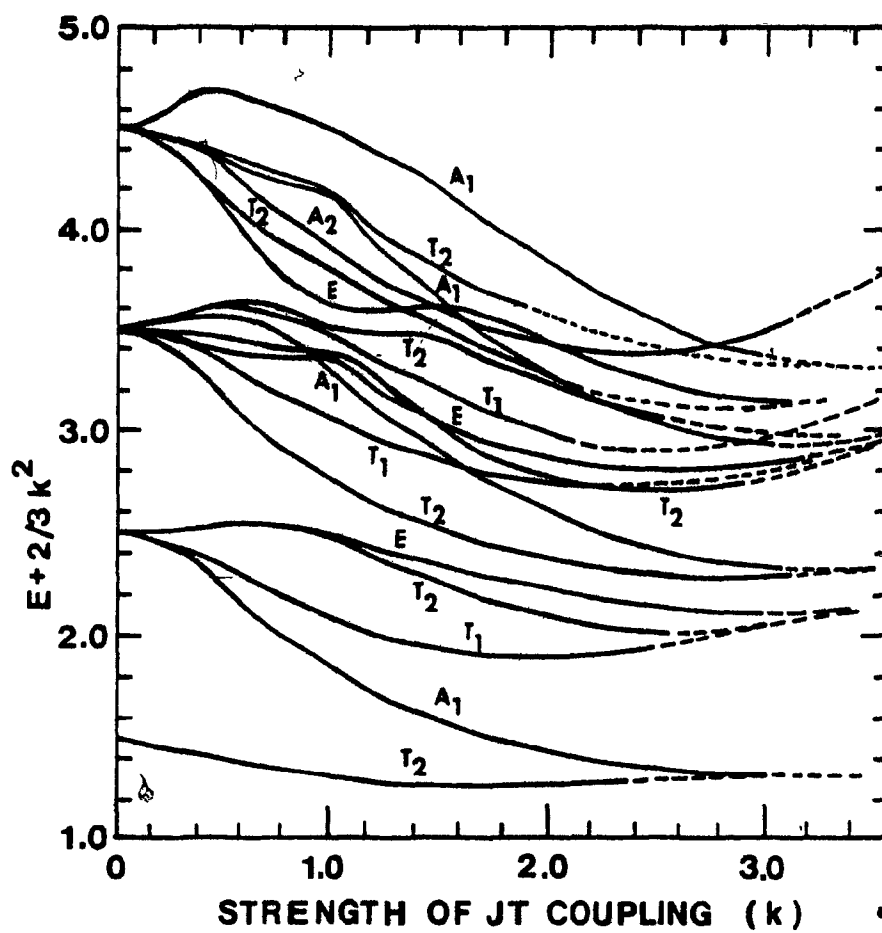


Fig. 3-7

The vibronic energy levels resulting from the interaction of a T_{2g} electronic state with t_{2g} vibrations. In this case, $k = V_T / (\mu \hbar \omega_T)^{\frac{1}{2}}$. (After ref. 85)

of the JT energy. The linear combination of irreducible representations into which each one-phonon state can be decomposed, Table 3.1, is given by the space product $\Gamma_i \times \Gamma_j$ where Γ_i is the representation of the corresponding no-phonon vibronic state and Γ_j is the vibrational mode representation. The one-phonon vibronic states have degeneracy higher than what is allowed under O_h symmetry and, consequently, are split by the H_{JT} in accordance with group theoretical predictions.

The correction to the energy, to second-order of perturbation theory, Eq. (3.4-5), involves matrix elements of H_{JT} in the vibronic states

$$\langle \Psi_n^0(\Gamma_j \Gamma_k) | H_{JT} | \Psi_p^1(\Gamma_j \Gamma_k) \rangle \quad (3.4-3)$$

which transforms according to the representation product

$$\Gamma_k \times \Gamma_1 \times \Gamma_k \quad (3.4-4)$$

where we have used the fact that H_{JT} is a scalar, i.e.,

$\Gamma(H_{JT}) = \Gamma_1$. Moreover, the matrix element, (3.4-3), must be a scalar for the correction to the energy to be a scalar. Consequently, according to the well-known³⁹ group theoretical rule, the identity Γ_1 must appear in the reduction of the representation product (3.4-4) for the matrix element (3.4-3)

to be non-zero. This condition is fulfilled when

$\Gamma_k = \Gamma_k'$ in (3.4-4), which means that H_{JT} has non-zero matrix elements only between vibronic states of identical symmetry.

In this case, group theory reduces considerably the number of terms to be calculated in the summation of Eq. (3.4-5) and shows that the transformation properties of the perturbed vibronic functions (Eq. (3.4-7)) are conserved.

3.4.2 The reduction in the spin-orbit splitting

Since H_{JT} is linear in Q_n which have non-zero matrix elements between vibrational states of different occupation number, the perturbation calculation must be carried out to second-order in V_E and V_T . Consequently, the correction to the unperturbed energies, Eqs. (2.3-10a) to (2.3-10f), is expressed as

$$\Delta E_n = \sum_p \frac{|\langle \Psi_n^0(\Gamma_j, \Gamma_k) | H_{JT} | \Psi_p^1(\Gamma_j', \Gamma_k') \rangle|^2}{E_n - E_p} \quad (3.4-5)$$

where n and p label the different no-phonon and one-phonon vibronic states, respectively, and their corresponding energies.

This correction to the energy can be separated in two contributions, one from the E_g -modes of vibration and the other from the T_{2g} -modes of vibration, as specified in subsection 3.2.4.

The corrections to the energy for the three lowest states are, in agreement with Ham's results³⁵,

$$E(a_1^2 e_g) = -(E_{JT})_E F_1(\omega_E) - \frac{3}{2}(E_{JT})_T F_2(\omega_T) \quad (3.4-6a)$$

$$E(e_g) = -(E_{JT})_E F_3(\omega_E) - \frac{3}{2}(E_{JT})_T F_4(\omega_T) \quad (3.4-6b)$$

$$E(a_1^2 e_g) = -(E_{JT})_E F_5(\omega_E) - \frac{3}{2}(E_{JT})_T F_6(\omega_T) \quad (3.4-6c)$$

where the following definitions apply

$$F_1(\omega) = \frac{1}{100} + \frac{3}{20} \frac{\hbar\omega}{\hbar\omega+198} + \frac{27}{50} \frac{\hbar\omega}{\hbar\omega+501} + \frac{3}{10} \frac{\hbar\omega}{\hbar\omega+492}$$

$$F_2(\omega) = \frac{1}{100} + \frac{1}{10} \frac{\hbar\omega}{\hbar\omega+192} + \frac{1}{20} \frac{\hbar\omega}{\hbar\omega+198} + \frac{1}{5} \frac{\hbar\omega}{\hbar\omega+480} + \frac{2}{5} \frac{\hbar\omega}{\hbar\omega+492} + \frac{6}{25} \frac{\hbar\omega}{\hbar\omega+501}$$

$$F_3(\omega) = \frac{1}{2} + \frac{1}{2} \frac{\hbar\omega}{\hbar\omega+288}$$

$$F_4(\omega) = \frac{1}{4} + \frac{3}{20} \frac{\hbar\omega}{\hbar\omega-192} + \frac{1}{2} \frac{\hbar\omega}{\hbar\omega+300} + \frac{1}{10} \frac{\hbar\omega}{\hbar\omega+309}$$

$$F_5(\omega) = \frac{1}{4} + \frac{3}{20} \frac{\hbar\omega}{\hbar\omega-198} + \frac{1}{2} \frac{\hbar\omega}{\hbar\omega+294} + \frac{1}{10} \frac{\hbar\omega}{\hbar\omega+303}$$

$$F_6(\omega) = \frac{1}{4} + \frac{1}{8} \frac{\hbar\omega}{\hbar\omega-6} + \frac{1}{20} \frac{\hbar\omega}{\hbar\omega-198} + \frac{8}{15} \frac{\hbar\omega}{\hbar\omega+303}$$

The energy difference between the no-phonon states is given in reciprocal centimeters, Eq. (2.3-10).

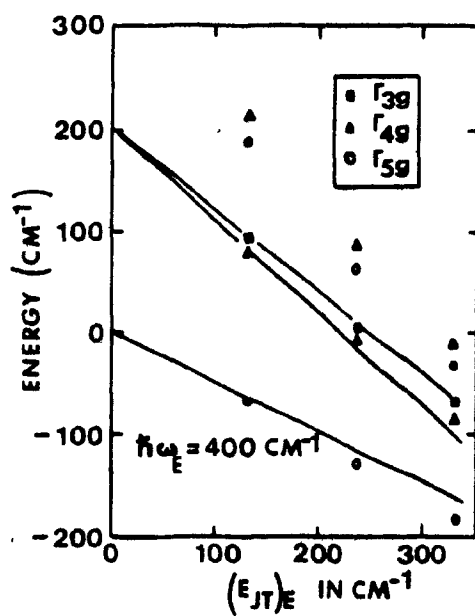
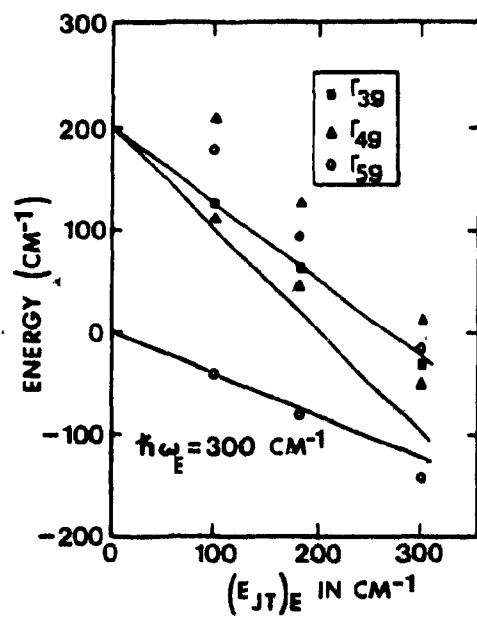
We observe that the three lowest vibronic energy levels are simply shifted (lowered) by the JT interaction. This is to be expected, according to group theory, since the JT Hamiltonian is totally symmetric under the transformations of the octahedral group and cannot split states spanning an irreducible

representation of the same group. Figures 3.11 and 3.13 show the shift of the energy levels for given values of V_E , V_T , $\hbar\omega_E$ and $\hbar\omega_T$, according to Eqs. (3.4-6). These figures also show the reduction in the spin-orbit splitting which is mainly due to the different Ham reduction factors for the different spin-orbit states. The frequency dependent terms of each $F_i(\omega)$, Eqs. (3.4-6), give approximately the same contribution, but the constant terms, given by the appropriate Ham reduction factors squared (except for $F_3(\omega)$), determine the relative magnitude of each $F_i(\omega)$ and, thus, the relative magnitude of the shift.

Ham et al³⁵ verified the accuracy of this perturbation approach by direct numerical diagonalization of the energy matrix for the case in which the JT interaction is with the E_g -modes alone. They used eigenstates of the unperturbed Hamiltonian which had fewer than four vibrational quanta excited. Their results are shown in Fig. 3.8 for two different vibrational quanta, 300 cm^{-1} and 400 cm^{-1} . As mentioned in chapter 4, a typical vibrational quantum lies in the range 300 cm^{-1} to 400 cm^{-1} . For increasing value of the JT energy,

Fig. 3-8

Shift in the spin-orbit energy levels versus the strength of the Jahn-Teller interaction with one E_g -vibrational mode. The solid lines represent the ground state and the first two excited states, as calculated from the second-order perturbation treatment of H_{JT} . The points indicate the same levels calculated from a direct numerical diagonalization of the energy matrix. The states had fewer than four vibrational quanta excited. The calculations were made for a spin-orbit-parameter $\lambda = 100 \text{ cm}^{-1}$ and an effective mode energy (A) $\hbar\omega_E = 300 \text{ cm}^{-1}$ and (B) $\hbar\omega_E = 400 \text{ cm}^{-1}$. Second-order spin-orbit splitting of the energy levels is neglected (After ref.35).



the perturbation approach will break down sooner for $\hbar\omega$ smaller than 300 cm^{-1} owing to the terms involving an energy difference in $F_i(\omega)$ with $i = 4, 5, 6$. The magnitude of these terms increases rapidly as the denominator tends to zero, and their contributions to the correction in energy is exaggerated compared to the contributions from other terms. These authors³⁵ concluded that the perturbation approach is accurate in estimating the reduced energy separation of the spin-orbit states out to $E_{JT} \approx 200 \text{ cm}^{-1}$. As is shown in chapter 5, we obtain JT energies well below this breakdown limit, therefore justifying the use of perturbation theory.

3.4.3 Reduced Ham factors

The JT interaction affects the Ham reduction factors, Eqs. (3.3-3) and (3.3-7), in perturbing to first-order, the no-phonon vibronic functions used to define those reduction factors. According to second-order perturbation theory, the perturbed functions are written

$$|\Psi(\Gamma_j \Gamma_k)\rangle = |\Psi^0(\Gamma_j \Gamma_k)\rangle + \sum \frac{\langle \Psi^0(\Gamma_j \Gamma_k) | H_{JT} | \Psi^0(\Gamma_j \Gamma_k) \rangle}{E^0(\Gamma_j \Gamma_k) - E^0(\Gamma_j \Gamma_k)} \cdot |\Psi^0(\Gamma_j \Gamma_k)\rangle \quad (3.4-7)$$

where $|\Psi^0(\Gamma_j \Gamma_k)\rangle$ is the unperturbed vibronic state defined in

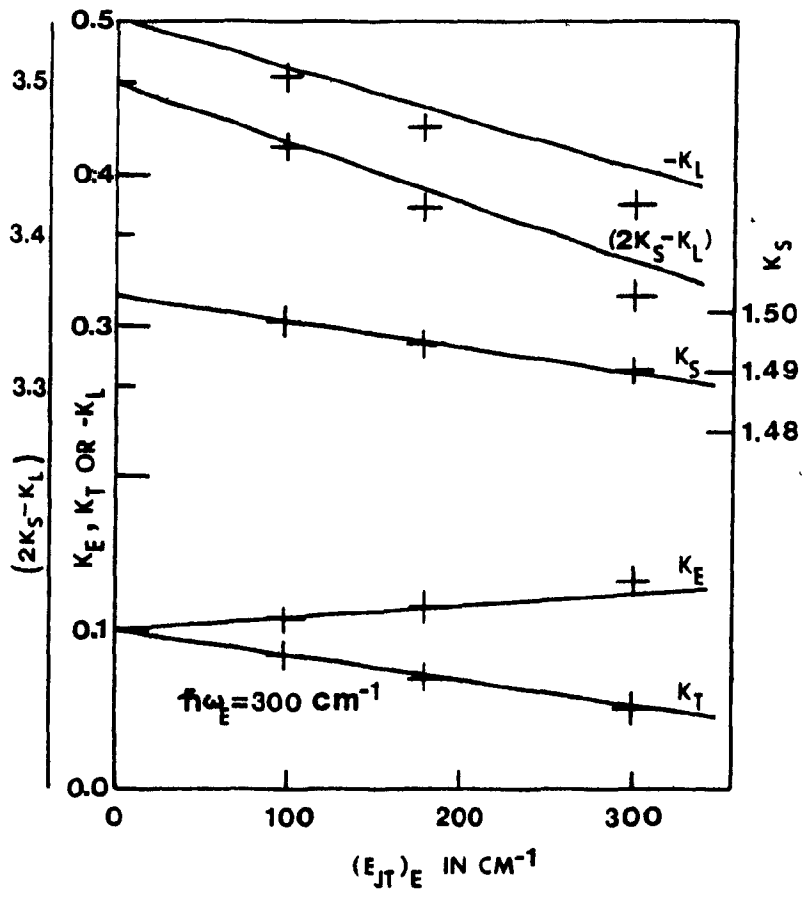
Eq. (3.4-1) and $E^0(\Gamma_j \Gamma_k)$ is the associated energy. A perturbed function including corrections to all orders of perturbation becomes the Glauber state mentioned in subsection 3.2.2. The perturbed Ham reduction factors are obtained by recalculating the matrix elements in Eqs. (3.3-3) and (3.3-7), using the perturbed vibronic functions, Eq. (3.4-7). The perturbed Ham factors are given in Appendix D.

Ham et al³⁵ compared the reduction factors evaluated from the eigen-states obtained in a direct matrix diagonalization with the results of perturbation theory. The comparison is shown in Fig. 3.9 where good agreement is obtained between the two calculation techniques. This figure shows that the reduction factor K_g for the spin is weakly perturbed by the JT effect, whereas the reduction factor K_L is diminished significantly (~20%) from its crystal field value -0.5, indicating a partial quenching of the orbital angular momentum.

Figure 3.10 shows the behavior of the reduction factors K_E and K_T for the three lowest spin-orbit states ($a\Gamma_{5g}$, Γ_{3g} and $a\Gamma_{4g}$) for both coupling to E_g modes and T_{2g}

Fig. 3-9

Reduction factors K_E , K_T , K_L and K_S for the Γ_{5g} ground state of the ferrous ion versus the strength of the Jahn-Teller interaction with one E_g -vibrational mode. The solid lines represent the calculations from second-order perturbation treatment of H_{JT} . The crosses indicate the results of a direct numerical diagonalization of the energy matrix. The eigenstates had fewer than four vibrational quanta excited. The combination $2K_S - K_L$ gives the ground-state g -factor when covalent effects and higher order corrections are neglected. (After ref. 35).



modes. (The parameters used in the calculation are given in the figure caption). In this case, the coupling to E_g modes is stronger, resulting in an important reduction of $K_T(2) \sim 24\%$ by the JT effect at $(E_{JT})_E = 100 \text{ cm}^{-1}$, and a 15% reduction for $K_E(2)$ at the same JT energy. The reductions are less severe in the a Γ_{5g} ground state with 4% for $K_E(1)$ and 14% for $K_T(1)$. Fig. 3.11 shows the shift of the energy levels and the reduced spin-orbit splitting obtained from the same parameters used in Fig. 3.10. It is interesting to note the reduced second-order spin-orbit splitting between the Γ_{4g} and the Γ_{3g} levels as was observed by Meyer et al⁴⁰.

The reduction factors K_E and K_T , in Fig. 3.12, result from a slightly stronger coupling to T_{2g} modes and a weaker coupling to E_g modes. In this case, where we have almost equal coupling to both modes of vibration, K_E and K_T are diminished by a comparable amount by the JT effect showing the independent stabilization of their respective distortions. A comparison of Fig. 3.10 and 3.12 shows that the stronger coupling always dominates the picture, as discussed in subsection 3.2.4. Fig. 3.13 shows the shifts of the energy levels and the reduced spin-orbit splitting obtained from the parameters

Fig. 3-10

The magnitude of the Ham reduction factors (K_E and K_T) versus the strength of the Jahn-Teller interaction. The effective mode energies $\hbar\omega_E = 345 \text{ cm}^{-1}$ and $\hbar\omega_T = 303 \text{ cm}^{-1}$ are used in the calculation, as explained in the text.

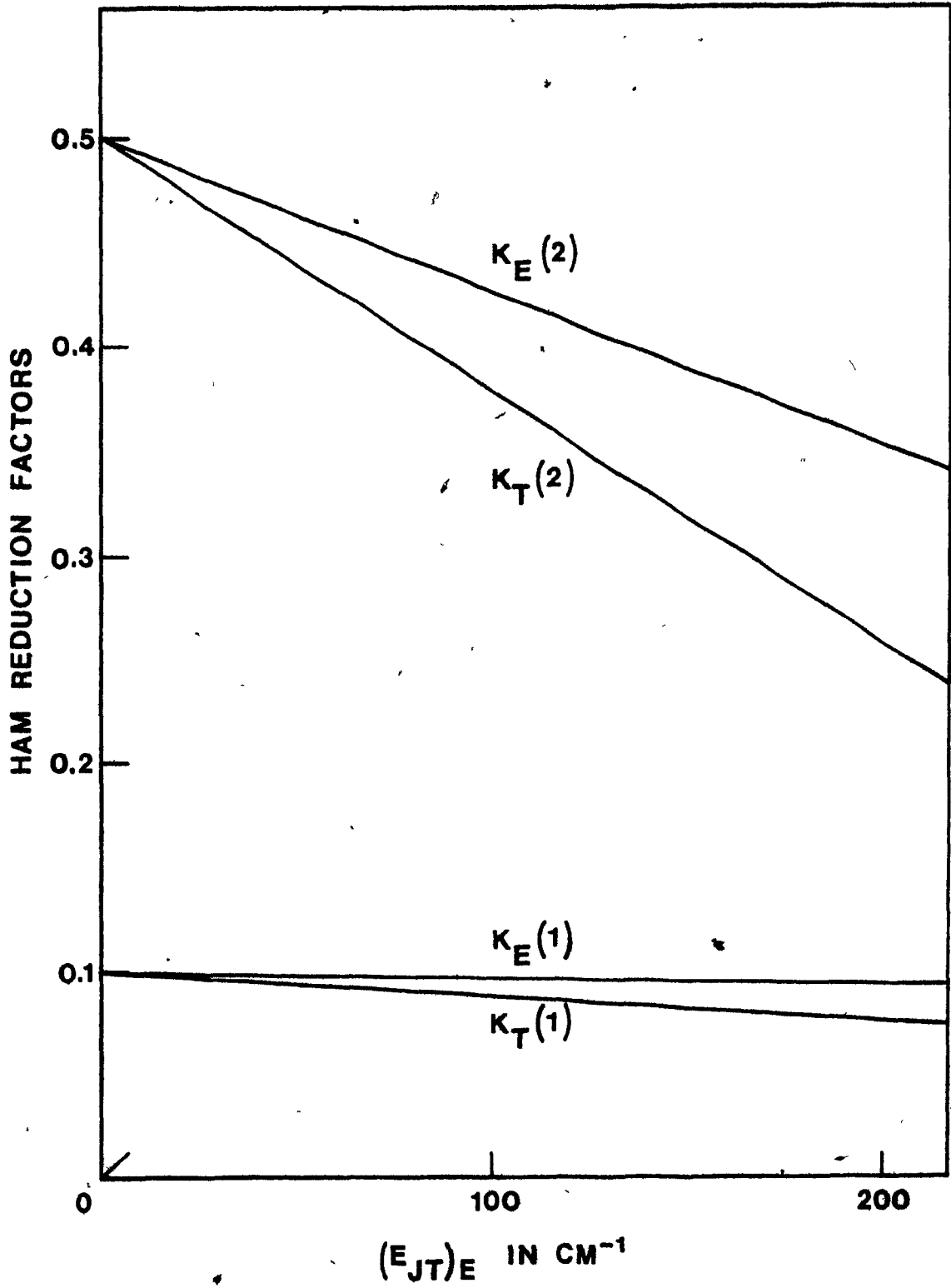
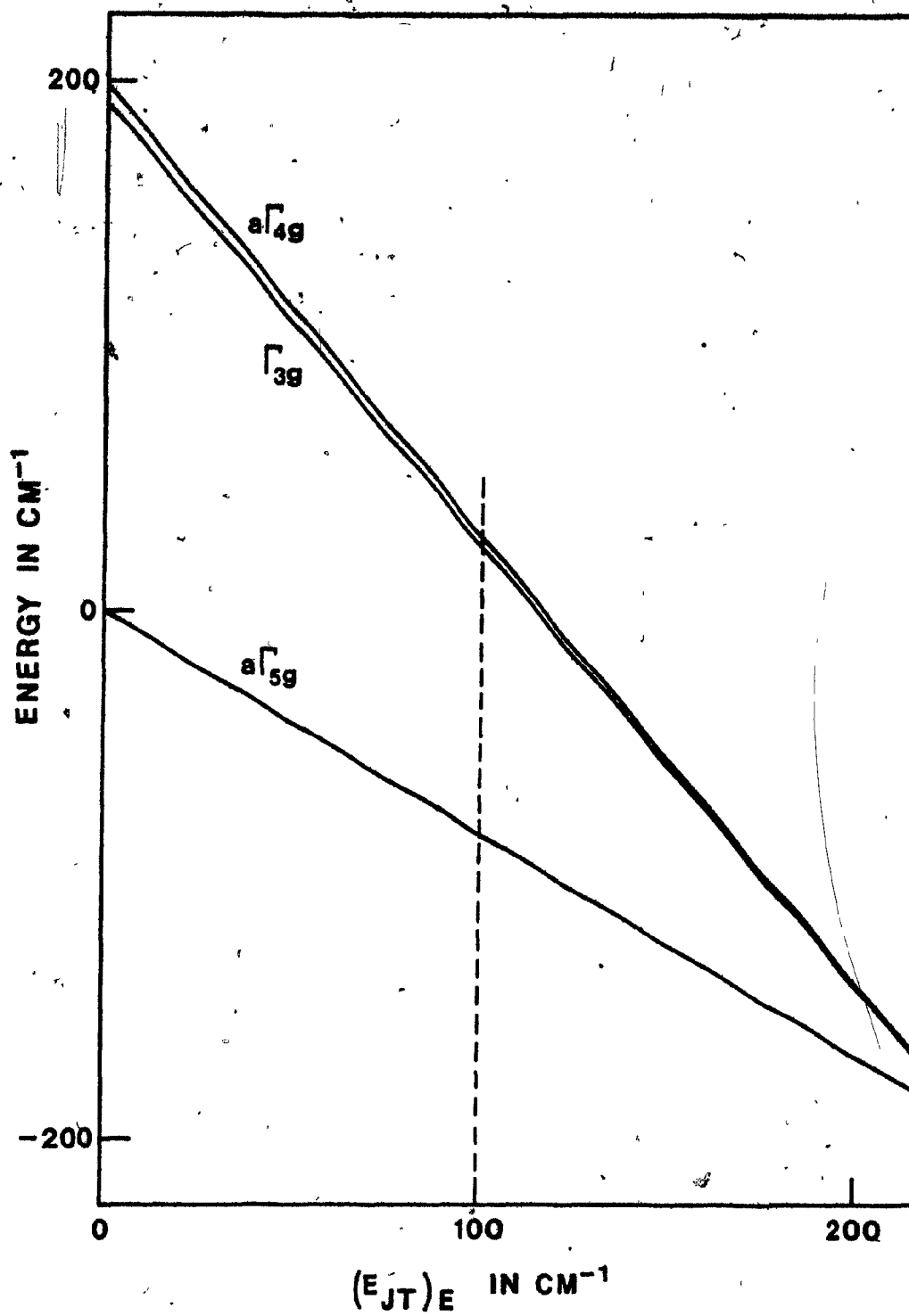


Fig. 3-11

The shift in the spin-orbit energy levels versus the strength of the Jahn-Teller interaction. The effective mode energies $\hbar\omega_E = 345 \text{ cm}^{-1}$ and $\hbar\omega_T = 303 \text{ cm}^{-1}$ are used in the calculation, as explained in the text. The vertical dash line indicates the JT energy, $(E_{JT})_E$, which fits best the experimental results.



of Fig. 3.12. Fig. 3.11 and 3.13 are remarkably similar which contrasts with the marked difference between the related figures 3.10 and 3.12. In other words, many different kind of coupling strength to E_g and T_{2g} modes can fit the experimental results of Wong (cf. chapter 4) indicated by a vertical dashed line on each figure.

Fig. 3.14 indicates how the g-factor can be made to agree with the reduced spin-orbit splitting simply by adjusting the parameter k in Eq. (3.3-6) which accounts for the covalent effect. To obtain unambiguously the respective coupling strength to E_g and T_{2g} modes of vibration, new experimental evidence is required. Such new evidence is provided from the determination of the strain coupling coefficients, as described in chapter 5.

Fig. 3-13

The magnitude of the Ham reduction factors (K_E and K_T) versus the strength of the Jahn-Teller interaction. The effective mode energies $\hbar\omega_E = 345 \text{ cm}^{-1}$ and $\hbar\omega_T = 400 \text{ cm}^{-1}$ are used in the calculation, as explained in the text.

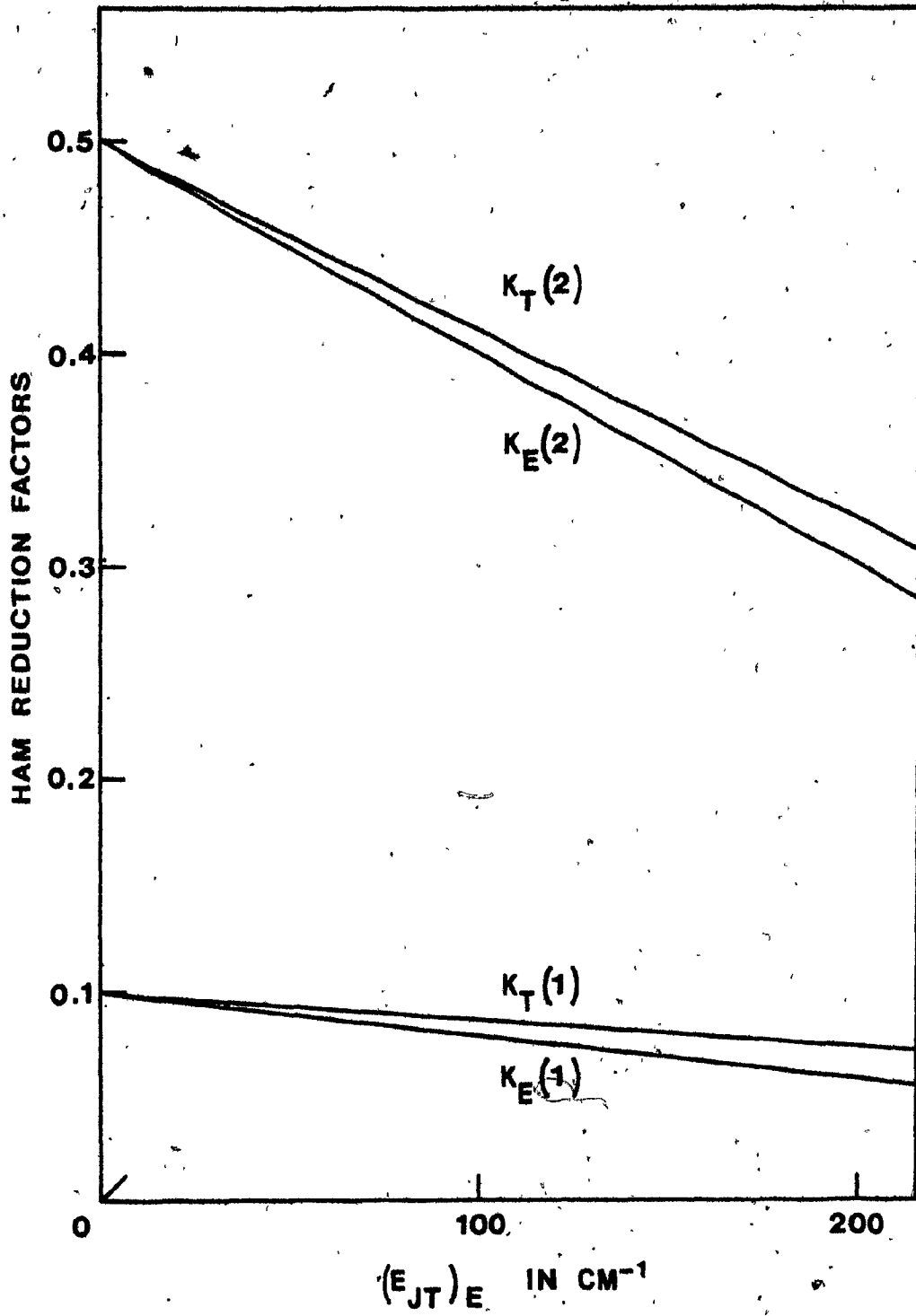


Fig. 3-13

The shift in the spin-orbit energy levels versus the strength of the Jahn-Teller interaction. The effective mode energies $\hbar\omega_E = 345 \text{ cm}^{-1}$ and $\hbar\omega_T = 400 \text{ cm}^{-1}$ are used in the calculation, as explained in the text. The vertical dash line indicates the JT energy, $(E_{JT})_E$, which fits best the experimental results.

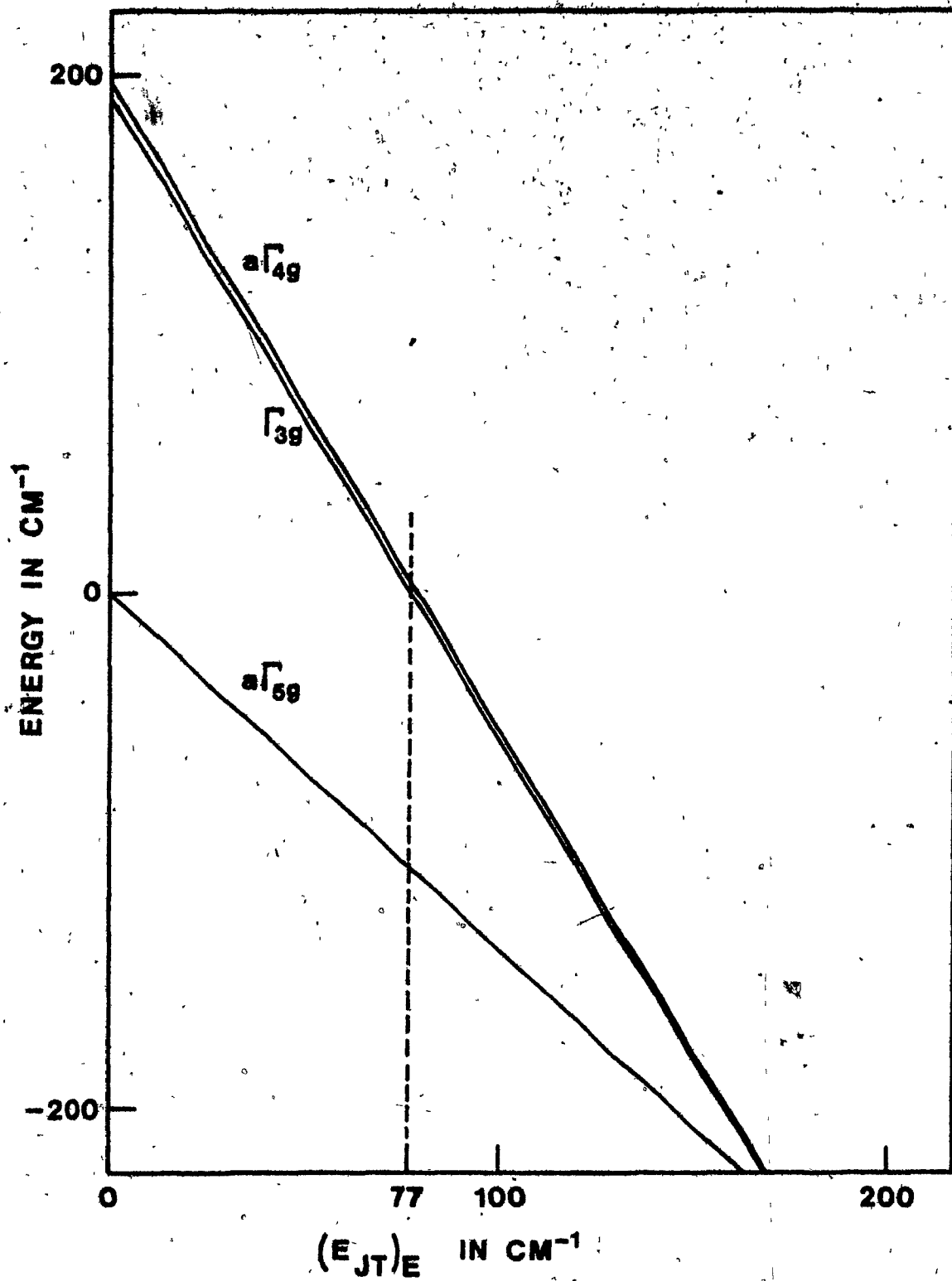
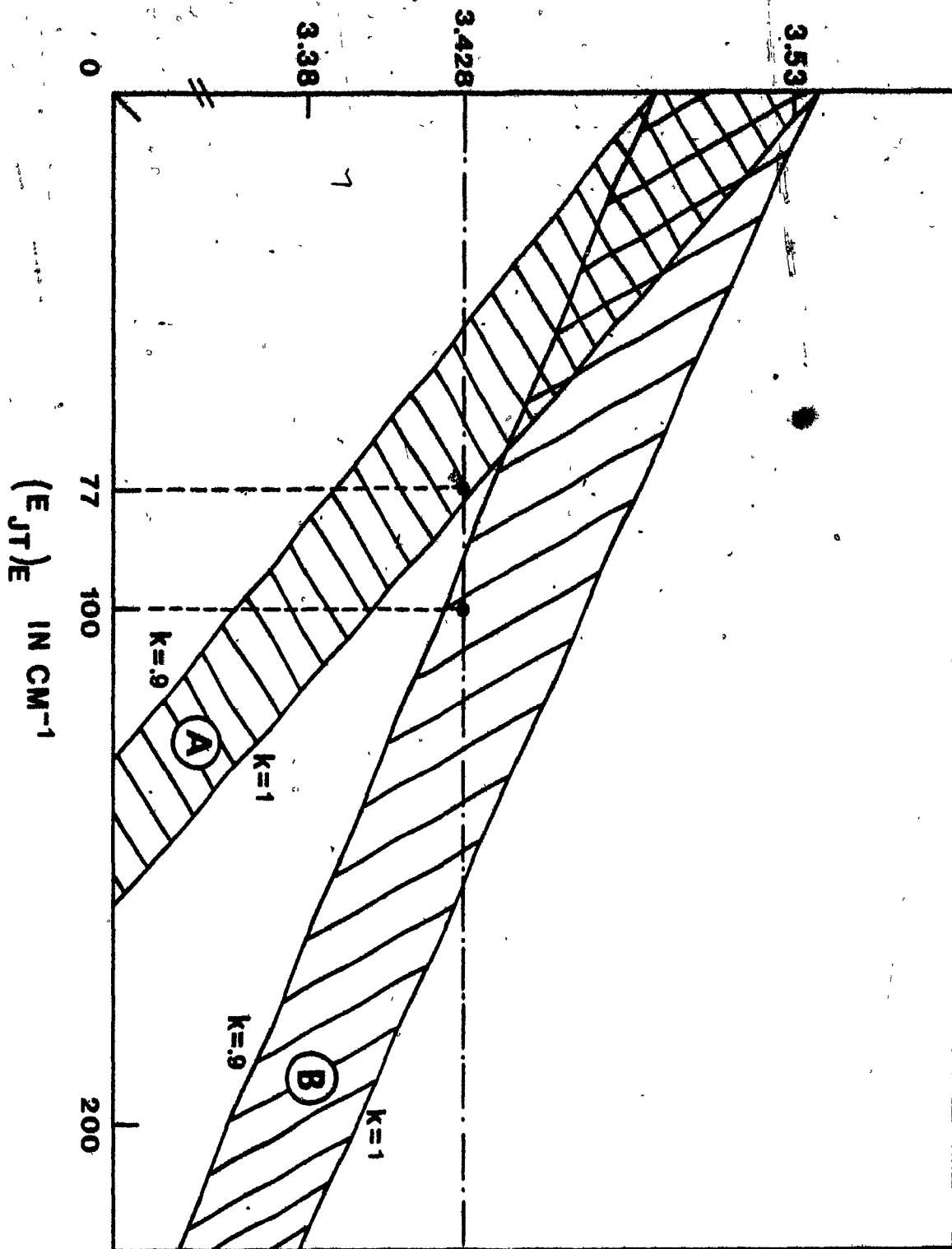


Fig. 3-14

The magnitude of the electronic g-factor versus the strength of the Jahn-Teller interaction. Two curves, A and B, are calculated using the effective mode energies given in Figs. 3-13 and 3-11, respectively. For each curve, the parameter k (covalent effects) is varied from 1 to 0.9. The dash-dot line indicates the experimental value ($g = 3.428$) and the dash lines show agreement with the results of Figs. 3-13 and 3-11.

ELECTRONIC G-FACTOR



CHAPTER 4

THE EXPERIMENTAL RESULTS

4.1 The literature review

4.1.1 The direct evidence

The direct measurement of the energy separation between the ground state and the first excited states of the ferrous ion in MgO by far infrared optical absorption was first reported by Wong and Schawlow^{41,42} in 1967. They investigated the energy range from 10 to 220 cm^{-1} for two samples of $\text{MgO}:\text{Fe}^{2+}$ having different iron concentrations. At a temperature of 20K, they observed an absorption peak 9 cm^{-1} in width at an energy of 105 cm^{-1} . Reduction, oxidation and X-ray irradiation data together with a direct relationship between Fe^{2+} concentration and line strength confirmed the origin of the peak as due to the presence of ferrous ions in the MgO crystal. The absorption peak was attributed to the magnetic dipole transitions $\Gamma_{5g} \rightarrow \Gamma_{3g}$ and Γ_{4g} . Crystal field theory² predicts, however, a spin-orbit splitting of 200 cm^{-1} and an energy separation of 6 cm^{-1} between the first excited states Γ_{3g} and Γ_{4g} . Since they were not able to resolve the two levels, they concluded that the JT effect is reducing their separation to less than 2 cm^{-1} (spectrometer resolution) and reducing the spin-orbit splitting by 50%.

Ham et al.³⁵ were able to explain the discrepancies in Wong's results from the predictions of crystal field theory as due to the partial reduction of the orbital angular momentum by a weak dynamic JT coupling to two different local modes of vibration. Their approach has been discussed in chapter 3 of this thesis.

Meyer et al.⁴⁰ were able to resolve the two electronic transitions $\Gamma_{5g} \rightarrow \Gamma_{3g}$ and Γ_{4g} , in the far infrared absorption spectrum of $\text{MgO}:\text{Fe}^{2+}$, at 106.9 cm^{-1} and 110.5 cm^{-1} . Hjortsberg et al.^{43,44} studied extensively the shift and the splitting of the two absorption peaks in the presence of a magnetic field. They estimated the oscillator strength of each peak and they concluded that the Γ_{3g} level lies lowest in energy at 106.9 cm^{-1} and the Γ_{4g} level corresponds to the peak at 110.5 cm^{-1} .

Hjortsberg⁴³ and Manson et al.⁴⁵ observed a hot line at 90K in the near infrared absorption spectrum of $\text{MgO}:\text{Fe}^{2+}$ which appeared 105 cm^{-1} from the ${}^5\text{T}_{2g} \rightarrow {}^5\text{E}_g$ zero-phonon line, Fig. 2.2. The hot line is attributed to infrared absorption from the first excited states (Γ_{3g} and Γ_{4g}) which are sufficiently populated at 90K for the transition to be observed.

Therefore, the existence of electronic states of the ferrous ions in MgO at $\sim 110 \text{ cm}^{-1}$ is well established by infrared optical absorption. As we will see in the following

subsection, the observed spin-orbit splitting is confirmed by other experimental techniques.

4.1.2 The inferred evidence

Pipkorn and Leider⁴⁶ observed a quadrupole doublet in the Mossbauer spectrum of the ferrous ion in MgO at $T < 14K$. They proposed, for $T < 14K$, that a static JT deformation of the cluster surrounding the ferrous ion was at the origin of the electric field gradient producing the quadrupole splitting. For $T > 14K$, a dynamical JT effect was believed to dominate the situation producing a time average octahedral symmetry leading to the so-called motional narrowing of the spectrum. Ham⁴⁷ showed, however, that the electric field gradient produced at the nucleus by the valence electrons of the ferrous ion, the presence of random strains⁴⁸ in the MgO crystal which split the Γ_{5g} ground state and suitably long electronic relaxation times could very well explain the appearance of a quadrupole doublet at sufficiently low temperature. Consequently, no strong JT effect is required to explain the motional narrowing at $T > 14K$, but rather rapid electronic transitions among the three strain-split states of the Γ_{5g} ground state of Fe^{2+} . For instance, rapid reorientation of the valence electrons around the nucleus with respect to the quadrupole precession time produces an isotropic electric field at the nucleus leading to a vanishing splitting. Ham calculated the electronic transition time τ via the transition probability P per unit time, since $\tau = 1/3P$, for phonon-induced transitions between two

of the strain-split Γ_{5g} states. Ham found that the most likely process for such a transition is an Orbach process⁴⁹ (i.e., resonant Raman process) through the first excited spin-orbit states, Γ_{3g} and Γ_{4g} . The transition probability for this process is proportional to an exponential term of the form,

$$P \propto \exp(-\Delta/kT) \quad (4.1-1)$$

where Δ is the spin-orbit splitting between the ground state and the first excited states. On the basis of this model, Ham adjusted Δ in Eq. (4.1-1) so that P gives an electronic transition time which would explain the disappearance of the quadrupole splitting at $T > 14K$. Ham's result of $\Delta = 95 \text{ cm}^{-1}$ is the first experimental prediction of the reduction in the spin-orbit splitting with respect to the predicted crystal field value of 200 cm^{-1} . Leider and Pipkorn⁵⁰ studied the Mossbauer spectrum of $\text{MgO}:\text{Fe}^{2+}$ extensively and obtained a spin-orbit splitting of 93 cm^{-1} in good agreement with Ham's estimate. Ham's way of extracting the spin-orbit splitting from the relaxation time lead to a series of new experiments. For instance, electron spin resonance studies^{51,52} of Fe^{2+} in MgO showed that the spin-relaxation time at $T > 8K$ can be described by a phonon-relaxation process involving an electronic excited state of energy $100 \pm 10 \text{ cm}^{-1}$ above the ferrous ion ground state. Although less accurate, this energy separation corroborates the previous results for Δ .

King et al.⁵³ measured the microwave acoustic attenuation in samples of iron doped MgO as a function of temperature. From the temperature dependent relaxation time which is determined from an analysis of the form of the attenuation peak of a [100]-propagating compressional wave, they were able to predict the existence of an electronic excited state at $110 \pm 2 \text{ cm}^{-1}$ above the ground state of the ferrous.

A marked minimum in the thermal conductivity of $\text{MgO}:\text{Fe}^{2+}$ at 80K, was found by Morton and Lewis⁵⁴ to correspond to the resonant scattering of phonons of energy 105 cm^{-1} interacting with two sets of magnetic levels of the ferrous ion.

It is interesting to note that the discrepancy in the relative energy of the first excited states of the ferrous ion, Γ_{3g} and Γ_{4g} , measured by infrared optical absorption as compared with the results from Orbach spin-lattice relaxation rates or from the Mossbauer experiments can be accounted for by the effect of finite width⁵⁵ of the excited levels. The existence of electronic levels of the ferrous ion at 110 cm^{-1} is now well accepted but, however, not much knowledge has been gained as to the kind and strength of the JT coupling. This matter will be discussed in chapter 5.

4.1.3 The vibrational spectrum of MgO crystal

Mon⁵⁶ obtained for the first time in 1965, the second-order vibrational Raman spectrum of pure MgO samples. Shortly

after, Mon⁵⁷ was also successful in recording the first-order vibrational Raman spectrum induced by ferrous ion impurities in MgO. The first-order Raman spectrum is observed only when the translation property of the crystal lattice is perturbed by the presence of a defect, e.g., an impurity site. Billat et al.^{58,59} studied extensively the first-order vibrational Raman spectrum of iron doped MgO crystal and observed, among other things, a broad structured band extending from 100 cm^{-1} to 350 cm^{-1} which peaks at 180 cm^{-1} . The band is observed for both MgO:Fe^{3+} and MgO:Fe^{2+} showing that the modification of the force constants between nearest neighbors is the same for both types of iron ions, in agreement with the observation of Low and Weger², which leads to the assignment of a A_{1g} resonance mode at 180 cm^{-1} for MgO:Fe^{2+} . Billat et al.⁵⁹ also observed that the first-order Raman spectrum, in the range 300 cm^{-1} to 450 cm^{-1} , reproduces very well the one-phonon density of state which is mainly of E_g and T_{2g} symmetry in that range.

Wong⁴² and Hjortsberg⁴³ did not observe the A_{1g} resonance mode for the simple reason that vibrational mode of even symmetry are not infra-red active, but Raman active only. In fact, a lattice resonance mode⁶⁰ of vibrational energy 403 cm^{-1} is the only infra-red active vibration reported and is in agreement with the known phonon density of states^{61,62}.

Peckham⁶¹ first measured the phonon dispersion relations in MgO through neutron scattering technique. A more accurate

frequency distribution was obtained by Sangster et al.⁶² which, when compared with the theoretical histogram⁵⁹ of the projected density of states for lattice phonons indicates that the JT active phonons cover the energy range from 300 cm^{-1} to 450 cm^{-1} , Fig. 4.1. As Ham³⁵ suggested, the effective mode frequency is chosen to lie in the region of the peaks of the frequency distribution function for the lattice phonons in MgO crystal.

4.1.4 The g-factor

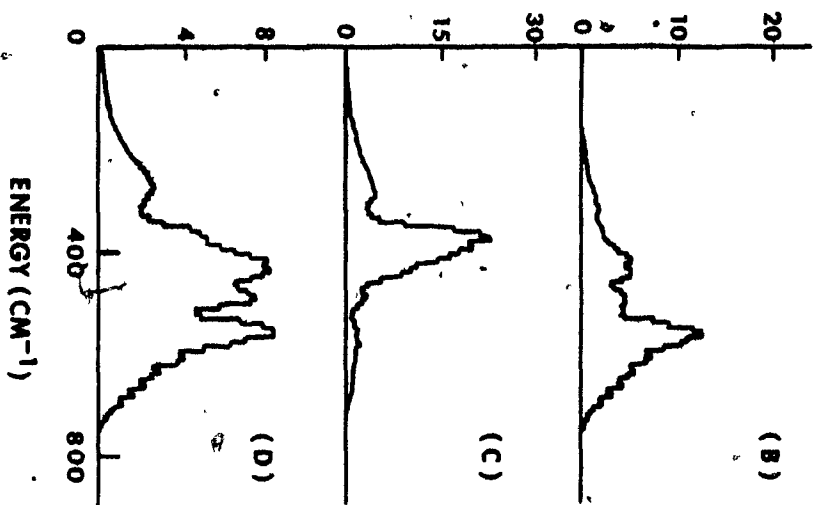
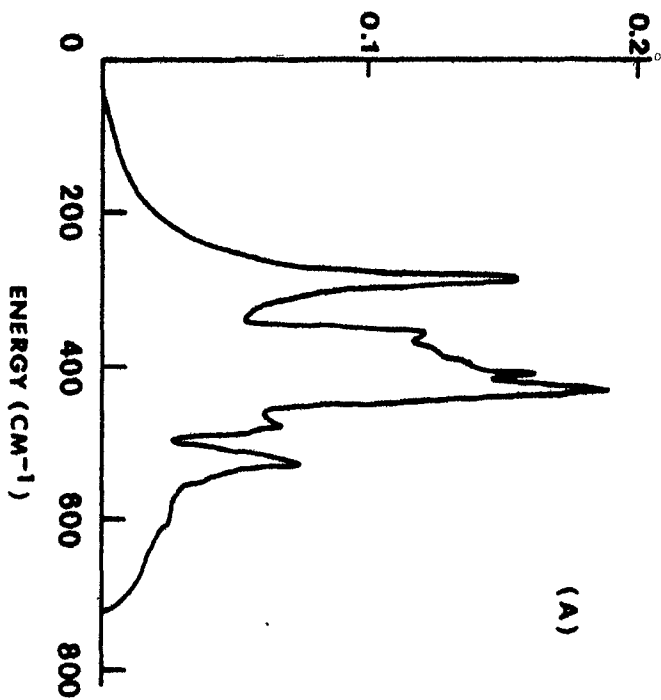
Paramagnetic resonance studies^{2,63} are the earliest works on MgO:Fe^{2+} which demonstrated the existence of a JT effect as a reduction in the g-factor with respect to the value 3.53 predicted² by crystal field theory. However, if there is a strong JT effect, the orbital contribution to the g-factor is quenched and a superposition of anisotropic EPR spectra having $g=2$ should be observed. Moreover, when JT coupling is only to one mode of vibration, the reduction parameters used to account for the 50% reduction in the spin-orbit splitting give $g=3.25$ which disagrees with the experimental value. Ham et al.³⁵ could explain the experimental g-value using a weak dynamic JT coupling to both E_g and T_{2g} modes of vibration and a small covalent bonding^{34,36}.

Acoustic saturation measurements⁶⁴ and acoustic paramagnetic resonance⁶⁵ confirmed the isotropy of the g-factor and give $g = 3.4277$.

Fig. 4-1

- (A) Frequency distribution function as calculated from 2,048,000 points in the Brillouin zone (**neutron scattering data; after ref. 62**).
- (B) Histogram of the projected density of states for unperturbed phonons of A_{1g} , (C) E_g and (D) T_{2g} symmetry for MgO (after ref. 59).

DISTRIBUTION FUNCTION



4.2 The experimental set-up

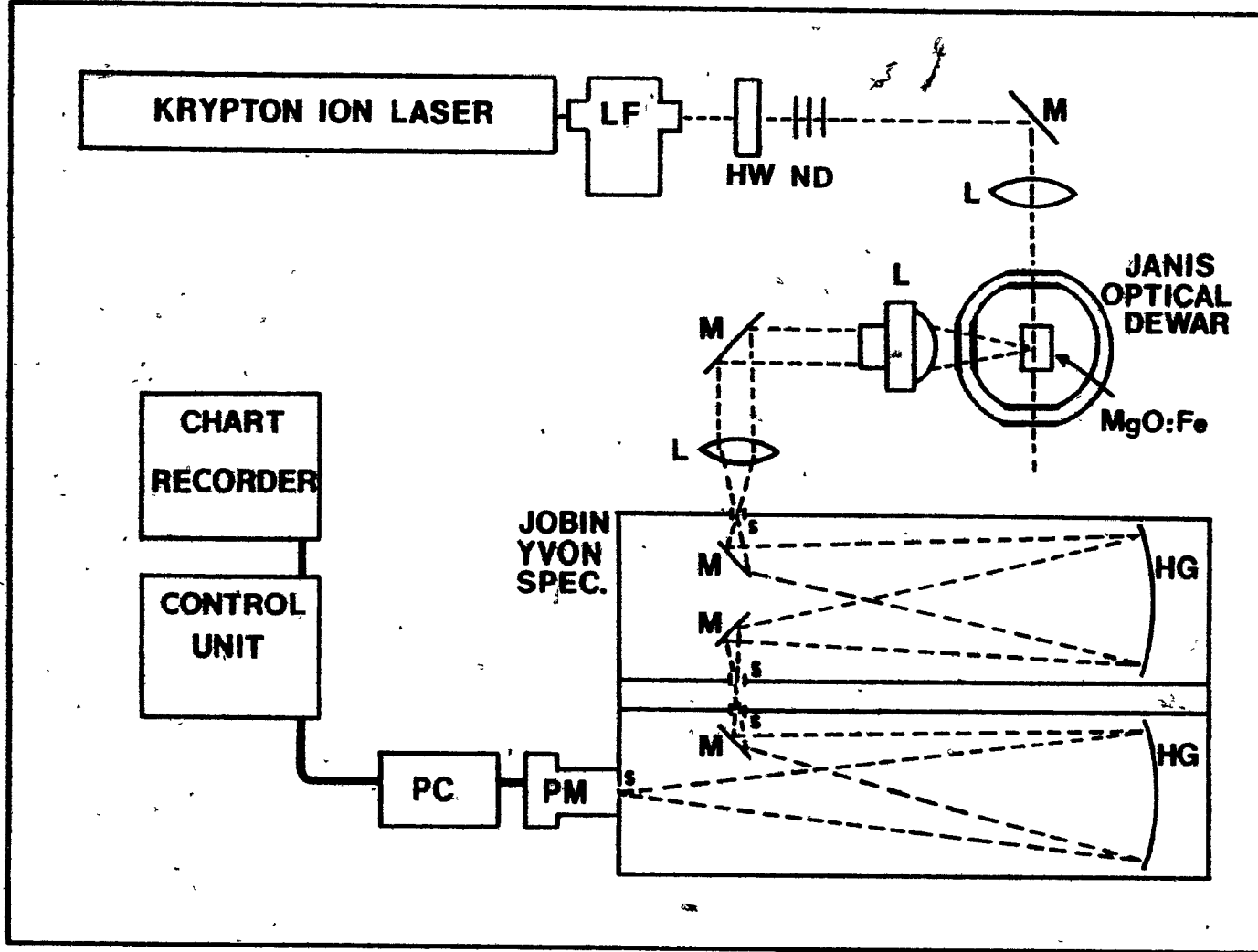
4.2.1 The Raman system

The excitation of the electronic Raman spectrum was by a Spectra Physics 171 krypton ion laser using 200 mW of focused light at 20995 cm^{-1} and 18834 cm^{-1} . The laser beam is passed through an Anaspec 300S laser filter monochromator consisting of six air-glass interfaces providing an 80% power throughput and a 20 cm^{-1} bandwidth which can be set for any wavelength of the visible spectrum. The Anaspec laser filter is required to remove the several plasma lines, inherent in the krypton ion laser, which interfere with the electronic Raman spectrum. The laser tube is provided with Brewster windows which polarize the laser beam vertically. The plane of polarization is rotated at will via a half-wave plate in order to obtain the different scattering geometries required to identify the different electronic transitions or vibrational modes, as discussed in section 4.4. A 90° -scattering geometry was employed, as shown in Fig. 4.2, to avoid the troublesome radiation due to Rayleigh scattering which, otherwise would extend considerably the laser wing and thus obscure the electronic Raman spectrum.

The laser beam is focused in the bulk of the crystal and the scattered light, collected by a $f/8$ optical system having an image magnification of four, is focused on the entrance slit of the spectrometer. The scattered light is

Fig. 4-2

Experimental set-up showing the 90° -scattering geometry employed. The laser beam is filtered by the Anaspec laser filter (LF), its polarization is changed via the half-wave plate (HW) and its intensity is attenuated through the neutral density filters (ND). M and L refer to front surface mirrors and lenses, respectively, both having anti-reflexion coatings. The MgO:Fe sample is cooled down to liquid He temperatures in the Janis optical dewar. The scattered light is analysed by the Jobin Yvon spectrometer. HG and s refer to the holographic gratings and the slits. The scattered photons are detected by the photomultiplier (PM) and photon-counting equipment (PC). The electronic Raman spectrum appears on the chart recorder.



then spectrally analysed using a Jobin Yvon HG 25 double monochromator equipped with holographic gratings of one-meter focal length. An interesting property of the holographic grating is its capability to polarize a light signal, i.e., only the light having its electric vector perpendicular to the ruling of the grating will be diffracted. This property of the holographic gratings eliminated the need of an analyser to polarize the scattered light from the crystal. The spectrometer design includes four electronically controlled slits independently adjustable which achieve a stray light rejection of 10^{-14} at 20 cm^{-1} from the Rayleigh line and 2 cm^{-1} resolution for a 200μ slit width which was used most of the time. The exit slit is directly coupled to a cooled GaAs Hamamatsu R666S photomultiplier tube equipped with standard photon counting equipment. The spectrum scan rate, the sensitivity of the photon counting system and the integration time together with the spectrum chart recorder are adjusted from a control module. The typical background noise of the system using a 4.7s integration time is 10 photon-counts/s.

The crystal, glued by one edge with a drop of Duco cement to prevent an excessive stress to develop, is mounted on a copper sample holder in a Janis 8 DT optical dewar. The sample space can be cooled either by flowing cold He gas or simply by flooding the space with liquid He. The crystal temperature was monitored by a DT-500-KL silicon diode mounted

directly on the copper sample holder. All the experiments were performed at 1.6K in liquid He or at 10K in a reduced atmosphere of He gas with a temperature stability of $\pm 0.5K$. It must be mentioned that laser heating inevitably occurs near the laser beam waist in the crystal and this phenomenon contributes to broadening of the electronic Raman line. This heating effect is minimized, however, by the very good optical quality of the crystal.

4.2.2 The stress apparatus

For the stress experiments, the crystal must be prepared with two parallel surfaces on which the stress will be applied. As a precaution, a piece of computer card and a small amount of grease establish the contact between the parallel surfaces of the crystal and the jaws of the stress apparatus, Fig. 4.3. The gas pressure driven piston applies the stress to the crystal via a steel rod which is supported by the top jaw. The bottom jaw rests on a piezoelectric pressure sensor which is hooked up to a charge detector and amplifier. The pressure sensor calibration was checked using alternatively several pressure regulators which controlled the pressure in the piston chamber. The results of these tests are plotted on Fig. 4.4 where a slope of $10.3 \pm .5$ PSI/V is obtained (at liquid He temperature) in agreement with the 10.0 PSI/V calibration. Therefore, we assume an accuracy of $\pm 5\%$ on the stress quoted in this and the following chapter. Typically, a MgO sample breaks when the stress exceeds 40 KG/MM^2 which explains why this value is never exceeded.

Fig. 4-3

Details of the stress apparatus. The rod which moves freely in its tubular guide carries the pressure from the piston (room temperature) to the sample (liquid He temperature) via the upper jaw. The sample is installed between the upper jaw and the lower jaw. The applied pressure is measured from the pressure sensor. Everything within the box, standing for the Janis optical dewar, is at or near liquid He temperature. The drawing has been simplified and is not drawn to scale.

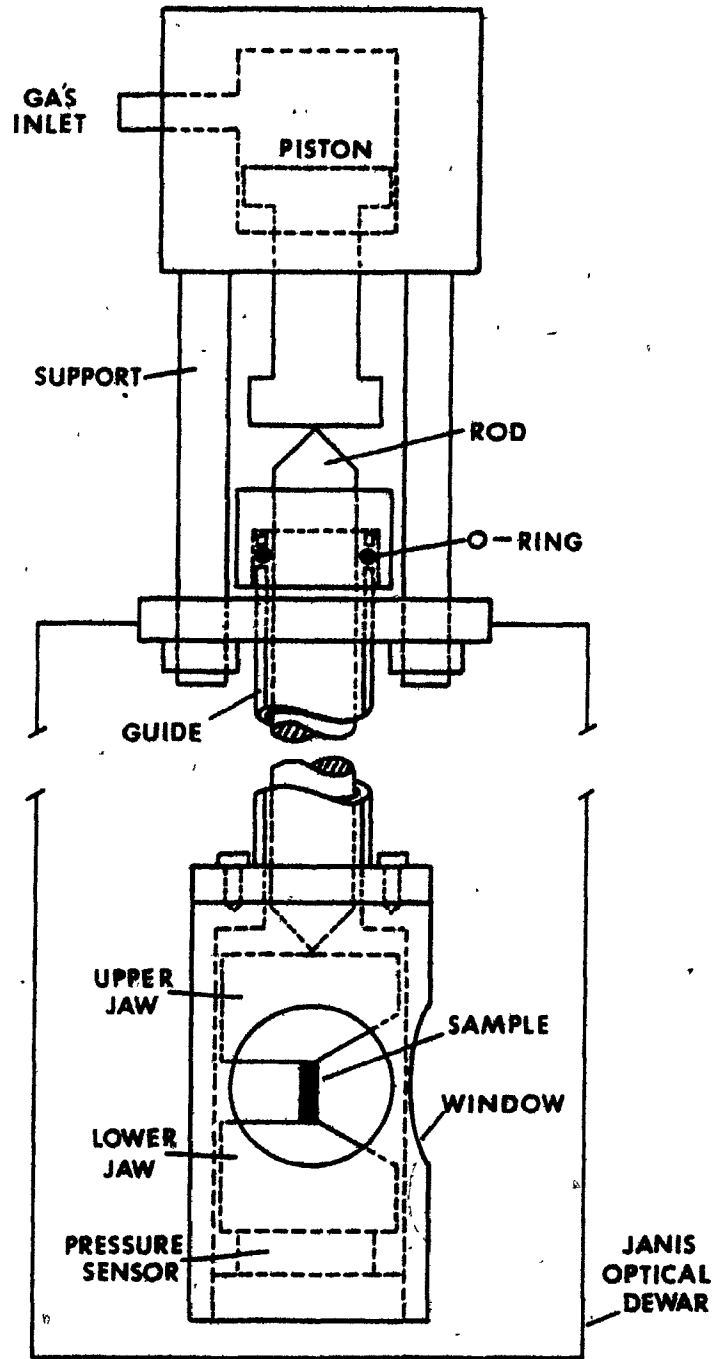
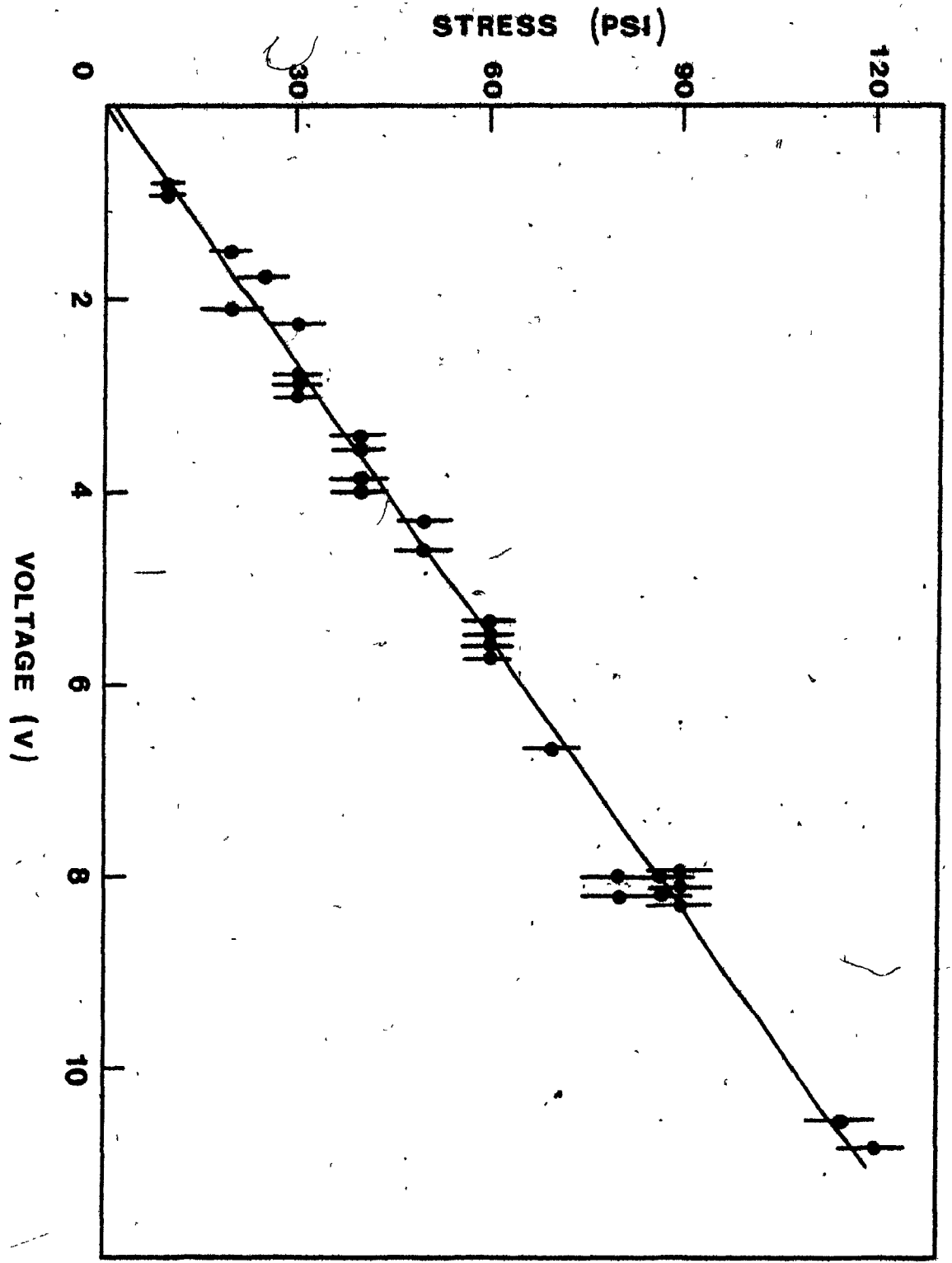




Fig. 4-4

Pressure sensor calibration done at liquid He temperature. The slope calculated from a least square fit is $10.3 \pm .5$ PSI/V.



4.2.3 The iron-doped MgO samples

The iron-doped MgO single crystals employed in these investigations were grown by means of the submerged arc-fusion technique⁶⁶. Doping of the MgO samples was achieved by mixing an appropriate amount of Fe_2O_3 (~1% nominal) with high-purity MgO powder prior to the arc melting process. The optical samples were cleaved from the resulting large ($3 \times 2 \times 1.5 \text{ cm}^3$) single crystal grains. Even though the exact iron concentration is not known, samples with different iron concentration could be distinguished from the yellow tint of the crystal which is darker for higher iron concentration. The electronic Raman peak was observed with the darkest samples only. The electronic Raman signal being so weak (on the 100 photon-counts/s scale) care must be taken not to lose too many photons. Consequently, the surfaces of the sample must be cleaved to obtain a single plane of atoms and, hence, minimize the surface scattering. But, MgO cleaves only along its (100)-plane and, being a very hard material, it is difficult to cleave neatly. So, more often than not the faces of the sample must be polished mechanically down to one micron or less using Al_2O_3 lapping sheets.

In order to obtain the different (100), (110) and (111)-configuration, see Figs. 5.1 to 5.3, an X-ray Laue picture of the crystal is obtained and, then, knowing the orientation of the crystal planes, the crystal is properly cut with a circular diamond saw. The (100) and (110) configurations

are obtained to $\pm 1^\circ$ and the (111) configuration which involves two cutting steps is obtained to $\pm 3^\circ$. Besides, the MgO samples must be prepared with very sharp edges since the laser beam must be focused in the bulk of the crystal very close to the surface facing the optical collecting system to minimize reabsorption and internal scattering of the electronic Raman signal during its travel in the crystal.

The EPR line shape and the zero-phonon line shape of optical spectra were found to be much broader than the expected broadening from spin-spin interaction. In fact, the electronic energy levels are split by internal strains of E and T_2 symmetry in the host crystal. The magnitude of the splitting depends on the type and strength of the strain field at the impurity site of interest. The microscopic strains are caused by several different species of strain source - for example, point defects, straight edges and screw dislocations. Stoneham^{48,67} showed that random strains in the crystal cause a broadening of the line shape, which can be of the order of a few wavenumbers for severe strains⁶⁸. The resulting line shape depends on the statistical distribution of the imperfections and their individual strain field which will be different from sample to sample, depending on the method of formation and on the mechanical history of the crystal investigated.

4.3 The electronic Raman effect

4.3.1 The scattering tensor

The well-known Rayleigh scattering is a first-order process in which the frequency of the photon is preserved, whereas Raman scattering is a second-order process in which a shift in the frequency of the scattered photon with respect to the incident photon is observed. Moreover, compared with the optical infrared absorption which is essentially a direct transition between two discrete energy levels, the Raman scattering is rather an indirect transition from an initial state to a set of probable intermediate (or virtual) states instantaneously followed by a transition down to the final state, Fig. 4.5.

In a crystal, the frequency shift of the Raman scattering is either due to the creation or annihilation of a phonon which characterizes the vibrational Raman scattering, or to the excitation (or deexcitation) of the electronic state of an ion which characterizes the electronic Raman scattering. The first unambiguous observation of electronic Raman scattering was made by Das Gupta⁶⁹, as late as 1959, who had to use the intense and narrow line of an X-ray source owing to the elusiveness of the phenomenon. In the following years, the discovery of the laser, an ideal light source for Raman spectroscopy, and the proposal by Elliot and Loudon⁷⁰ (1963) of Raman scattering as a useful method to investigate the low-lying electronic states of paramagnetic impurity ions in crystal, promoted considerably the electronic Raman spectroscopy.

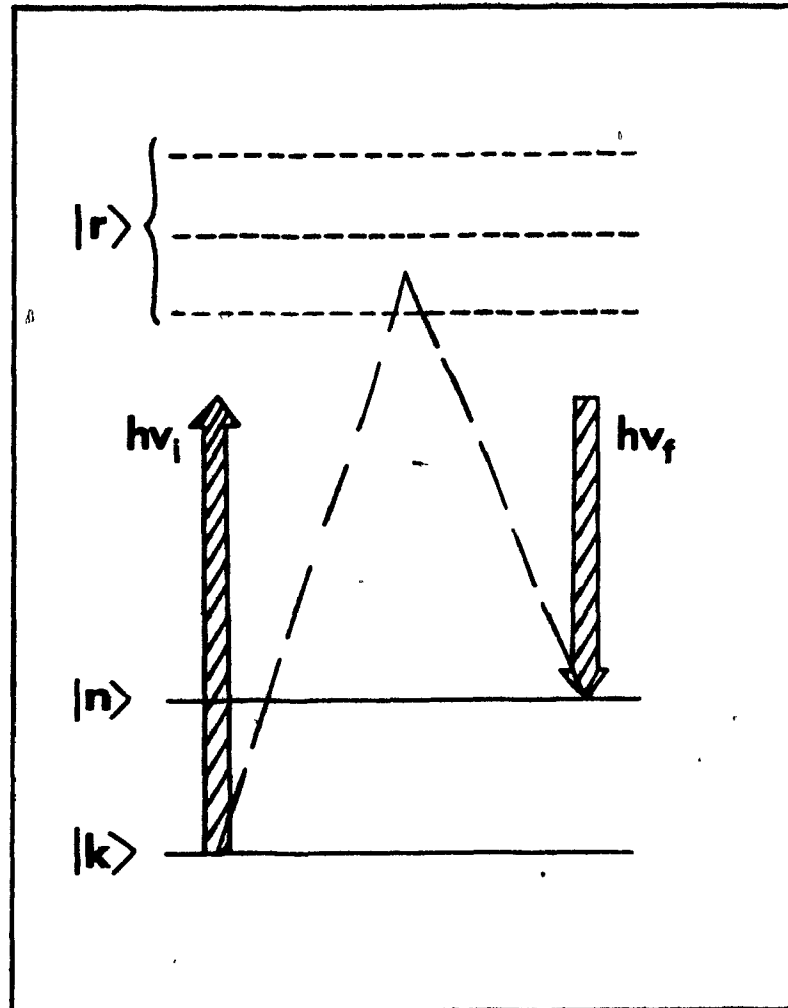


Fig. 4-5

The Raman transition K and N label the initial and final states, respectively; R labels the intermediate states. $h\nu_i$ and $h\nu_f$ represent the initial and final photon energies of the Raman scattering process.

The Born approach⁷¹ to the Raman effect makes use of the semi-classical radiation theory to calculate the electric moment (M) induced in the crystal by the electric field (E) of the incident light beam. In fact, the incident radiation polarizes the electronic cloud around the ions, and the scattered photon is produced by re-radiation of energy by the oscillating dipole moment of the polarized electronic cloud. In these terms, it is possible to define an electronic polarizability tensor $\alpha_{\rho\sigma}$ for a crystal according to the relation

$$M_{\rho} = \sum_{\sigma} \alpha_{\rho\sigma} E_{\sigma} \quad (4.3-1)$$

where M_{ρ} and E_{σ} are the components of the electric moment and electric field, respectively, taken along the principal axes of the crystal. We define also the Raman scattering efficiency S as the ratio of the number of scattered photons produced per unit time per unit cross-sectional area of the crystal solid angle about the direction of observation to the number of incident photons crossing a unit area in a unit time. For incident and scattered photons having a definite polarization in the directions of unit vectors e_i and e_s , respectively, the components of the polarizability tensor can be used to calculate the scattering efficiency

$$S = A \left[\sum_{\rho\sigma} e_i^{\rho} \alpha_{\rho\sigma} e_s^{\sigma} \right]^2 \quad (4.3-2)$$

where A is a constant of proportionality, e_i^{ρ} and e_s^{σ} are the

components of the unit vectors along the crystal principal axes ρ and σ . Equation (4.3-2) stresses the fact that the components of the polarizability tensor determine the intensity of the Raman scattered radiation, and as we will see, give information on the symmetry of the transition.

Analogous to the dipole operator that governs optical absorption, we can define a scattering operator $\hat{\alpha}_{\rho\sigma}$ which takes the scattering entity from state k to state n by a Raman process, Fig. 4.5. The average value of the scattering operator, between an initial state k and a final state n is given by

$$(\alpha_{\rho\sigma})_{kn} = \langle \Psi_n | \hat{\alpha}_{\rho\sigma} | \Psi_k \rangle \quad (4.3-3)$$

where the operator is defined⁷² to be

$$\hat{\alpha}_{\rho\sigma} = \frac{1}{h} \sum_r \frac{M_\rho | \Psi_r \rangle \langle \Psi_r | M_\sigma}{\nu_{rk} - \nu_0} + \frac{M_\rho | \Psi_r \rangle \langle \Psi_r | M_\sigma}{\nu_{rn} + \nu_0} \quad (4.3-4)$$

Ψ_r refers to the intermediate states, ν_0 is the frequency of the incident radiation, ν_{rk} is the transition frequency between the initial state k and the states r , and ν_{rn} is the transition frequency between the states r and the final state n .

M_σ is the transition moment of a component of the electric dipole operator along the axis of a Cartesian coordinate system and, therefore, transforms according to the coordinates X , Y or Z . We can form new moments M_μ and M_ν whose product makes the

scattering operator $\hat{\alpha}_{\mu\nu}$ to transform according to irreducible representation of octahedral symmetry. Loudon⁷³ calculated the different scattering tensors for different crystal symmetries; the corresponding matrices for O_h symmetry are given in Appendix E.

4.3.2 Selection rules and symmetry of the transitions

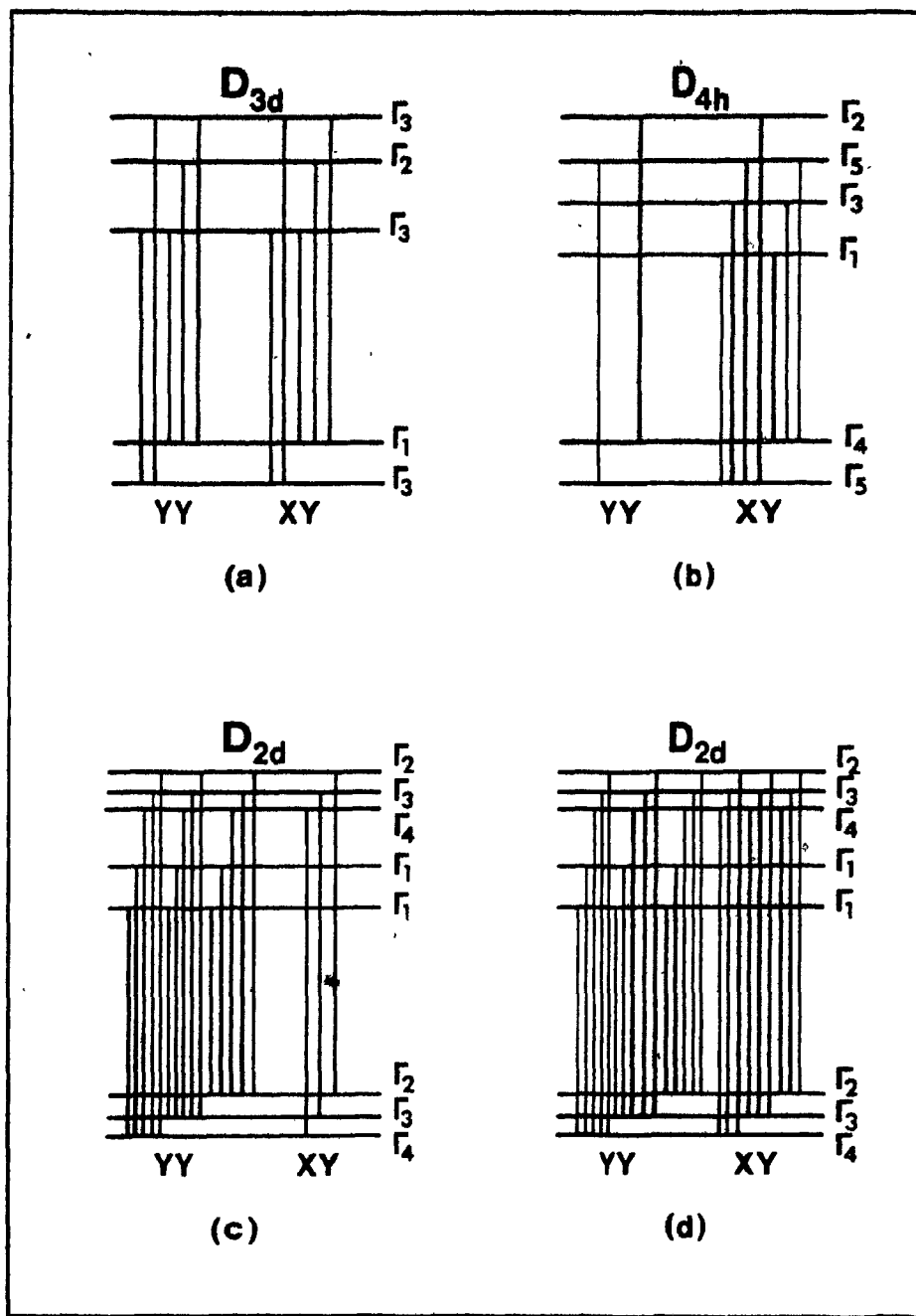
For the electronic Raman transition to become a physically observable quantity, the average value of the symmetry adapted scattering operator, Eq. (4.3-3), must be non-zero. Group theoretically, this means that the identity must appear³⁹ in reducing the representation product

$$\Gamma_n \times \Gamma_{\rho\sigma} \times \Gamma_k \quad (4.3-5)$$

For a given crystal orientation, the polarization of the incident and scattered photons determine the components of the scattering tensors involved in the Raman scattering process via Eq. (4.3-2). The selected components of the tensors give the irreducible representations to be used in the representation product, Eq. (4.3-5). Besides, the scattering operator $\hat{\alpha}_{\rho\sigma}$ is an even operator since M_ρ and M_σ both change sign simultaneously under inversion. Therefore, Eq. (4.3-3) is non-zero if the initial state and the final state are states of the same parity. This parity requirement implies that electronic Raman transitions are permissible among the $^5T_{2g}$ states of the ferrous ion.

Fig. 4-6

Allowed Raman transitions for different crystal deformations: (a) D_{3d} corresponds to a trigonal deformation, the sample being oriented as shown in Fig. 4-9; (b) D_{4h} corresponds to a tetragonal deformation, the sample being oriented as shown in Fig. 4-8; (c) and (d) D_{2h} corresponds to an orthorhombic deformation, the sample being oriented as shown in Fig. 4-10 and Fig. 4-11, respectively. The two polarizations YY and XY are also indicated.



MgO has octahedral symmetry and hence the scattering tensor has the irreducible representations A_{1g} , E_g and T_{2g} . Loudon⁷³ has calculated these Raman tensors for a crystal having its principal axes $[100]$, $[010]$ and $[001]$ aligned with the laboratory frame of reference X, Y and Z, respectively. For any other orientation of the crystal with respect to the laboratory frame of reference, the Raman tensors must be transformed^{74,75}, as instructed in Appendix E, before Eq. (4.3-2) can be used.

Fig. 4.6 shows the allowed transitions corresponding to the different crystal orientations and polarization of incident and scattered photons used in the experiments described in section 4.4. The notation $i(jk)l$ where $i, j, k, l \rightarrow X, Y, Z$ means that the incident photon has its \bar{k} -vector parallel to the i -axis and is polarized along the j -axis; the scattered photon has its \bar{k} -vector parallel to the l -axis and is polarized along the k -axis. It must be mentioned that the impurity induced local mode observed in the Raman spectrum of $MgO:Fe^{2+}$, Fig. 4.7, can be treated in a similar fashion to determine its symmetry properties.

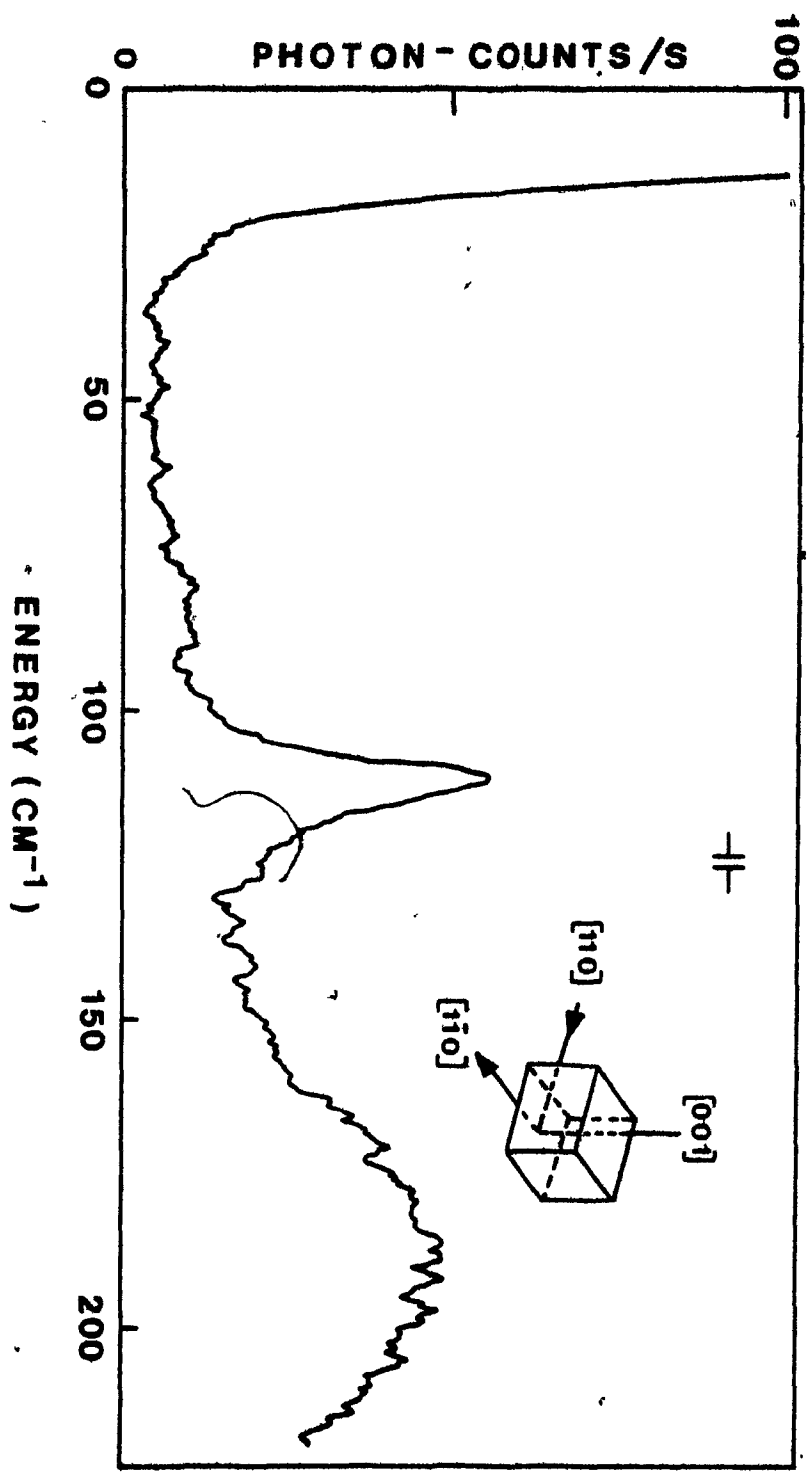
4.4 The Raman spectrum of iron doped MgO crystal

4.4.1 The electronic Raman transition

Figure 4.7 shows the Raman spectrum of an $MgO:Fe^{2+}$ sample immersed in liquid He, at a temperature below the lambda

Fig. 4-7

Electronic Raman spectrum of iron doped MgO taken at liquid He temperature (2K) using 200 mW of laser power (18834 cm^{-1} line). The spectrum is identical using the 20997 cm^{-1} laser line. The electronic Raman transitions to the Γ_{3g} and Γ_{4g} levels peak at 110.5 cm^{-1} . The A_{1g} vibrational mode is centered at 185 cm^{-1} . Incident light wavevector $\parallel [110]$ and scattered light wavevector $\parallel [1\bar{1}0]$, polarized parallel to $[1\bar{1}0]$ and $[001]$, respectively. The resolution is 2 cm^{-1} .



point (i.e., 1.6K). We observe a narrow emission peak at 110.5 cm^{-1} and an emission band which peaks at 185 cm^{-1} . No other features appear in the range 15 cm^{-1} to 220 cm^{-1} as opposed to Wong⁴² and Hjortsberg's⁴³ observations. This fact confirms, as Wong and Hjortsberg suggested, that the additional peaks observed in their spectra are due to other impurity systems.

Samples with different iron concentrations were examined by Raman spectroscopy. The electronic Raman peak observed at 110.5 cm^{-1} and the impurity mode at 185 cm^{-1} were found only in the dark yellow samples which have the highest iron impurity concentration among the samples we studied; as opposed to the pure and perfectly clear MgO sample which gives a flat Raman spectrum up to 500 cm^{-1} from the Rayleigh line. The signal strength is found to be proportional to the iron impurity concentration, although no quantitative relation can be established since the exact ferrous ion concentration in the doped MgO sample is not known and due to the 10% variation in the signal strength from experiment to experiment. This 10% fluctuation in the signal strength is mainly caused by the non-uniform impurity distribution in the crystal which can be judged from the color variation. Consequently, the 50μ diameter laser beam is never guaranteed to probe exactly the same volume in the crystal each time a sample is reinstalled in the Raman system leading to variation in the signal strength. No extensive reduction, oxidation or X-irradiation studies were attempted on these

samples since, particularly, the oxidation process destroys the surface quality of the MgO samples. Hence, the previous experimental conditions can never be recovered making any estimate of the relative change of the signal strength irrelevant. Moreover, Wong⁴² showed that only a small fraction of the ferrous ions are converted into ferric ions during the oxidation process.

At this point it would be legitimate to ask if the 110.5 cm^{-1} peak could be vibrational in nature.

In subsection 4.1.3, we have discussed the fact that the first-order vibrational Raman scattering was found to reproduce quite well the one-phonon density of states of the host MgO crystal. Fig. 4.1 shows that no lattice phonons are expected at energies below 200 cm^{-1} . Consequently, the 110.5 cm^{-1} peak could only be an impurity induced local mode of E_g or T_{2g} symmetry analogous to the A_{1g} mode at 185 cm^{-1} . But then, we would be dealing with a JT active vibration which would interact with the electronic levels, Γ_{3g} and Γ_{4g} , since they would have the same energy. This fact goes against Hjortsberg's observations of the behavior of the electronic levels in the presence of a magnetic field.

Billat et al.⁵⁹ have observed the first-order Raman spectrum of $\text{MgO}:\text{Fe}^{3+}$ which shows two overlapping peaks of A_{1g} symmetry at 129 cm^{-1} and 148 cm^{-1} . These features are not

observed in our spectra and cannot be confused with the 110.5 cm^{-1} peak. Thus, we eliminate the possibility that the observed peak is induced by the ferric ions.

Moreover, in Raman spectroscopy as well as in infrared absorption or in photoluminescence, we can make the qualitative observation that the narrowness of the 110.5 cm^{-1} line width (9 cm^{-1}) is typical of an electronic transition whereas the breadth of the 185 cm^{-1} band (50 cm^{-1}) is typical of a vibrational mode (for example, see Refs. 45 and 76). For all the reasons mentioned above, and from the results of the stress experiments (see chapter 5), it becomes evident that the 110.5 cm^{-1} peak is the electronic transitions observed by Wong⁴² and Hjortsberg⁴³, i.e., $\Gamma_{5g} \rightarrow \Gamma_{3g}$ and Γ_{4g} .

The existence of random strains in MgO crystals has been established from the asymmetrical line shape of EPR^{48,63} spectra. Acoustic paramagnetic resonance⁶⁵ (APR) studies of $\text{MgO}:\text{Fe}^{2+}$ as well as the study by microwave acoustic attenuation⁵³ (MAA) in the same material must include the presence of random strains in their corresponding theories to explain some of the experimental results. In $\text{MgO}:\text{Fe}^{2+}$, the average random strains distribution has been estimated from different considerations and different experimental techniques to be: 2×10^{-5} from EPR⁶³ and Mossbauer⁴⁷, 2×10^{-4} from EPR⁴⁸ and MAA⁵³, and 2×10^{-3} from APR⁶⁵. We see that the average random strains distribution seems to vary very much depending on the technique used to

investigate the sample, EPR being the least sensitive to the random strains. Besides, an average random strain distribution of 2×10^{-3} is sufficient to broaden the Γ_{5g} ground state of the ferrous ion to approximately 1 cm^{-1} , in accordance with the fact that optical transitions are easily broadened to a few wavenumbers (cm^{-1}) by large enough random strains⁶⁸. The coupling of the Γ_{3g} and Γ_{4g} levels to strain is predicted by theory to be five times stronger than that for the ground Γ_{5g} level, as mentioned by Ham³⁵. Accordingly, the first excited states Γ_{3g} and Γ_{4g} are broadened individually to 5 cm^{-1} where their separation of 3 cm^{-1} and the 2 cm^{-1} resolution of the spectrometer make up the observed line width of 10 cm^{-1} . This observation implies that optical transitions as well as APR transitions are very sensitive to random strains in crystals.

4.4.2 The electronic Raman transitions under uniaxial stress

The theory and concept of stress and strain are discussed in details in chapter 5 together with the interpretations of the experimental results presented in this subsection.

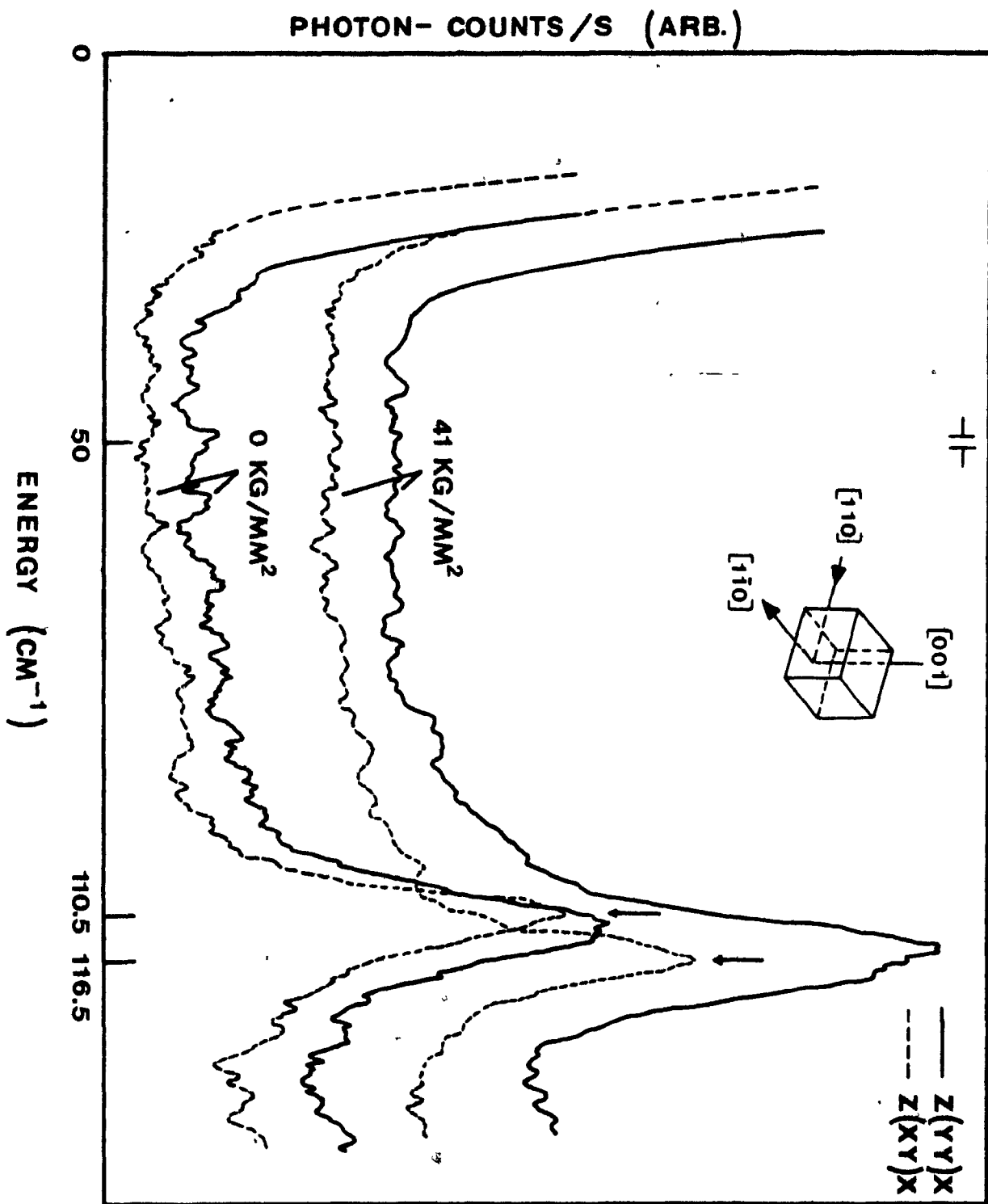
Three different types of uniaxial stress were applied to the MgO samples, each type being characterized by the symmetry axis along which the stress is applied. We chose two scattering geometries, i.e., $Z(\text{YY})X$ and $Z(\text{XY})X$ where the notation is explained in subsection 4.3.2. In certain cases, depending on the crystal orientation and the stress applied, different Raman transitions are allowed for each of the two scattering geometries chosen.

Using the Z(YY)X scattering geometry with the MgO samples prepared for tetragonal stress (applied along the [001]-axis of the crystal), only the $\Gamma_{5g} \rightarrow \Gamma_{4g}$ transition is allowed (in the $J = 2$ multiplet) and the peak position is observed at $112 \pm 0.5 \text{ cm}^{-1}$ from the Rayleigh line. Using the Z(XY)X geometry with the same crystal, both $\Gamma_{5g} \rightarrow \Gamma_{3g}$ and Γ_{4g} Raman transitions are allowed, and the peak position is observed at $110.5 \pm 0.5 \text{ cm}^{-1}$. Although any attempt to deconvolute the peaks in order to obtain accurately the position of the $\Gamma_{5g} \rightarrow \Gamma_{3g}$ transition is absolutely hopeless in our case, we still observe that the Γ_{4g} level is higher in energy than the Γ_{3g} level. Moreover, from the apparent displacement of the electronic peak in going from one scattering geometry to the other and assuming that both transitions, $\Gamma_{5g} \rightarrow \Gamma_{3g}$ and Γ_{4g} , have the same intensity, their separation can be estimated to be $3 \pm 2 \text{ cm}^{-1}$ in agreement with Meyer et al.⁴⁰ and Hjorsberg's⁴³ observation of 3.6 cm^{-1} . In the analysis of chapter 5, we choose a separation of 3 cm^{-1} between the Γ_{3g} and Γ_{4g} levels which fits best the data.

A tetragonal stress of 41 KG/MM^2 applied to a suitably prepared MgO crystal induced an appreciable shift of 4.5 cm^{-1} with the Z(YY)X geometry and 6.0 cm^{-1} with the Z(XY)X geometry, as shown in Fig. 4.8. Actually no shift as such is to be expected since only the A_{1g} component of the strain produces a shift of the center of gravity of a given electronic level (in Kaplyanskii's term⁷⁷), and this shift is the same for all

Fig. 4-8

Electronic Raman spectra of MgO:Fe^{2+} taken at liquid He temperature (4K) using 200 mW of laser power (18834 cm^{-1}) with and without a tetragonal stress applied. Incident light wavevector // $[110]$ and scattered light wavevector // $[1\bar{1}0]$. The corresponding polarizations and stress for each spectrum are indicated on the figure. The resolution is 2.5 cm^{-1} and the sensitivity is 100 photon-counts/s (full scale) with a 4.7s time constant. The arrows indicate the peaks at 110.5 cm^{-1} and 116.5 cm^{-1} .



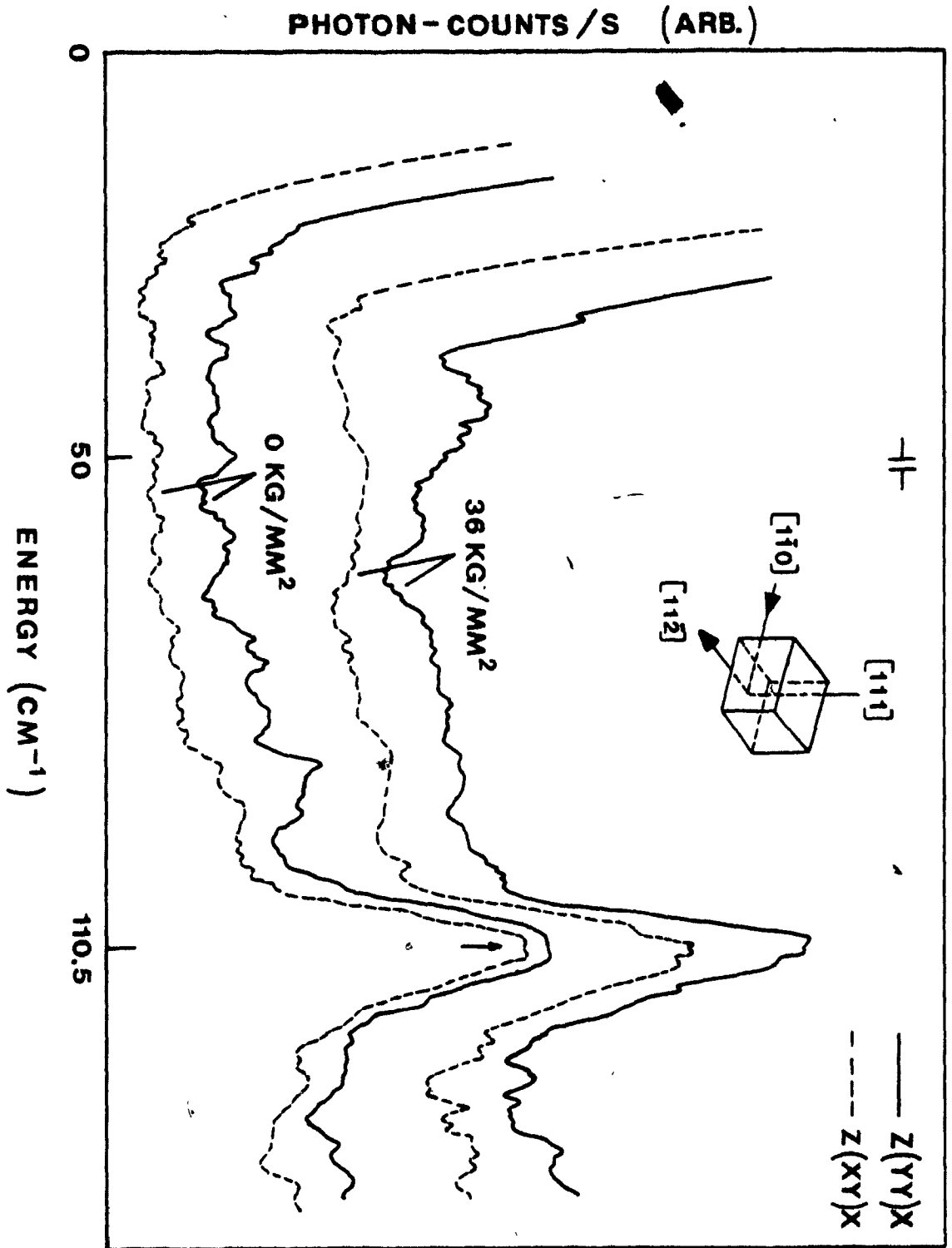
the levels of the ${}^5T_{2g}$ states since all the functions of Appendix B are eigenfunctions of the operator $L(L+1)$ with an eigenvalue of 2. Chapter 5 clears up this situation.

The trigonal stress applied along the $[111]$ -axis of a suitably prepared MgO crystal induces a small shift of 1.5 cm^{-1} of the electronic Raman peak using a stress of 36 KG/MM^2 . In this case represented by Fig. 4.9, both scattering geometries allow the transitions $\Gamma_{5g} \rightarrow \Gamma_{4g}$ and Γ_{3g} to be observed. Thus, the two transitions cannot be distinguished and the spectra corresponding to the two scattering geometries exactly superpose. A posteriori, we observe that the JT complex couples somewhat more strongly to the tetragonal stress than to the trigonal stress. In fact, the notion of coupling strength is clarified in chapter 5 where the strain coupling coefficients are determined and their relation to the JT coupling coefficients is established.

Finally, an orthorhombic stress applied along the $[110]$ -axis of a properly cut MgO sample was considered for two different crystals, as shown in Figs. 4.10 and 4.11. The $Z(XY)X$ geometry allows the transition $\Gamma_{5g} \rightarrow \Gamma_{4g}$ alone which is shifted by 2 cm^{-1} when a stress of 36 KG/MM^2 is applied to the sample. The $Z(YY)X$ geometry allows transitions to both Γ_{3g} and Γ_{4g} levels, and no shift of the electronic Raman peak is observed within the experimental error. Without stress, it is not possible to observe if the Γ_{4g} level is higher in energy

Fig. 4-9

Electronic Raman spectra of $\text{MgO}:\text{Fe}^{2+}$ taken at liquid He temperature (4K) using 200 mW of laser power (18834 cm^{-1}) with and without a trigonal stress applied. Incident light wavevector // $[1\bar{1}0]$ and scattered light wavevector // $[11\bar{2}]$. The corresponding polarizations and stress for each spectrum are indicated on the figure. The resolution is 2.5 cm^{-1} and the sensitivity is 100 photon-counts/s (full scale) with a 4.7s time constant. The arrow indicates the peak at 110.5 cm^{-1} .

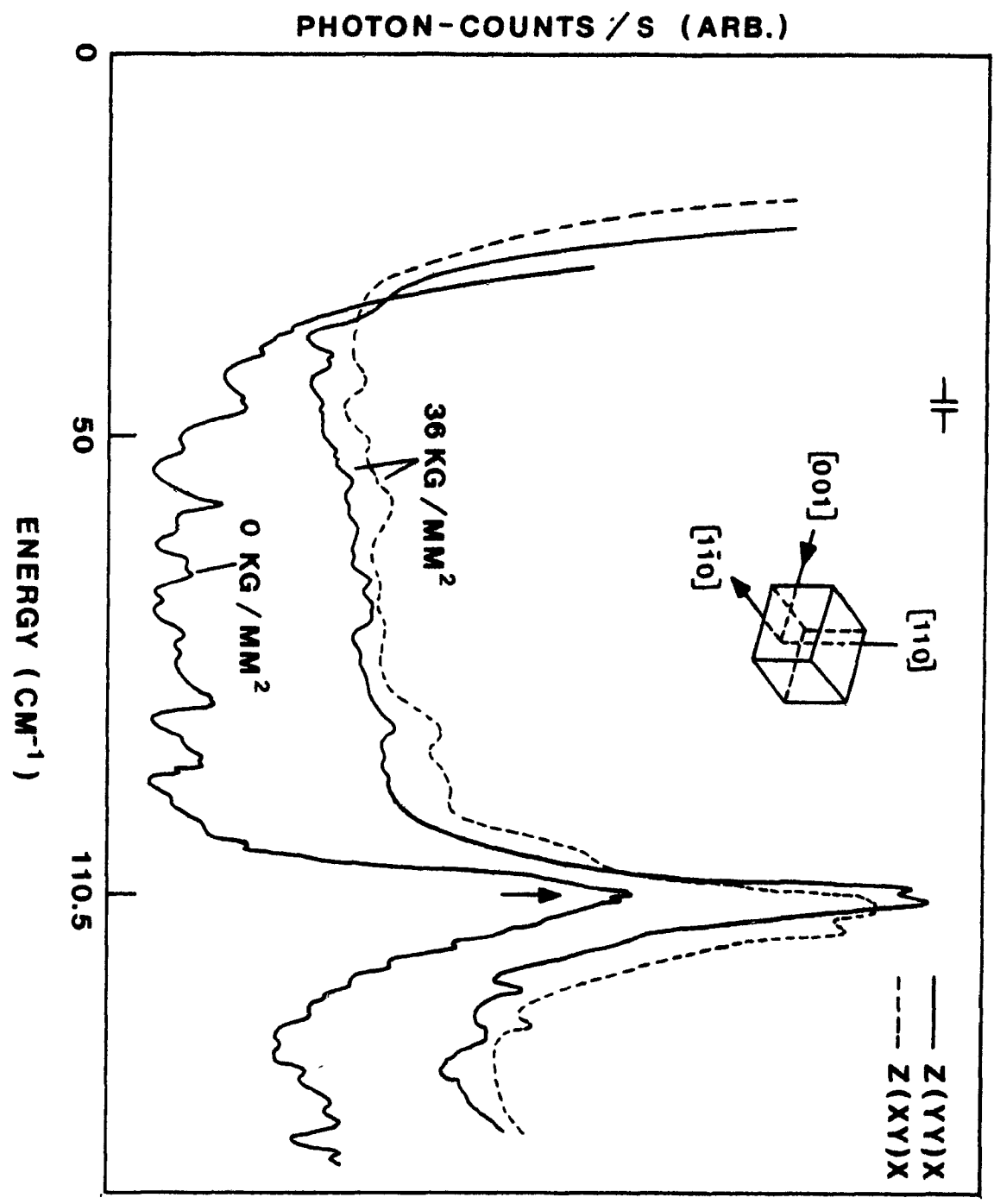


with respect to the Γ_{3g} level simply by changing the scattering geometries, as was done with the crystals prepared for the uniaxial tetragonal stress. This situation is mainly caused by the poorer surface quality of the samples which had to be cut and polished to obtain the required orientation and, accordingly, the signal quality has degraded. But still, under stress, we observe that the Γ_{4g} level is shifted on the high energy side, i.e., away from the Rayleigh line. Under uniaxial orthorhombic stress, it is shown in chapter 5 that the Γ_{3g} states and the Γ_{4g} states interact with each other. In such a case, as shown in Fig. 5.6, the levels tend to repel each other: the level which is higher in energy moves to the high energy side and vice-versa. Therefore, we conclude that the Γ_{4g} level is higher in energy, in agreement with our previous statement.

Each one of Fig. 4.8 to Fig. 4.11 compares two spectra, one taken without stress and the other taken with the highest applied stress during the corresponding experiment. In fact, several spectra were taken where the magnitude of the stress was varied between the two extreme values shown on each figure. These complete results are presented in Fig. 5.4 to Fig. 5.7 together with the theoretical curves obtained from the stress Hamiltonian introduced in chapter 5.

Fig. 4-10

Electronic Raman spectra of $\text{MgO}:\text{Fe}^{2+}$ taken at liquid He temperature (4K) using 200 mW of laser power (18834 cm^{-1}) with and without an orthorhombic stress applied. Incident light wavevector // $[001]$ and scattered light wavevector // $[1\bar{1}0]$. The corresponding polarizations and stress for each spectrum are indicated on the figure. The resolution is 2.5 cm^{-1} and the sensitivity is 100 photon-counts/s (full scale) with a 4.7s time constant. The arrow indicates the electronic Raman peak at 110.5 cm^{-1} .

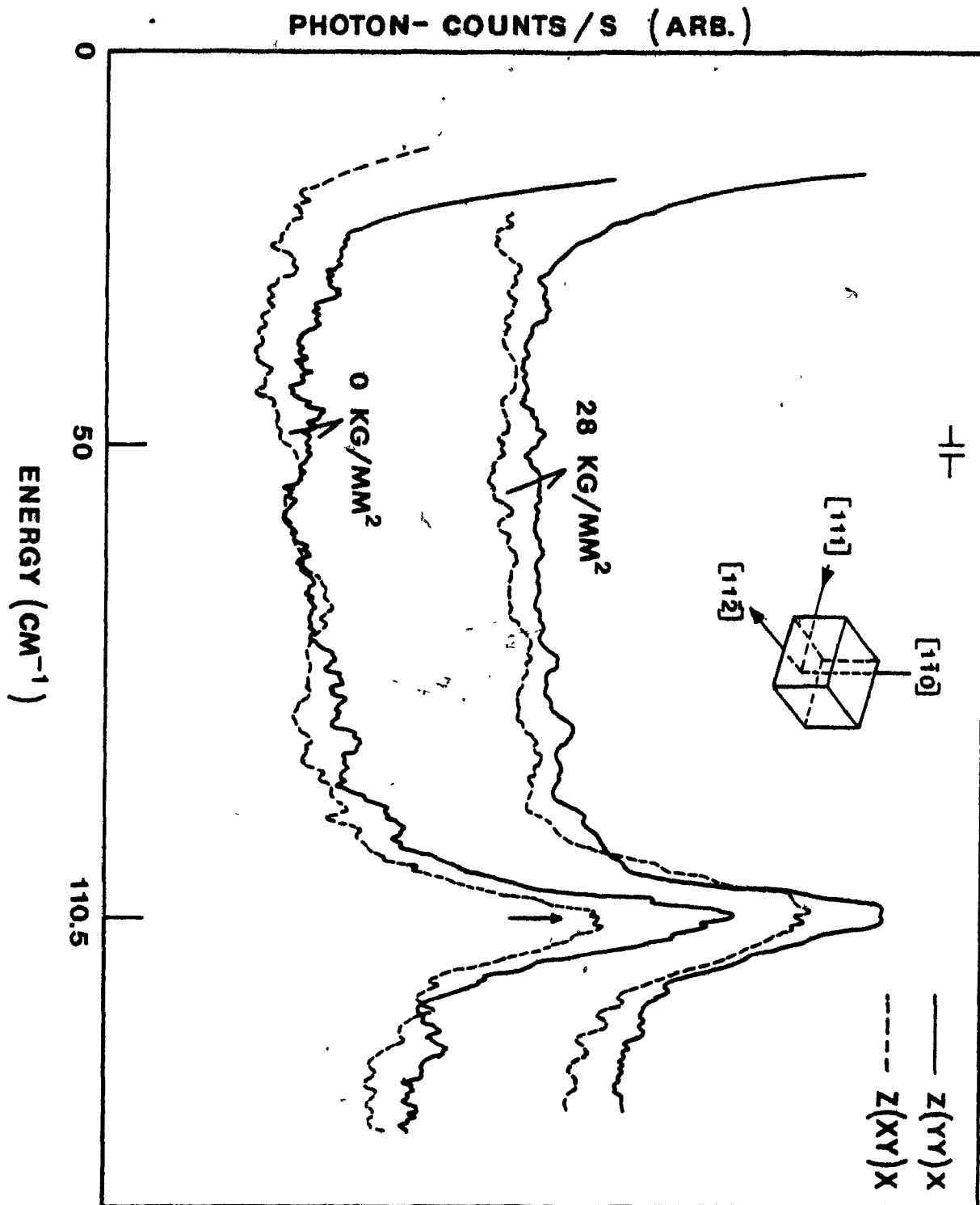


()

()

Fig. 4-11

Electronic Raman spectra of $\text{MgO}:\text{Fe}^{2+}$ taken at liquid He temperature (4K) using 200 mW of laser power (18834 cm^{-1}) with and without an orthorhombic stress applied. Incident light wavevector // $[111]$ and scattered light wavevector // $[11\bar{2}]$. The corresponding polarizations and stress for each spectrum are indicated on the figure. The resolution is 2.5 cm^{-1} and the sensitivity is 100 photon-counts/s (full scale) with a 4.7s time constant. The arrow indicates the peak at 110.5 cm^{-1} .



CHAPTER 5

THE UNIAXIAL STRESS

5.1 Ham's phenomenological approach

5.1.1 The strain components

We have showed in chapter 3 that the electronic energy levels are perturbed by any displacements either static or dynamic of the nearest neighbors. We can deliberately impose a static deformation of the octahedron surrounding the impurity ion by applying a uniaxial stress along one of the symmetry axes of the MgO crystal using the technique described in chapter 4. After deformation, the resulting site symmetry being lower than octahedral, some of the orbital degeneracies of the spin-orbit states must be lifted, i.e., the energy levels are split by the applied uniaxial stress. Schawlow et al.⁷⁸ were the first to attempt successfully such an experiment. They applied uniaxial stresses along different symmetry axes of MgO:Cr^{3+} samples and they observed both a shift and a splitting of a purely cubic field fluorescence line.

The ability to split an electronic energy level resides in the kind and magnitude of the distortion of the octahedron surrounding the impurity which, in turn, depends on the stiffness of the crystal lattice, i.e., its compliance to an externally applied stress. The deformation or strain of a

crystal lattice is usually described in terms of strain components⁷⁹ ϵ_{ij} whose magnitude depends on the physical properties of the material. Let's assume that \bar{x} , \bar{y} and \bar{z} are orthonormal vectors embedded securely in the unstrained crystal. After a small force per unit area or stress has been applied to the crystal, a uniform deformation of the lattice has taken place. The new distorted axes x' , y' and z' can be defined in terms of the old ones

$$\begin{bmatrix} x' \\ y' \\ z' \end{bmatrix} = \begin{bmatrix} 1 + \epsilon_{xx} & \epsilon_{xy} & \epsilon_{xz} \\ \epsilon_{yx} & 1 + \epsilon_{yy} & \epsilon_{yz} \\ \epsilon_{zx} & \epsilon_{zy} & 1 + \epsilon_{zz} \end{bmatrix} \begin{bmatrix} \bar{x} \\ \bar{y} \\ \bar{z} \end{bmatrix} \quad (5.1-1)$$

The dimensionless coefficients ϵ_{ij} define uniquely the magnitude and the symmetry of the deformation (strain). Assume that the distance between two atoms before the deformation is given by $\bar{r} = x\bar{x} + y\bar{y} + z\bar{z}$, and the same distance is given by $r' = x'x' + y'y' + z'z'$ after the deformation. The relative displacement of the two atoms due to the deformation of the lattice is given by

$$\begin{aligned} R &= r' - \bar{r} \\ &= x(x' - \bar{x}) + y(y' - \bar{y}) + z(z' - \bar{z}) \end{aligned}$$

which becomes after substitution of Eq. (5.1-1)

$$\mathbf{R} = (x\epsilon_{xx} + y\epsilon_{yx} + z\epsilon_{zx}) \bar{x} + (x\epsilon_{xy} + y\epsilon_{yy} + z\epsilon_{zy}) \bar{y} \\ + (x\epsilon_{xz} + y\epsilon_{yz} + z\epsilon_{zz}) \bar{z}$$

More generally, the displacement can be expressed as,

$$\mathbf{R}(\mathbf{r}) = u(\mathbf{r}) \bar{x} + v(\mathbf{r}) \bar{y} + w(\mathbf{r}) \bar{z} \quad (5.1-2)$$

where $u(\mathbf{r})$, $v(\mathbf{r})$ and $w(\mathbf{r})$ represent the small relative displacements of the two atoms measured along the orthonormal vectors of the previously unstrained crystal. Therefore, we will use Eq. (5.1-2) to measure the deformation with respect to the unstrained crystal taken as a reference frame. We can define the components ϵ_{ij} used in Eq. (5.1-1) as the rate of change of the components of the relative displacements, Eq. (5.1-2), along a particular direction \bar{x} , \bar{y} or \bar{z} of the unstrained crystal. The strain components e_{ij} are defined generally as a linear combination of ϵ_{ij} , i.e.,

$$e_{ij} = 1/2 (\epsilon_{ij} + \epsilon_{ji}) \quad : i, j = x, y, z$$

and

$$\epsilon_{ij} = \partial R_i / \partial r_j \quad (5.1-3)$$

with $R_x = u(\mathbf{r})$, $R_y = v(\mathbf{r})$, $R_z = w(\mathbf{r})$ and $r_x = x$, $r_y = y$, $r_z = z$.

We can also define a linear combination of strain coefficients designated by the irreducible representation of the symmetry of the deformation. These symmetry adapted strain coefficients are

$$e_A(A) = e_{xx} + e_{yy} + e_{zz} \quad (5.1-4a)$$

$$e_\theta(E) = e_{zz} - 1/2 (e_{xx} + e_{yy}) \quad (5.1-4b)$$

$$e_\epsilon(E) = \sqrt{3}/2 (e_{xx} - e_{yy}) \quad (5.1-4c)$$

$$e_z(T) = e_{yz} \quad (5.1-4d)$$

$$e_y(T) = e_{zx} \quad (5.1-4e)$$

$$e_x(T) = e_{xy} \quad (5.1-4f)$$

Let the force acting on the crystal element of surface ΔA_j (perpendicular to the j -axis) have components ΔF_i . We can define the stress tensor as

$$T_{ij} = \lim_{\Delta A_j \rightarrow 0} \Delta F_i / \Delta A_j$$

where $i, j = x, y, z$. The theory of elasticity assumes Hooke's law in postulating that the stress is proportional to strain (for sufficiently small strains). In this approximation, the elements of the stress tensor can be expressed as a linear

combination of strain components

$$T_i = \sum_{j=1}^6 c_{ij} e_j \quad (5.1-5)$$

where $i, j = 1(xx), 2(yy), 3(zz), 4(yz), 5(zx), 6(xy)$ and the proportionality constants c_{ij} are called the elasticity constants (or stiffness constants). The set of linear, homogeneous, independent equations represented by Eq. (5.1-5) can be solved for the e_j in terms of the elements of the stress tensor T_i and leads to the following linear combination

$$e_j = \sum_{i=1}^6 s_{ij} T_i \quad (5.1-6)$$

where the coefficients s_{ij} are called elastic compliance factors. Using the technique of ultrasonic continuous wave resonance⁸⁰ (sound velocity measurement), the elasticity constants c_{ij} can be determined experimentally as a function of temperature. The elasticity compliance factors s_{ij} are given in terms of the c_{ij} by the following relations⁸¹,

$$s_{11} = \frac{c_{11} + c_{12}}{(c_{11} - c_{12})(c_{11} + 2c_{12})} \quad (5.1-7a)$$

$$s_{12} = \frac{-c_{12}}{(c_{11} - c_{12})(c_{11} + 2c_{12})} \quad (5.1-7b)$$

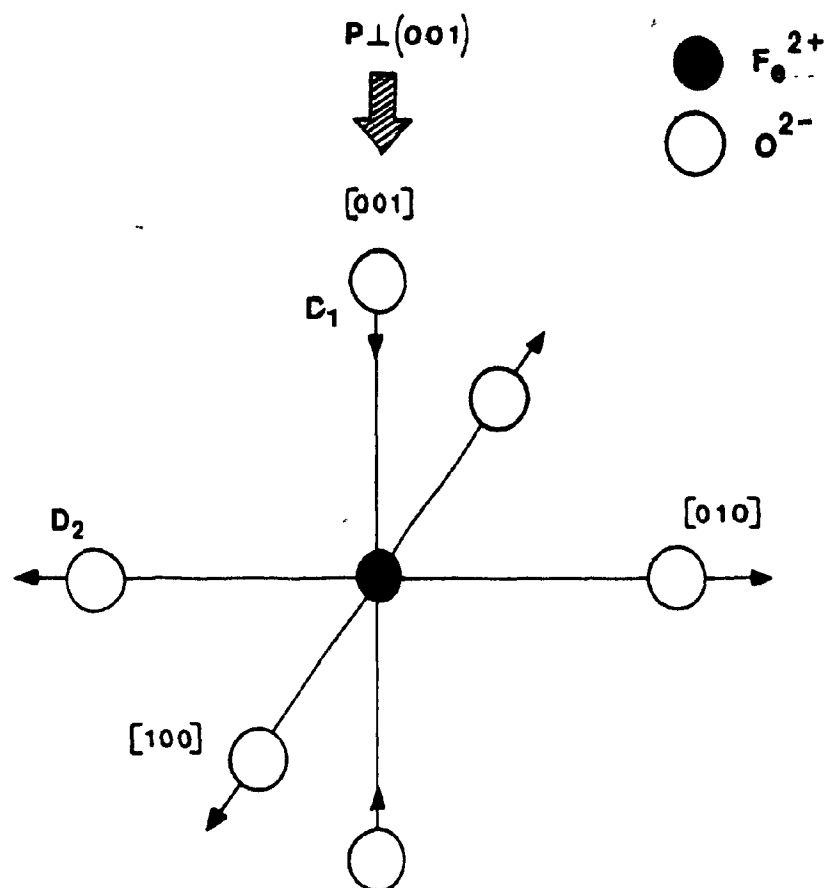


Fig. 5-1

Tetragonal deformation. Mechanical stress (P) applied perpendicularly to the (001)-plane displaces the upper and lower oxygen ions inward by D_1 ; the four other ions are displaced outward by D_2 .

$$s_{44} = \frac{1}{c_{44}} \quad (5.1-7c)$$

which are the only coefficients required to completely define the situation.

Depending on the type of deformation, we can relate the symmetry adapted strain components, Eq. (5.1-4), to the external pressure (element of the stress tensor) via the elastic compliance factors, Eq. (5.1-6). The pressure P is the uniaxial stress applied to the crystal and is chosen to be negative for compression. We distinguish three types of deformation, pictured in Figs. 5.1 to 5.3, for which Eqs. (5.1-6) are written explicitly.

Type (i), the tetragonal deformation (D_{4h} symmetry)

$$e_{\alpha}(A) = (s_{11} + 2s_{12}) P \quad (5.1-8a)$$

$$e_{\theta}(E) = (s_{11} - s_{12}) P \quad (5.1-8b)$$

$$e_{\epsilon}(E) = e_{\zeta}(T) = e_{\eta}(T) = e_{\xi}(T) = 0 \quad (5.1-8c)$$

Type (ii), the orthorhombic deformation (D_{2d} symmetry)

$$e_{\alpha}(A) = (s_{11} + 2s_{12}) P \quad (5.1-9a)$$

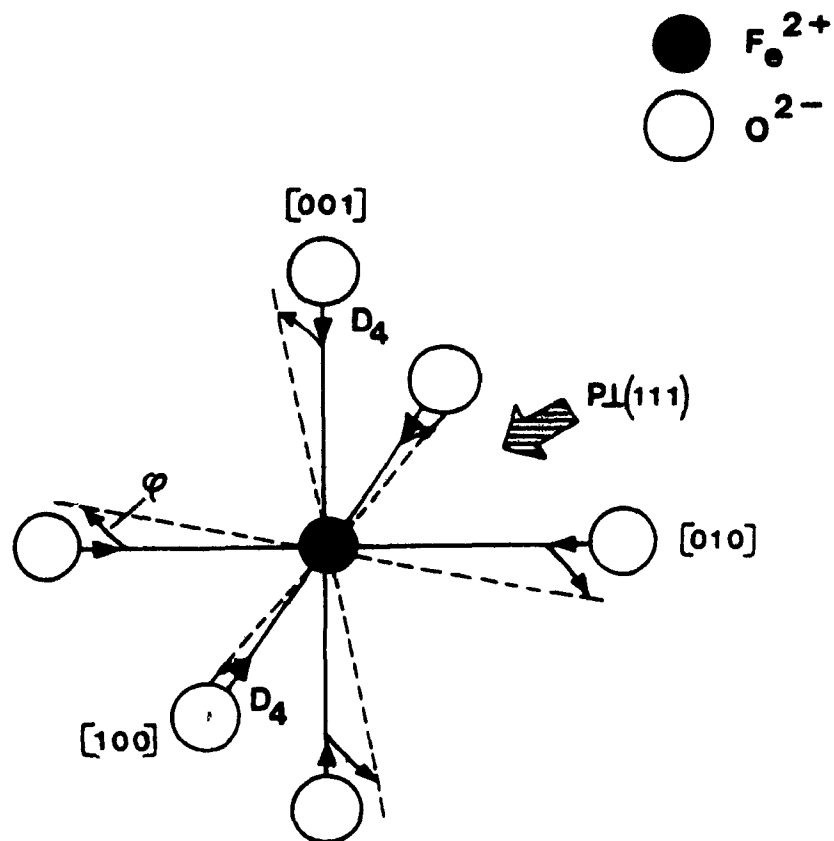


Fig. 5-2

Trigonal deformation. Mechanical stress (P) applied perpendicularly to the (111)-plane displaces all the oxygen ions inward by D_4 . The angle φ is in a plane defined by the $[111]$ -axis and any of the corresponding oxygen-ferrous ion axis.

$$e_{\theta}(E) = - (s_{11} - s_{12}) P/2 \quad (5.1-9b)$$

$$e_{\epsilon}(E) = e_{\zeta}(T) = e_{\eta}(T) = 0 \quad (5.1-9c)$$

$$e_{\zeta}(T) = s_{44} P/2 \quad (5.1-9d)$$

Type (iii), the trigonal deformation (D_{3d} symmetry)

$$e_{\alpha}(A) = (s_{11} + 2s_{12}) P \quad (5.1-10a)$$

$$e_{\theta}(E) = e_{\epsilon}(E) = 0 \quad (5.1-10b)$$

$$e_{\zeta}(T) = e_{\eta}(T) = e_{\gamma}(T) = s_{44} P/3 \quad (5.1-10c)$$

Marklund and Mahmouds⁸⁰ recently measured the elasticity constants c_{ij} of MgO crystal at 4.2K. Their experimental results ($\pm 0.1\%$) are

$$c_{11} = 30.67 \times 10^{10} \text{ N/M}^2$$

$$c_{12} = 9.371 \times 10^{10} \text{ N/M}^2$$

$$c_{44} = 15.76 \times 10^{10} \text{ N/M}^2$$

The corresponding elastic compliance factors s_{ij} are obtained from Eqs. 5.1-7.

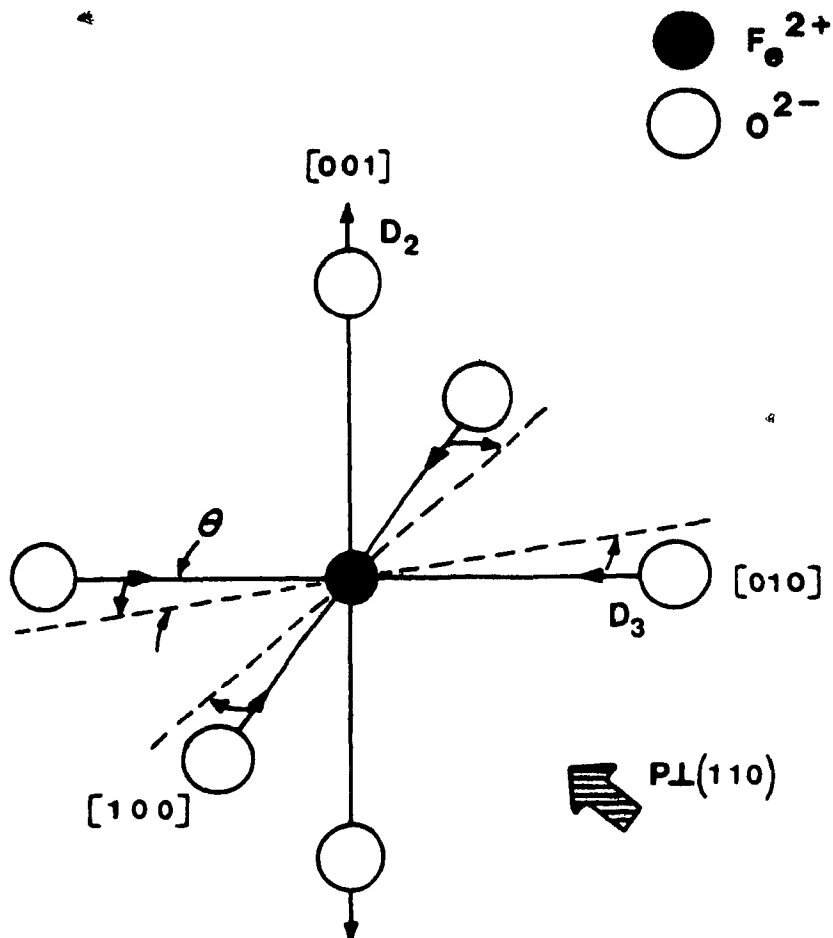


Fig. 5-3

Orthorhombic deformation. Mechanical stress (P) applied perpendicularly to the (110) -plane displaces the upper and lower oxygen ions outward by D_2 ; the four other ions are displaced inward by D_3 . The angle θ is in the (001) -plane.

5.1.2 The stress Hamiltonian

We have seen in chapter 3, that deformations of the lattice site are produced by the electron-phonon interaction between a JT impurity ion and the lattice vibrations transforming as the E_g or T_{2g} representation of the octahedral group. Since the strong JT effect leads to a static deformation of the cluster surrounding the ion, i.e., a permanently shifted equilibrium position of the distortion modes. Then, we may assume that the effect of strain in the crystal is that of shifting the equilibrium position of the distortion modes.

We can integrate Eq. (5.1-3b) to obtain an expression for the shift of the equilibrium position of a given distortion mode. Choosing the static tetragonal distortion, for example, the shift is expressed as

$$\begin{aligned}\Delta Q_\theta &= 1/\sqrt{3} \left[\Delta z_3 + \Delta z_6 - \frac{1}{2} (\Delta x_1 + \Delta x_4 + \Delta y_2 + \Delta y_5) \right] \\ &= 2R/\sqrt{3} \left[e_{zz} - \frac{1}{2} (e_{xx} - e_{yy}) \right]\end{aligned}$$

which can be written as

$$\Delta Q_\theta = \left[2R/\sqrt{3} \right] e_\theta = K e_\theta \quad (5.1-11)$$

where R is the lattice constant (2.1 Å) and e_θ is given by Eq. (5.1-4b). In doing this calculation, we have made the

() reasonably accurate assumption that the electronic states are coupled only to the nearest neighbors, based on the fact that the strain field is decreasing as R^{-2} away from the impurity ion. Consequently, we can write a new set of collective displacements Q'_n , Table 3.1, describing the vibrations of the octahedron about the displaced equilibrium positions

$$Q'_\theta = Q_\theta - K e_\theta \quad (5.1-12a)$$

$$Q'_\epsilon = Q_\epsilon - K e_\epsilon \quad (5.1-12b)$$

$$Q'_\xi = Q_\xi - K' e_\xi \quad (5.1-12c)$$

$$Q'_\eta = Q_\eta - K' e_\eta \quad (5.1-12d)$$

$$Q'_\zeta = Q_\zeta - K' e_\zeta \quad (5.1-12e)$$

where $K' = 2R$ can be obtained in a similar fashion to K . In the presence of strain, the elastic energy of the system measured from the displaced equilibrium positions is given by

$$\begin{aligned} H_{el}^s = & \frac{1}{2} \mu_E \omega_E^2 \left[(Q_\theta - K e_\theta)^2 + (Q_\epsilon - K e_\epsilon)^2 \right] \cdot I \\ & + \frac{1}{2} \mu_T \omega_T^2 \left[(Q_\xi - K' e_\xi)^2 + (Q_\eta - K' e_\eta)^2 + (Q_\zeta - K' e_\zeta)^2 \right] \cdot I \end{aligned} \quad (5.1-13)$$

Together with the kinetic energy and the JT energy in Eqs. (3.2-1) and (3.2-6), we constitute the Hamiltonian of the system. Accordingly, we can make the change of variables given

by Eq. (5.1-12), and the corresponding transformation of the canonical momenta $P_n' = P_n$. In terms of the primed variables, the elastic energy and the kinetic energy are expressed by the corresponding expressions in Eqs. (3.2-1) and (3.2-6), but the JT energy includes additional terms, i.e.,

$$H_{JT}' = H_{JT} + H^S$$

where

$$H^S = V_E K (e_e E_e + e_\epsilon E_\epsilon) + V_T K' (e_\xi T_\xi + e_\eta T_\eta + e_\zeta T_\zeta) \quad (5.1-14)$$

where H_{JT} is given by Eq. (3.1-11) and the electronic operators are defined by Eqs. (3.1-10). Therefore, we see that the effect of strain in the crystal is described phenomenologically by an Hamiltonian H^S identical in form to the JT Hamiltonian where the dynamical variables Q_n have been replaced by the static ones $e_n R$. The effects of static strains on the ${}^5T_{2g}$ states are described by the stress Hamiltonian $H^S({}^5T_{2g})$, given by Eq. (5.1-14). Now, we can use the Ham reduction factors, Eq. (3.3-3), to write the stress Hamiltonian as an operator in the space of the spin-orbit states,

$$H^S(J) = V_2 K_E(J) (e_e E_e + e_\epsilon E_\epsilon) + V_3 K_T(J) (e_\xi T_\xi + e_\eta T_\eta + e_\zeta T_\zeta) \quad (5.1-15)$$

where $V_2 = V_E K$ and $V_3 = V_T K'$ define the strain coupling coefficients and J specifies the set of spin-orbit states.

At this point, it is important to remember that we have made the assumption of a cluster model, i.e., the Q_n are normal modes of the cluster (the octahedron formed by the six nearest neighbors of the central ion) having unique frequencies ω_E and ω_T . We also made the crude approximation that the mode effective mass is given by the mass of one of the oxygen neighbor, $\mu_E = \mu_T = M(O^{2-})$, so that the canonical relations $P_n = \mu \dot{Q}_n$ can be written in Eqs. (3.2-1) and (3.2-6). So, we expect the relations between the strain coupling coefficients and the JT coupling coefficients to give agreement only within the accuracy of the above approximations. A careful determination of the JT coupling coefficients from the experimental results of stress experiments would have to bypass the question of an effective frequency and an effective mass (mode) in the calculations. A multi-mode full lattice model should be used in such a case.

5.1.3 The effect of uniaxial stress

The pressure P applied along a symmetry axis of the MgO crystal lowers the site symmetry around the ferrous ion. In such a case, group theory predicts that the orbital degeneracy of the spin-orbit states is partially lifted and a splitting of the energy levels occurs. The degeneracies and the transformation properties of the new states are obtained from the compati-

bility tables⁹ for the octahedral group. The group theoretical predictions with regard to the new states for the three types of strain, Eqs. (5.1-8) to (5.1-10), are summarized in Table 5.1. We see from the Table that the orthorhombic strain lifts all the degeneracies of the energy levels considered, whereas the tetragonal and the trigonal strains lift only partially the orbital degeneracies. Moreover, the trigonal strain is inoperative on the Γ_{3g} level showing clearly, in the context of the JT effect, that states transforming as E_g do not couple to vibrations (deformations) of T_{2g} representation since the product

$$E_g \times E_g = A_{1g} + A_{2g} + E_g$$

does not include T_{2g} . Group theory does not give which way the energy levels split and the magnitude of the splitting. To get this information, we rely on the stress Hamiltonian, Eq. (5.1-15).

In the case of MgO crystals, the strain splitting of the energy levels is expected to be of the same order of magnitude as the second-order spin-orbit splitting, Eq. (2.3-8). Therefore, the second-order spin-orbit Hamiltonian and the stress Hamiltonian must be treated simultaneously by first-order perturbation theory in the spin-orbit states. It must be noted that the JT Hamiltonian is accounted for by second-order perturbation theory and, consequently, can be treated independently from the spin-orbit Hamiltonian and the stress Hamiltonian. Besides, the

TYPE OF STRAIN	—————	TETRAGONAL	ORTHORHOMBIC	TRIGONAL
SYMMETRY	O_h	D_{4h}	D_{2d}	D_{3d}
$J = 3$	Γ_5	$\Gamma_4 + \Gamma_5$	$\Gamma_2 + \Gamma_3 + \Gamma_4$	$\Gamma_1 + \Gamma_3$
	Γ_4	$\Gamma_2 + \Gamma_5$	$\Gamma_2 + \Gamma_3 + \Gamma_4$	$\Gamma_2 + \Gamma_3$
	Γ_1	Γ_1	Γ_1	Γ_1
$J = 2$	Γ_4	$\Gamma_2 + \Gamma_5$	$\Gamma_2 + \Gamma_3 + \Gamma_4$	$\Gamma_2 + \Gamma_3$
	Γ_3	$\Gamma_1 + \Gamma_3$	$2\Gamma_1$	Γ_3
$J = 1$	Γ_5	$\Gamma_4 + \Gamma_5$	$\Gamma_2 + \Gamma_3 + \Gamma_4$	$\Gamma_1 + \Gamma_3$

TABLE 5.1

() JT effect on the strain splitting of the energy levels is accounted for via the Ham reduction factors which were calculated using the JT perturbed vibronic functions (see Appendix D).

The secular determinants of the spin-orbit and stress Hamiltonian can be solved easily if we neglect the matrix elements between states belonging to different J values, the magnitude of these terms being negligible compared with the energy separation between different J-states. These matrix elements are required to lift the accidental degeneracy occurring when states of different J values cross each other (which does not apply in our case). The resulting splitting of the energy levels is calculated from the stress Hamiltonian for the tetragonal, trigonal and orthorhombic strain as shown in Appendix F.

5.2 The interpretation of the experimental results

5.2.1 The procedure

() In the recent years, the first and the second excited states of the ferrous ion in MgO, Γ_{3g} and Γ_{4g} levels respectively, have been observed by optical infrared absorption to be at 106.9 cm^{-1} and 110.5 cm^{-1} . A confusion was created by Meyer et al.⁴⁰ with regard to the assignment of each peak. This confusion has been clarified by Hjortsberg et al.⁴³ whose conclusion is confirmed by us, i.e., the Γ_{3g} level is the lowest in energy with respect to the Γ_{4g} level as established in chapter 4. Also in chapter 4, we have concluded, however, that

the respective energy of the first excited states was slightly higher than Hjortsberg's observation at 109 cm^{-1} for the Γ_{3g} states and 112 cm^{-1} for the Γ_{4g} states. The crystal field theory predicts the energy of these two levels to be 198 cm^{-1} (Γ_{4g}) and 192 cm^{-1} (Γ_{3g}), Eqs. (2.3-11a) and (2.3-11b). We have seen in chapter 3 that the JT effect is expected to shift the energy levels and to reduce the spin-orbit splitting. Assuming that the shift of the energy levels is entirely due to the JT effect, we can use Eqs. (3.4-6) to calculate the JT energies $(E_{JT})_E$ and $(E_{JT})_T$ for different values of the quanta of vibration $\hbar\omega_E$ and $\hbar\omega_T$ from the expressions

$$(E_{JT})_E = \frac{83 [F_6(\omega_T) - F_2(\omega_T)] - 86 [F_4(\omega_T) - F_2(\omega_T)]}{F_{31} - F_{51}} \quad (5.2-1)$$

where

$$F_{31} = [F_3(\omega_E) - F_1(\omega_E)] [F_6(\omega_T) - F_2(\omega_T)]$$

$$F_{51} = [F_5(\omega_E) - F_1(\omega_E)] [F_4(\omega_T) - F_2(\omega_T)]$$

and

$$3/2 (E_{JT})_T = \frac{86 - (E_{JT})_E (F_5(\omega_E) - F_1(\omega_E))}{F_4(\omega_T) - F_1(\omega_T)} \quad (5.2-2)$$

where we have used a reduction of the spin-orbit splitting of -83 cm^{-1} between the Γ_{3g} and Γ_{5g} levels, and a reduction of -86 cm^{-1} between the Γ_{4g} and Γ_{5g} levels in accordance with our experimental results. Knowing the JT energies corresponding to a given set of quanta of vibration, we can calculate the JT corrections to the Ham reduction factors, Appendix D. The strain splitting of the energy levels considered, Eqs. (5.2-2), (5.2-4) and (5.2-6), is dependent on the magnitude of the strain components e_i which can be calculated from the knowledge of the pressure and the elasticity constants, and is dependent on terms like $K_E V_2$ and $K_T V_3$. The magnitude of these last two terms can be estimated from the experimental results and, knowing the Ham reduction factors K_E and K_T , we can extract the value of the strain coupling coefficients V_2 and V_3 . Moreover, the value of the strain coupling coefficients so obtained must be in agreement with the strain coupling coefficients estimated from the splitting of the EPR lines under uniaxial stress. Finally, for the self-consistency of the cluster model, as discussed in subsection 3.3.3, the same parameters used to extract the value of the strain coupling coefficients must be used to explain the orbital reduction in the experimental g-factor, $g = 3.428$.

However, since the effective mode quantum of vibration cannot be related in any unique way to the host lattice phonon spectrum^{61,62} and must be chosen in the range 300 cm^{-1} to 450 cm^{-1} , only a range of values for the JT energies can be determined which fit the reduction in the spin-orbit splitting and the

$\hbar\omega_E$	303	303	345	345	345	400	400
$\hbar\omega_T$	303	345	303	345	400	345	400
$(E_{JT})_E$	74	64	100	88	77	118	105
$\frac{3}{2}(E_{JT})_T$	108	134	94	120	148	103	130
V_2	6152	5722	8143	7639	7146	10256	9675
V_3	9103	11545	8493	10926	14068	10122	13185
$K_E(1)$.092	.088	.096	.092	.087	.096	.092
$K_E(2)$	-.129	-.130	-.142	-.141	-.141	-.153	-.139
$K_T(1)$.091	.092	.087	.089	.089	.085	.086
$K_T(2)$	-.127	-.137	-.126	-.135	-.144	-.134	-.142
K_L	-.447	-.441	-.442	-.437	-.430	-.431	-.425
K_S	1.494	1.494	1.494	1.494	1.494	1.494	1.494
K_A	2.872	2.862	2.864	2.855	2.845	2.847	2.837
K_B	1.172	1.166	1.176	1.170	1.164	1.174	1.168
k ($g=3.428$)	.90	.91	.91	.92	.94	.94	.95

• CM^{-1}

TABLE 5.2

g-factor, Table 5.2. Moreover, due to the large error in the strain coupling coefficients estimated from the EPR⁸², APR⁸³ and Mossbauer⁸⁴ experiments and due to the latitude in our fit to the experimental results we can only hope to determine a range of the most probable values for the strain coupling coefficients, and this within the scheme of the cluster model.

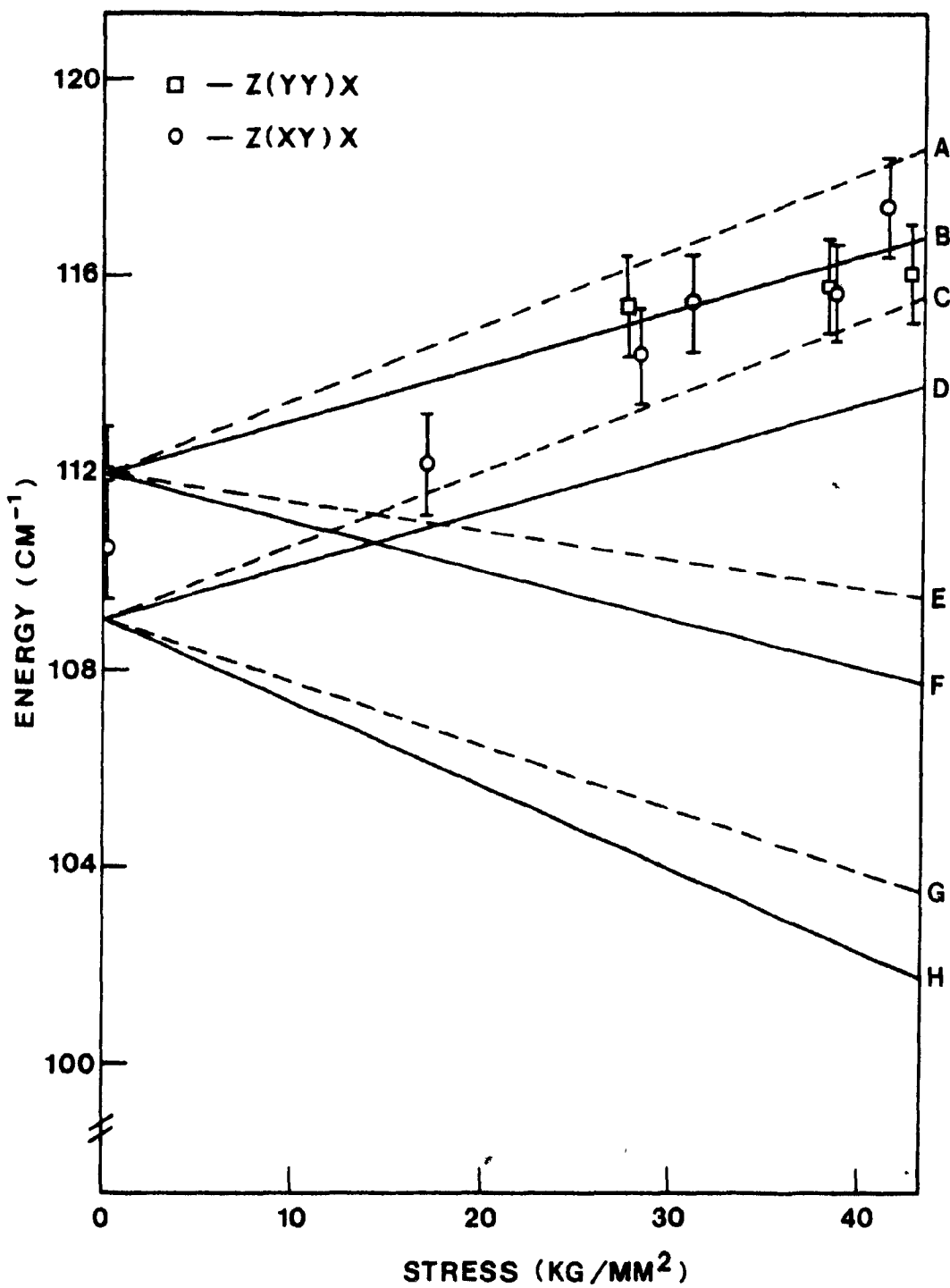
5.2.2 The fit to the experimental results

As mentioned in subsection 4.4.2, the position of the electronic Raman peak was measured for different values of stress, for each type of strain, using the two scattering geometries: Z(Y_Y)X and Z(XY)X. These results are presented in Figs. 5.4 to 5.7 together with the theoretical splitting of the corresponding energy levels as calculated from Eqs. (F-2), (F-4) and (F-6). For each case, the allowed Raman transitions are given in Fig. 4.6. Since the Γ_{5g} ground state is also split by any of the three types of strain, the theoretical curves represent all the possible transitions originating from the split components of the ground state. Besides, the ground state is only weakly coupled to strains in the crystal and split to a maximum of 1.6 cm^{-1} at 40 KG/MM^2 . Consequently, all the split components of the ground state are thermally populated at 10K (due to local laser heating) and lead to potentially observable transitions.

Fig. 5.4 represents the effect of increasing the tetragonal strain, in a MgO:Fe^{2+} sample, on the position of the

Fig. 5-4

Theoretical fit of the energy of the electronic Raman transitions measured for increasing tetragonal stress. The different electronic transitions are labeled from A to H. The theoretical fit is calculated as discussed in the text. The dash lines and the solid lines refer to transitions originating from the doublet and singlet components of the ground state, respectively.



() electronic Raman line. Group theoretically, the Z(YY)X scattering geometry allows transitions B and E to be observed, see Fig. 4.6. In this case, the energy corresponding to the difference between Eqs. (F-2e) and (F-2a) constitute the transition energy labeled B on the figure and fits the experimental results identified by open squares on the figure. Group theoretically, the Z(XY)X scattering geometry allows transitions to A, C, D, E, F and G, see Fig. 4.6. Since, under O_h symmetry, this scattering geometry allows transitions to both the Γ_{3g} and Γ_{4g} levels, we still expect transitions to some of the components of the two levels under D_{4h} symmetry. However, the shift of the peak position being even larger with this scattering geometry (6.0 cm^{-1} with respect to 4.5 cm^{-1} with the previous scattering geometry), only the allowed transitions A, C and D can possibly be observed to explain these experimental results. The corresponding energy of the transitions A, C and D are calculated from the difference between Eqs. (F-2e) and (F-2b), Eqs. (F-2c) and (F-2b), Eqs. (F-2c) and (F-2a), respectively.

Owing to the unique transition B to be fitted by the theoretical curve, with the Z(YY)X scattering geometry, we obtain a good estimate for the only parameter of the stress Hamiltonian in this case

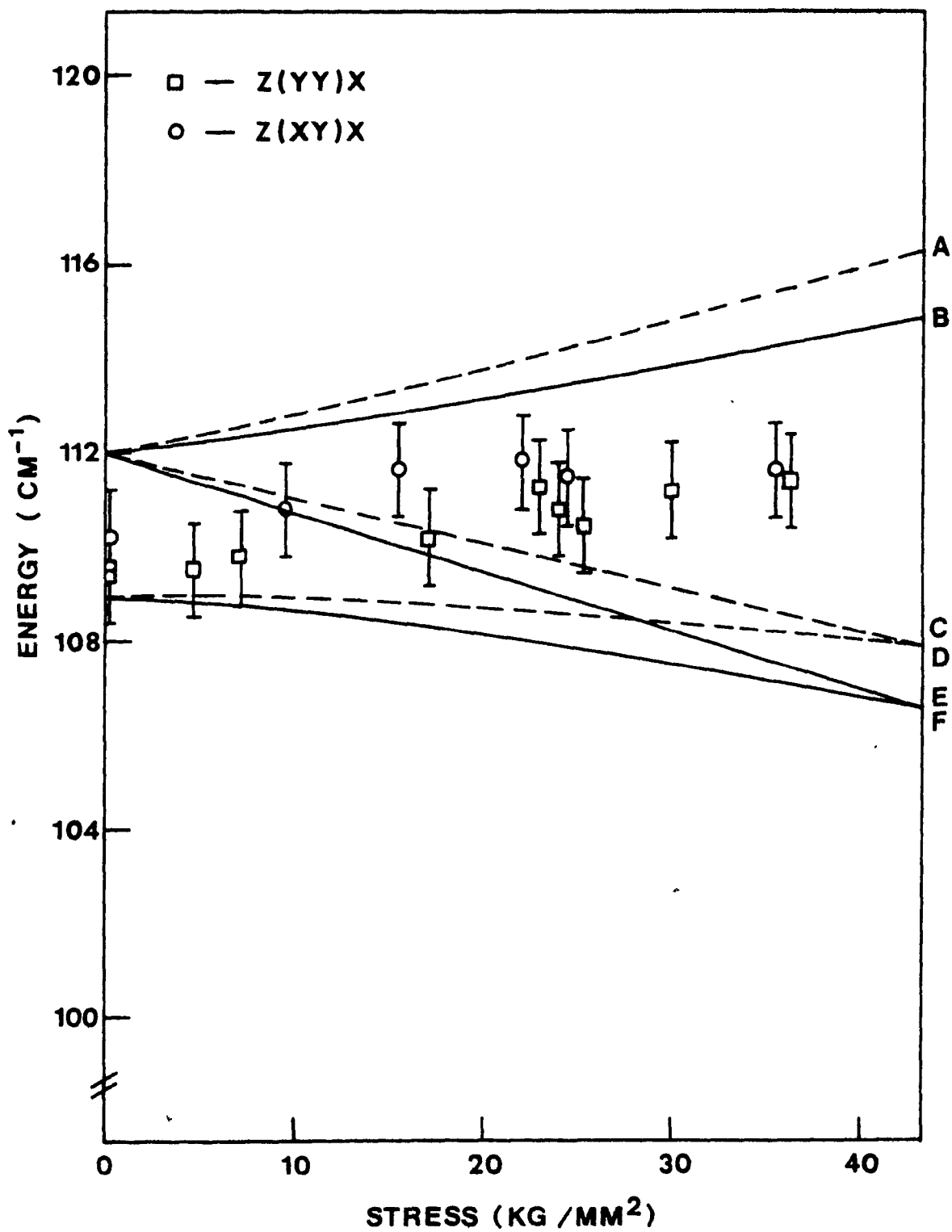
$$K_E(2)V_2 = -1000 \pm 150 \text{ cm}^{-1} \quad (5.2-3)$$

() Therefore, $K_E(2)$ only remains to be determined to obtain the value of the strain coupling coefficient to E_g -type of strain, V_2 .

The interpretation of the behaviour of the electronic Raman line in the case of trigonal strain, Fig. 5.5, is not as obvious as the case of tetragonal strain. The reason is that transitions, A, B, D, E and F are all group theoretically allowed with the Z(Y \bar{Y})X scattering geometry as well as with the Z(X \bar{Y})X geometry. When a uniaxial stress of 36 KG/MM² is applied to the sample, a small 1.5 cm⁻¹ shift of the peak is observed. Two explanations can be offered for such a behaviour of the electronic line, which will determine a range of values for the parameter $K_T(2)V_3$ in Eqs. (F-4). Since in absence of stress, the peak position is observed at $110.5 \pm .8$ cm⁻¹, it implies that both $\Gamma_{5g} \rightarrow \Gamma_{3g}$ and $\Gamma_{5g} \rightarrow \Gamma_{4g}$ transitions are observed. Consequently, we expect all the allowed transitions A, B, D, E and F to be observed, and the electronic Raman line follows the center of gravity of these transitions. This assertion, however, does not restrict the splitting of the Γ_{4g} level (O_h), i.e., the energy difference between A, B and C, E transitions is still left arbitrary. Nevertheless, we can postulate that a 2 cm⁻¹ resolution of the spectrometer and a random strain broadening of 5 cm⁻¹ should broaden the split components of the Γ_{4g} level (O_h) to at least 6 cm⁻¹, so that we should distinguish a splitting of the electronic Raman line, using Rayleigh's criterion, at an energy difference between

Fig. 5-5

Theoretical fit of the energy of the electronic Raman transitions measured for increasing trigonal stress. The different electronic transitions are labeled from A to F. The theoretical fit is calculated as discussed in the text. The **dash** lines and solid lines refer to transitions originating from the doublet and singlet components of the ground state, respectively.



Eqs. (F-4b) and (F-4a) equals to 6 cm^{-1} . This situation is depicted in Fig. 5.5 and leads to an upper limit for the value of the strain coupling coefficient

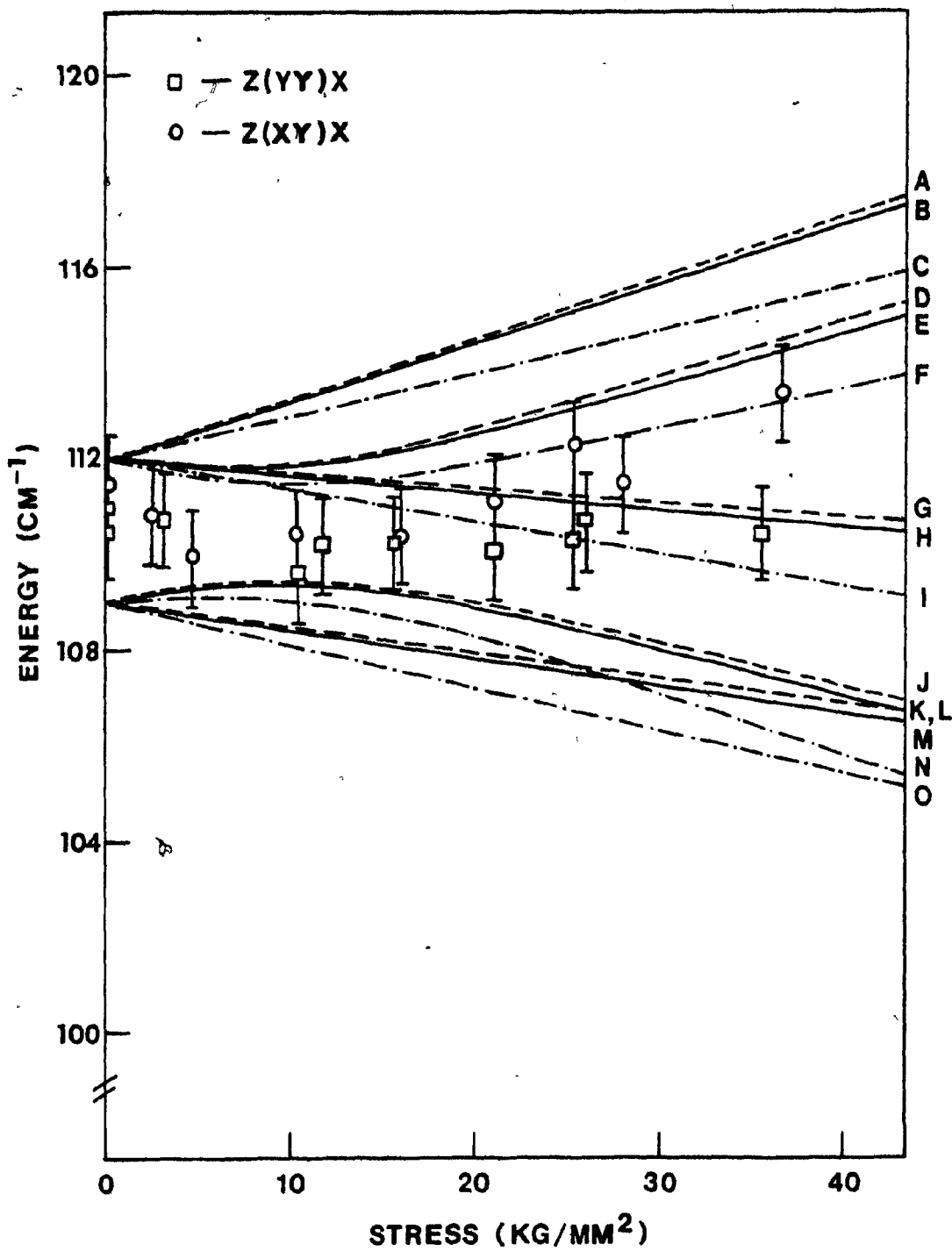
$$K_T(2)V_3(\text{MAX}) = -840 \text{ cm}^{-1} \quad (5.2-4)$$

The lower limit for the value of the strain coupling coefficient can be set to zero and, still, the 1.5 cm^{-1} shift of the Raman line for large trigonal strain can be understood if a reduction in the transition probability to the $\Gamma_{3g} (D_{4h})$ level takes place for increasing stress. In such a case, for sufficiently high stress, we would mainly observe the $\Gamma_{5g} \rightarrow \Gamma_{4g} (O_h)$ transition at 112 cm^{-1} . However, since the intermediate states of the ferrous ion at energies larger than $10,000 \text{ cm}^{-1}$ needed to compute Eq. (4.3-2) are not known, it is not possible to obtain a sufficiently accurate value for the Raman intensities (or transition probabilities) relevant to this problem that would help us to decide between the upper limit value given by Eq. (5.2-4) or the lower limit, $V_3 = 0$.

The orthorhombic strain, which combines both a tetragonal strain (expansion) and a component of trigonal strain (compression), provides evidence for the upper limit value given by Eq. (5.2-4). With the Z(Y)X scattering geometry, all the transitions shown on Fig. 5.6 are allowed and the corresponding peak position ($110.5 \pm .8 \text{ cm}^{-1}$) is not affected by the applied stress within the experimental errors. Again, we observe the

Fig. 5-6

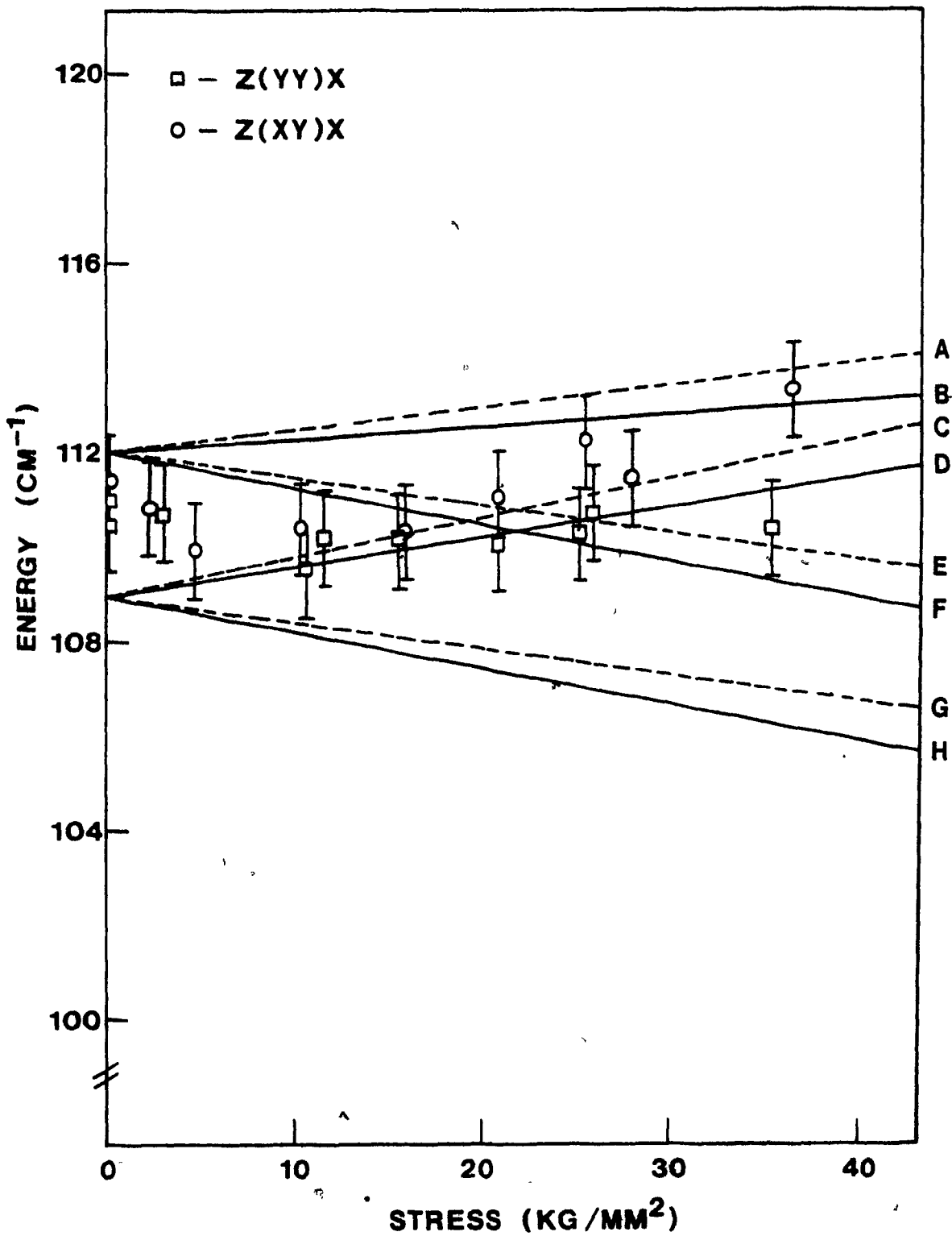
Theoretical fit of the energy of the electronic Raman transitions measured for increasing orthorhombic stress. The different electronic transitions are labeled from A to O. The theoretical fit is calculated as discussed in the text. The dash lines, solid lines and dash-dot lines refer to transitions originating from the three different singlet components of the ground state.



center of gravity of all the allowed transitions of Fig. 5.6 and not much can be extracted as to the behaviour of the individual energy levels under stress. The Z(XY)Y scattering geometry is more restrictive and allows transitions A to I, inclusively, all issued from the $\Gamma_{4g}(O_h)$ level. To be consistent with our interpretation of Fig. 5.4, where, as far as the $\Gamma_{4g}(O_h)$ level is concerned, transitions are mainly to the singlet state $\Gamma_{2g}(D_{4h})$, i.e., transitions A and B, we expect the tetragonal strain component of the orthorhombic strain to induce transitions to the corresponding singlet state now represented by transitions D, E, F on Fig. 5.6. The theoretical curves of Fig. 5.6 have been calculated using the experimental results given by Eqs. (5.2-3) and (5.2-4). These curves show that, indeed, the center of gravity of all the transitions is preserved and that the singlet state (transitions D, E, F) reproduces very well the experimental results represented by open circles on Fig. 5.6, as expected from Fig. 5.4. Again, no measurable broadening of the electronic Raman peak is observed which could be due to weak transitions probabilities for A, B, C and M, N, O transitions of Fig. 5.6. The theoretical curves based on the equations which lead to Fig. 5.6 were calculated for the case $V_3 = 0$, and are presented in Fig. 5.7. The experimental results represented by open circles belong to the Z(XY)X scattering geometry which allows transitions A, B, C and D originating from the $\Gamma_{4g}(O_h)$ level in absence of stress. These experimental results cannot be unambiguously attributed to the center of gravity of the four allowed transitions or even to

Fig. 5-7

Theoretical fit of the energy of the electronic Raman transitions measured for increasing orthorhombic stress. The different electronic transitions are labeled from A to H. The theoretical fit is calculated assuming $V_3 = 0$, as explained in the text. The dash lines and solid lines refer to transitions originating from the doublet and singlet components of the ground state, respectively.



any of the group of transitions A, B or C, D. Therefore, we conclude that Fig. 5.6 provides the best fit to the experimental results obtained for the case of orthorhombic strain and corroborates the evidences obtained from the experimental results presented in Fig. 5.4. Since the value of the parameter $K_T(2)V_3$ given by Eq. (5.2-4) provides the best fit to the experimental results shown on Figs. 5.5 and 5.6, this value will be used to verify the consistency of the cluster model keeping in mind that a large error is attributed to it. At this point, $K_E(2)$ and $K_T(2)$ must be determined to extract the range of values for V_2 and V_3 .

Table 5.2 gives a range of values for $K_E(2)$ and $K_T(2)$ which were obtained from vibrational quanta and JT energies suitably chosen to fit both the reduction in the spin-orbit splitting and the reduction in the g-factor. These values for the Ham reduction factors are

$$K_E(2) = -0.140 \pm .014 \quad (5.2-5)$$

$$K_T(2) = -0.135 \pm .010 \quad (5.2-6)$$

which lead directly to an estimate for the strain coupling coefficients via Eqs. (5.2-3) and (5.2-4), i.e.,

$$V_2 = 7140 \pm 1800 \text{ cm}^{-1} \quad (5.2-7)$$

$$V_3^*(\text{MAX}) = 6220 \pm 460 \text{ cm}^{-1} \quad (5.2-8)$$

The coupling coefficient to E_g -type of strain, Eq. (5.2-7) is affected by the compounded errors of Eqs. (5.2-5) and (5.2-3), whereas Eq. (5.2-8) represents the maximum value of the coupling coefficient to T_{2g} -type of strain which only affected by the error in Eq. (5.2-6). It must be remembered that V_3 can actually take any value between 0 cm^{-1} and $V_3(\text{MAX})$, but that $V_3(\text{MAX})$ best fits the experimental results presented in Fig. 5.6 and is retained as the representative value of the V_3 coupling coefficient.

The strain coupling coefficients for the Γ_{5g} ground state of the ferrous ion in MgO have been measured by three different techniques, i.e., from the splitting of the EPR⁸² and APR⁸³ lines under applied stress and from Mossbauer spectroscopy⁸⁴. Using the notation of Watkins and Feher⁸², the strain splitting of the Γ_{5g} ground state is described by the Hamiltonian

$$H^B(\Gamma_{5g}) = J \cdot \delta D \cdot J$$

where J is an effective angular momentum (see Eq. (3.3-6)) and the tensor δD is related to the strain components via the following expression

$$\delta D_i = \sum_j G_{ij} e_j \quad (5.2-9)$$

In this case, Voigt notation is assumed, i.e., $\delta D_1 = \delta D_{xx}$, $\delta D_4 = \delta D_{yz}$, etc., but $e_1 = e_{xx}$, $e_4 = 2e_{yz}$, etc. Assuming

with Watkins and Feher that the trace of the tensor δD vanishes, i.e., $G_{11} = -2G_{12}$, and comparing Eq. (5.2-9) with Eq. (5.1-15), we obtain the equivalences

$$V_2 K_E(1) = G_{11} \quad (5.2-10)$$

$$V_3 K_T(1) = 2G_{44} \quad (5.2-11)$$

Table 5.3 gives the different experimental values for G_{11} and G_{44} . Although not quoted, the errors on these experimental values are known to be large as can be judged from the marked discrepancy in the values. Again, from Table 5.2, we can determine a range of values for the Ham reduction factors (with $J = 1$) in accordance with the reduction in the spin-orbit splitting and the g -factor,

$$K_E(1) = .092 \pm .008 \quad (5.2-12)$$

$$K_T(1) = .088 \pm .005 \quad (5.2-13)$$

Using these values, V_2 and V_3 of Table 5.3 were estimated. Besides, if absolute values of G_{11} and G_{44} are difficult to estimate, their relative value can be obtained more accurately. From APR⁶⁵ and acoustic saturation measurements⁶⁴, a reasonably accurate ratio is found for $MgO:Fe^{2+}$ samples,

$$G_{11}/G_{44} = 1.59 \pm .09 \quad (5.2-14)$$

\bullet CM ⁻¹	EPR ⁸²	APR ⁸³	MOSSBAUER ⁸⁴
G_{11} \bullet	800	647	585 \circ
$2G_{44}$ \bullet	1080	814	(736)
G_{11}/G_{44} \bullet	1.48	1.59	—
V_2 \bullet	8700	7000	6400
V_3 \bullet	12300	9200	(8400)

TABLE 5.3

This result is used to obtain the value for $2G_{44}$ in parentheses in Table 5.3. Our result for V_2 , Eq. (5.2-7), compares favorably with the three corresponding values of Table 5.3, whereas our estimate of V_3 seems anomalously low.

In following the phenomenological approach, the change of variables, Eqs. (5.1-12), provided a relation between the phenomenological strain coupling coefficients, V_2 and V_3 , and the JT coupling coefficients, V_E and V_T . This relation is given by Eq. (5.1-15), i.e., $V_2 = KV_E$ with $K = 2R/(3)^{\frac{1}{2}}$ and $V_3 = K'V_T$ with $K' = 2R$. As we already mentioned, the justification of the relations between the strain and JT coupling coefficients are subjected to the approximations inherent to the cluster model. If we were to account for the displacements of more distant atoms than the nearest neighbors, or if the elastic constants in the neighborhood of the ferrous ion should be different from those of the bulk MgO crystal, the constants of proportionality K and K' could have expressions much different from those of Eq. (5.1-15). Using expressions (3.2-3) and (3.2-7) for V_E and V_T , respectively, and Eq. (5.1-15), we can relate the strain coupling coefficients to the JT energy and vibrational quantum of the appropriate mode in the following way

$$V_2 = 2.360 \hbar \omega_E (E_{JT})_E^{\frac{1}{2}} \text{ cm}^{-1} \quad (5.2-15)$$

$$V_3 = 2.891 \hbar \omega_T (3E_{JT}/2)_T^{\frac{1}{2}} \text{ cm}^{-1} \quad (5.2-16)$$

() Again, using the results of Table 5.2 pertinent to the reduction in the spin-orbit splitting and the g-factor, we obtain

$$V_2 = 7900 \pm 2500 \text{ cm}^{-1}$$

$$V_3 = 11100 \pm 3300 \text{ cm}^{-1}$$

The phenomenological relation between V_2 and V_E gives the right estimate for V_2 to a better extent than we would have expected since it corroborates all the experimental results of Table 5.3. The estimate for V_3 also corroborates the results of Table 5.3 but overestimates our result given by Eq. (5.2-8).

Now that it is well established that the trigonal strain resulting from a non-zero component of stress along the $[111]$ -axis of a MgO crystal is somewhat smaller than expected; a simple explanation of the phenomenon can be presented.

Lange⁶⁵ determined the paramagnetic behaviour of Fe^{2+} in MgO using acoustic resonance techniques. The coupling of the hypersonic acoustic wave (10^9 Hz) to the paramagnetic state is observed to be related to the local vibrational components which interact with the electronic states. Lange deduced that the Γ_{5g} ground state of the ferrous ion is split into a singlet A_{1g} state and a doublet E_g state due to an internal strain field of E_g symmetry.

()

King et al.⁵³ measured the microwave acoustic attenuation of hypersonic waves in samples of single-crystal iron doped MgO. A comparison of the magnitude of the attenuation of the (E_g) compressional mode with theory together with the absence of a peak in the (T_{2g}) shear mode attenuation are in fair agreement with a model which supposes that the Fe^{2+} ions are subjected to random static strains which are predominantly compressional (E_g) in nature.

Consequently, Lange⁶⁵ and King et al.⁵³ established the presence of strong static strains of E_g symmetry in iron doped MgO. Assuming that such random strains exist in our sample, as can be judged from the width of the Raman line, we can account for the apparently reduced trigonal strain coupling of the ferrous ion.

In chapter 5, we have substantiated the analogy between the JT effect and the static strains, expressed the stress Hamiltonian in terms of electronic operators of E_g and T_{2g} symmetry. In subsection 3.2.2, we have treated the JT problem of an electronic triplet state coupled to a doublet vibrational mode. In that context, Ham²⁶ showed that the (E_g) strain electronic operator is diagonal in the spin-orbit states and its matrix elements within the vibronic states are written

$$\langle \Psi_i, MN | O(E_g) | \Psi_j, M'N' \rangle = \langle \Psi_i | O(E_g) | \Psi_j \rangle \cdot \delta_{ij} \delta_{MM'} \delta_{NN'} \quad (5.2-17)$$

On the other hand, the (T_{2g}) strain electronic operator is of the off-diagonal type and its effect in the vibronic states is reduced, according to the reduced overlap of the vibrational functions (see subsection 3.2.2). Its matrix elements within the vibronic states are written

$$\langle \Psi_i | MN | O(T_{2g}) | \Psi_j | M'N' \rangle = \langle \Psi_i | O(T_{2g}) | \Psi_j \rangle \langle M | M' \rangle \langle N | N' \rangle \quad (5.2-18)$$

Ham concludes from Eqs. (5.2-17) and (5.2-18), that the stress Hamiltonian is expressed in terms of V_2 and V_3 , as in Eq. (5.1-15), but that V_3 alone is multiplied by an exponential term (orbital reduction factor) which tends to zero in the limit of static JT deformation of E_g symmetry. This behaviour is imposed by the Ham reduction factors in Eq. (5.1-15), as can be seen from Fig. 3.6.

If we conclude random strains of predominantly E_g symmetry in our JT problem, we obtain a similar effect as if the JT coupling to E_g deformations was stronger than the coupling to T_{2g} deformations. The lattice site of the ferrous ion is distorted by the superposition of an E_g static strain (random) and both E_g and T_{2g} dynamical JT deformation. In accordance with Ham's treatment of static strain²⁶, the resulting effect of the E_g static random strains is to reduce the strain coupling coefficient to T_{2g} strain, i.e., V_3 . No suitable theory could be found in the literature or set up by the author

to relate the average strength of the strain field to a random strain reduction factor. This model provides a simple explanation for the consistency of our value for V_2 with the results of Table 5.3 and with the prediction of the cluster model, and accounts for the discrepancy in our value for V_3 when compared with Table 5.3.

It is also remembered that the effect of random strains on the value of V_3 is more severe in this case because the first excited states, Γ_{3g} and Γ_{4g} , couple more strongly to the stress than the ground state. The values of V_2 and V_3 in Table 5.3 have been obtained from the effect of stress on the ground state of the ferrous ion.

Moreover, choosing $\hbar\omega_E = 345 \text{ cm}^{-1}$, i.e., at the peak of the density of states for MgO phonons of E_g symmetry, Fig. 4.1, and using Eqs. (5.2-1), (5.2-2), (5.2-7) and (5.2-15), a range of values for the JT energies can be calculated that satisfies the reduction in the spin-orbit splitting and in the g-factor:

$$(E_{JT})_E = 80 \pm 38 \text{ cm}^{-1}$$

$$3/2(E_{JT})_T = 151 \pm 70 \text{ cm}^{-1}$$

These values for the JT energies correspond to the column of Table 5.2 which satisfies the equalities $\hbar\omega_E = 345 \text{ cm}^{-1}$ and

$\hbar\omega_T = 400 \text{ cm}^{-1}$, as expected from Fig. 4.1.

Chapter 6 summarizes the results and conclusions established in this chapter and the previous chapters.

CHAPTER 6

CONCLUSION

The nearby excited states of Fe^{2+} in MgO have been observed by Raman spectroscopy for the first time. We have identified an A_{1g} impurity mode (185 cm^{-1}) and an electronic transition at $110.5 \pm .8 \text{ cm}^{-1}$ which we associate with the first excited states of the ferrous ion, Γ_{3g} and Γ_{4g} , previously observed by far infrared optical absorption. Three Raman spectra with different input-output polarizations differentiate unambiguously the electronic transitions from the impurity mode transition.

In changing the polarization of the incident laser beam from T_{2g} to E_g polarization, we observe a 1.5 cm^{-1} displacement of the electronic Raman line to 112 cm^{-1} . This is as expected since the only allowed transition in such a case is $\Gamma_{5g} \rightarrow \Gamma_{4g}$. Consequently, we assigned the Γ_{4g} level at 112 cm^{-1} and the Γ_{3g} level at 109 cm^{-1} , making the simple assumption of equal intensity for both transitions $\Gamma_{5g} \rightarrow \Gamma_{3g}$ and $\Gamma_{5g} \rightarrow \Gamma_{4g}$. The 3 cm^{-1} separation between the Γ_{3g} and Γ_{4g} levels is in good agreement with the 3.6 cm^{-1} separation observed by Hjorsberg et al., and fits best our experimental data from the stress experiments.

Three different uniaxial stresses were applied to the MgO samples which produced a shift in the observed electronic

transitions. The stress Hamiltonian has been solved and the energy level splitting have been fitted to the experimental data. Chapter 5 discusses the best fit in detail. From the knowledge of the Ham reduction factors corrected for the JT effect, we extract an accurate value for the strain coupling coefficient to E_g deformation, i.e., $V_2 = 7140 \pm 1800 \text{ cm}^{-1}$. At first sight, the strain coupling coefficient to T_{2g} deformation, i.e., V_3 , seems much too weak to explain both the reduced spin-orbit splitting of the energy levels and the reduced electronic g-factor. Moreover, the value for V_3 does not corroborate the results obtained from other techniques and already published in the literature. This fact is understood when we consider the random strain of predominantly E_g symmetry which has been reported by several authors and gives the 9 cm^{-1} linewidth to the electronic transitions observed. As discussed by Ham, this E_g random strain reduces the effect of the trigonal stress and leads to an apparently reduced value for V_3 without affecting the coefficient V_2 . For this reason, we are not able to provide an estimate for the strain coupling coefficient V_3 . Nevertheless, the value for V_2 leads to an estimate for both JT energies, i.e., $(E_{JT})_E = 80 \text{ cm}^{-1}$ and $3/2(E_{JT})_T = 150 \text{ cm}^{-1}$, as explained in chapter 5.

These more accurate experimental results are essential to substantiate existing and future theories about the JT effect of this transition metal ion. The author would like to point out the lack of experimental results and adequate theories

of random strain in crystals with JT impurities and especially
its influence on the JT effect.

APPENDIX A

It is a simple matter to show that the components of the orbital angular momentum commute with the Hamiltonian H' of the electron-electron interaction. For example, the commutator of L_z and H' is calculated using,

$$\begin{aligned} H' &= \frac{1}{2} \sum_{i \neq j} \frac{e^2}{r_{ij}} , \\ &= \frac{e^2}{2} \sum_{i \neq j} \left[(x_i - x_j)^2 + (y_i - y_j)^2 + (z_i - z_j)^2 \right]^{-1/2} \end{aligned} \quad (A-1)$$

and

$$L_z = -i \sum_j \left(x_j \frac{\partial}{\partial y_j} - y_j \frac{\partial}{\partial x_j} \right) \quad (A-2)$$

The commutator applied to a certain linear combination of determinantal product state Ψ is given by,

$$L_z(H'\Psi) - H'(L_z\Psi)$$

or

$$H'(L_z\Psi) + (L_zH')\Psi - H'(L_z\Psi)$$

which will be zero, i.e., H' and L_z will commute, if the operator L_zH' is shown to be zero. From eq. A-1 and eq. A-2, we obtain after a straight forward calculation,

$$\begin{aligned} L_zH' &= \frac{e^2}{2i} \sum_{k=1}^N \sum_{l \neq k}^N \left[\frac{x_k y_l - y_k x_l}{r_{ik}^3} \right] , \\ &= 0 . \end{aligned}$$

The same procedure can be followed for the L_x and L_y components of the orbital angular momentum. Since H' contains no spin terms, it commutes trivially with the components of the spin angular momentum.

Defining states which are linear combinations of determinantal functions labeled by the quantum numbers $LSM_L M_S$, we can show that the matrix elements of H' vanish if $M_L \neq M'_L$. The following equalities are satisfied:

$$\begin{aligned} \langle LSM_L M_S | H' | L'S'M'_L M'_S \rangle M'_L \\ &= \langle LSM_L M_S | H' L_z | L'S'M'_L M'_S \rangle \\ &= \langle LSM_L M_S | L_z H' | L'S'M'_L M'_S \rangle \\ &= M_L \langle LSM_L M_S | H' | L'S'M'_L M'_S \rangle \end{aligned}$$

Replacing L_z by either L^2 , S^2 , or S_z , we show similarly that the matrix elements of H' must vanish if $L \neq L'$, $S \neq S'$ or $M_S \neq M'_S$ in the two determinantal functions involved for a particular matrix element.

APPENDIX B

In this Appendix are listed the fifteen spin-orbit functions of the ${}^5T_{2g}$ -states. The functions are different orthonormal linear combinations of the spinors defined by Eq. (2.3-9), i.e.,

$$\left[|\xi; s\rangle, |\eta; s\rangle, |\zeta; s\rangle \right]$$

where $S = 2, 1, 0, -1, -2$ is the M_S value. The spin-orbit functions are designated by $Q_i(\Gamma_j)$ where Γ_j refers to the irreducible representation of the spin-orbit states, Eq. (2.3-10), and the subscript i distinguishes the partners of a given irreducible representation. The fifteen spin-orbit functions are:

$$\varphi_1(a\Gamma_{5g}) = \frac{-\sqrt{3}}{2\sqrt{5}} \cdot \left(\left[|\xi 1\rangle - |\eta 1\rangle \right] - \left[|\xi -1\rangle + |\eta -1\rangle \right] \right) + \frac{\sqrt{2}}{\sqrt{5}} \cdot \left(|\xi 0\rangle \right)$$

$$\varphi_2(a\Gamma_{5g}) = \frac{\sqrt{3}}{2\sqrt{5}} \cdot \left(\left[|\xi 2\rangle - |\eta 2\rangle \right] + \left[|\xi -2\rangle + |\eta -2\rangle \right] \right) - \frac{1}{\sqrt{10}} \cdot \left(|\xi 0\rangle \right)$$

$$\varphi_3(a\Gamma_{5g}) = \frac{-\sqrt{3}}{2\sqrt{5}} \cdot \left(\left[|\xi 2\rangle + |\eta 2\rangle \right] - \left[|\xi -2\rangle - |\eta -2\rangle \right] \right) - \frac{1}{\sqrt{10}} \cdot \left(|\eta 0\rangle \right)$$

$$\varphi_1(\Gamma_{3g}) = \frac{1}{2\sqrt{3}} \cdot \left(\left[|\xi 1\rangle - |\eta 1\rangle \right] + \left[|\xi -1\rangle + |\eta -1\rangle \right] \right) + \frac{1}{\sqrt{3}} \cdot \left(|\xi 2\rangle - |\xi -2\rangle \right)$$

$$\varphi_2(\Gamma_{3g}) = \frac{-1}{2} \cdot \left(\left[|\xi 1\rangle + |\eta 1\rangle \right] + \left[|\xi -1\rangle - |\eta -1\rangle \right] \right)$$

$$\varphi_1(a \sqrt{4g}) = \frac{1}{2\sqrt{3}} \left(-[|\xi 1\rangle + |\eta 1\rangle] + [|\xi -1\rangle - |\eta -1\rangle] \right) \frac{-1}{\sqrt{3}} (|\zeta 2\rangle + |\zeta -2\rangle)$$

$$\varphi_2(a \sqrt{4g}) = \frac{1}{2\sqrt{3}} \left([|\xi 2\rangle - |\eta 2\rangle] - [|\xi -2\rangle + |\eta -2\rangle] + [|\zeta 1\rangle + |\zeta -1\rangle] \right) \frac{-1}{\sqrt{2}} (|\eta 0\rangle)$$

$$\varphi_3(a \sqrt{4g}) = \frac{1}{2\sqrt{3}} \left([|\xi 2\rangle - |\eta 2\rangle] + [|\xi -2\rangle + |\eta -2\rangle] + [|\zeta 1\rangle - |\zeta -1\rangle] \right) \frac{+1}{\sqrt{2}} (|\xi 0\rangle)$$

$$\varphi(\sqrt{1g}) = \frac{-1}{\sqrt{6}} \left([|\xi 1\rangle - |\eta 1\rangle] + [|\xi -1\rangle + |\eta -1\rangle] - [|\zeta 2\rangle - |\zeta -2\rangle] \right)$$

$$\varphi_1(b \sqrt{4g}) = \frac{1}{\sqrt{6}} \left([|\xi 1\rangle + |\eta 1\rangle] - [|\xi -1\rangle - |\eta -1\rangle] - [|\zeta 2\rangle + |\zeta -2\rangle] \right)$$

$$\varphi_2(b \sqrt{4g}) = \frac{1}{2\sqrt{6}} \left([|\xi 2\rangle + 2|\eta 2\rangle] + [|\xi -2\rangle - 2|\eta -2\rangle] - 2[|\zeta 1\rangle - |\zeta -1\rangle] \right) \frac{+1}{2} (|\xi 0\rangle)$$

$$\varphi_3(b \sqrt{4g}) = \frac{-1}{2\sqrt{6}} \left([2|\xi 2\rangle - |\eta 2\rangle] - [2|\xi -2\rangle + |\eta -2\rangle] + 2[|\zeta 1\rangle + |\zeta -1\rangle] \right) \frac{-1}{2} (|\eta 0\rangle)$$

$$\varphi_1(b \sqrt{5g}) = \frac{1}{\sqrt{10}} \left([|\xi 1\rangle - |\eta 1\rangle] - [|\xi -1\rangle + |\eta -1\rangle] \right) + \frac{\sqrt{3}}{\sqrt{5}} (|\zeta 0\rangle)$$

$$\varphi_2(b \sqrt{5g}) = \frac{1}{2\sqrt{10}} \left([3|\xi 2\rangle + 2|\eta 2\rangle] + [3|\xi -2\rangle - 2|\eta -2\rangle] + 2[|\zeta 1\rangle - |\zeta -1\rangle] \right) - \frac{\sqrt{3}}{2\sqrt{5}} (|\xi 0\rangle)$$

$$\varphi_3(b \sqrt{5g}) = \frac{1}{2\sqrt{10}} \left([2|\xi 2\rangle - 3|\eta 2\rangle] - [2|\xi -2\rangle + 3|\eta -2\rangle] - 2[|\zeta 1\rangle + |\zeta -1\rangle] \right) - \frac{\sqrt{3}}{2\sqrt{5}} (|\eta 0\rangle)$$

APPENDIX C

It must be shown that we can neglect the second-order terms in the Taylor expansion of the Coulomb energy of interaction between the i^{th} electron and the ligands, Eq. (3.1-1). We can combine the first-order and second-order terms in Eq. (3.1-1) so as to obtain,

$$V'(r, Q) = V'_{0h}(r, 0) + \frac{1}{2} \sum_N \frac{\partial}{\partial Q_N} \left[V' + \sum_M \left(\frac{\partial V'}{\partial Q_M} \right) Q_M \right] Q_N + \dots \quad (\text{C-1})$$

The expression (C-1) can be rewritten using Eq. (3.1-5). The right hand side term becomes,

$$\sum_N \left(- \sum_{\lambda, X} 4\pi \cdot \frac{\lambda+1}{2\lambda+1} \cdot \frac{r_i}{R_0^{\lambda+2}} \cdot Y_{\lambda, X} \sum_k c_k^N \left[a_k - \frac{1}{2} \sum_{k'} a_{k'} \sum_M (\lambda+2) c_{k'}^M \frac{Q_M}{R_0} \right] \right) \quad (\text{C-2})$$

We see that the second-order terms in Eq. (3.1-1) result in a correction to Eq. (3.1-5). The correction terms involve the ratio Q_M/R_0 which is smaller than 0.01 for weak JT coupling, as calculated from Eq. (3.2-2). The whole correction is smaller than 1% and, therefore, can be neglected since larger errors are expected from the cluster model.

More commonly occurring Tesseral harmonics :

$$Z_{20} = \frac{1}{4} \left(\frac{5}{\pi} \right)^{1/2} [(3z^2 - r^2)/r^2]$$

$$Z_{22}^C = \frac{1}{4} \left(\frac{15}{\pi} \right)^{1/2} [(x^2 - y^2)/r^2]$$

$$Z_{40} = \frac{3}{16} \left(\frac{1}{\pi} \right)^{1/2} [(35z^4 - 30z^2r^2 + 3r^4)/r^4]$$

$$Z_{42}^C = \frac{3}{8} \left(\frac{5}{\pi} \right)^{1/2} [(7z^2 - r^2)(x^2 - y^2)/r^4]$$

$$Z_{43}^C = \frac{3}{8} \left(\frac{70}{\pi} \right)^{1/2} [z(x^3 - 3xy^2)/r^4]$$

$$Z_{43}^S = \frac{3}{8} \left(\frac{70}{\pi} \right)^{1/2} [z(3x^2y - y^3)/r^4]$$

$$Z_{44}^C = \frac{3}{16} \left(\frac{35}{\pi} \right)^{1/2} [(x^4 - 6x^2y^2 + y^4)/r^4]$$

$$Z_{44}^S = \frac{3}{16} \left(\frac{35}{\pi} \right)^{1/2} [4(x^3y - y^3x)/r^4]$$

$$Z_{n0} = Y_{n0}$$

$$\left. \begin{aligned} Z_{nm}^C &= (1/\sqrt{2}) [Y_{n-m} + (-1)^m Y_{nm}] \\ Z_{nm}^S &= (i/\sqrt{2}) [Y_{n-m} - (-1)^m Y_{nm}] \end{aligned} \right\} m > 0$$

APPENDIX D

The Ham reduction factors, K_E and K_T , as defined in Chapter 3, are perturbed by the JT interaction between the no-phonon states and the one-phonon states. Only the reduction factors corresponding to the $J = 1$ and $J = 2$ spin-orbit states are considered since the $J = 3$ levels are not observed experimentally. Chapter 3 gives the guidelines to the perturbation calculations. The perturbed reduction factors are:

(i) $J = 1$ (a_{1g} level)

$$K_E(1) = \frac{1}{10} + \chi_E G_1(\xi, \omega_E) + \chi_T G_2(\xi, \omega_T)$$

$$K_T(1) = \frac{1}{10} + \chi_E G_2(\xi, \omega_E) + \chi_T G_3(\xi, \omega_T)$$

(ii) $J = 2$ (Γ_{3g} , a_{4g} levels)

$$K_E(2) = \frac{-1}{3} \left[\frac{1}{2} + \chi_E G_4(\xi, \omega_E) + \chi_T G_5(\xi, \omega_T) \right]$$

$$K_T(2) = \frac{-1}{3} \left[\frac{1}{2} + \chi_E G_5(\xi, \omega_E) + \chi_T G_6(\xi, \omega_T) \right]$$

The following definitions are used:

$$\chi_E = (E_{JT})_E / \hbar \omega_E$$

$$\chi_T = 3(E_{JT})_T / 2\hbar \omega_T$$

$$G_1(s, \omega) = \frac{1}{1000} + \frac{3}{40} U_{22} + \frac{27}{125} U_{55} - \frac{24}{125} U_{25} + \frac{27}{125} V_{25}$$

$$G_2(s, \omega) = \frac{-1}{2000} + \frac{3}{80} U_{22} + \frac{24}{125} U_{55} - \frac{279}{1000} U_{25} + \frac{117}{1000} V_{25}$$

$$G_3(s, \omega) = \frac{1}{2000} + \frac{1}{16} U_{22} + \frac{26}{125} U_{55} - \frac{221}{1000} U_{25} + \frac{183}{1000} V_{25}$$

$$G_4(s, \omega) = \frac{1}{2} R_{23} - S_{23}$$

$$G_5(s, \omega) = \frac{-1}{16} + \frac{3}{400} R_{22} - \frac{2}{25} R_{55} - \frac{23}{200} R_{23} - \frac{5}{8} S_{23}$$

$$G_6(s, \omega) = \frac{-1}{48} + \frac{1}{400} R_{22} - \frac{2}{75} R_{55} + \frac{59}{200} R_{23} - \frac{7}{8} S_{23}$$

where

$$U_{22} = (\kappa\omega)^2 / (\kappa\omega + 2s)^2$$

$$U_{55} = (\kappa\omega)^2 / (\kappa\omega + 5s)^2$$

$$U_{25} = (\kappa\omega)^2 / (\kappa\omega + 2s)(\kappa\omega + 5s)$$

$$V_{25} = s\kappa\omega / (\kappa\omega + 2s)(\kappa\omega + 5s)$$

$$R_{22} = (\kappa\omega)^2 / (\kappa\omega - 2s)^2$$

$$R_{33} = (\kappa\omega)^2 / (\kappa\omega + 3s)^2$$

$$R_{23} = (\kappa\omega)^2 / (\kappa\omega - 2s)(\kappa\omega + 3s)$$

$$S_{23} = s\kappa\omega / (\kappa\omega - 2s)(\kappa\omega + 3s)$$

APPENDIX E

In this Appendix are given the different Raman intensity matrices, as mentioned in subsection 4.3.2. London⁷³ calculated the Raman scattering tensors for crystals of O_h symmetry. The corresponding Raman intensity matrices for crystals having their symmetry axis $[001]$, $[010]$ and $[100]$ aligned with the laboratory frame of reference Z, Y and X, respectively, are obtained by squaring the elements of the Raman scattering tensors calculated by London, i.e.,

$$\begin{array}{ccc}
 \begin{bmatrix} 1 & 0 & 0 \\ 0 & 1 & 0 \\ 0 & 0 & 1 \end{bmatrix} & \begin{bmatrix} 1 & 0 & 0 \\ 0 & 1 & 0 \\ 0 & 0 & 4 \end{bmatrix} & \begin{bmatrix} 0 & 1 & 1 \\ 1 & 0 & 1 \\ 1 & 1 & 0 \end{bmatrix} \\
 A_{1g} & E_g & T_{2g} \quad (E-1)
 \end{array}$$

Knowing the scattering geometry, we obtain the irreducible representation of the scattering tensor with the help of Eq. (4.3-2). From (E-1), we obtain:

$$\begin{array}{l}
 Z(YY)X \longrightarrow A_{1g} + E_g \\
 Z(XY)X \longrightarrow T_{2g}
 \end{array}$$

Now, if the $[100]$ and $[011]$ axes of the crystal are aligned with the Z and Y axes of the laboratory frame of reference, (E-1) must be transformed accordingly by choosing the proper linear combination of elements of the Raman scattering tensors. So, $ZY \rightarrow x(y+z) = zy + xz$, where x, y, z belongs

to the crystal frame of reference. Consequently, the new elements R_{zy} of the Raman scattering tensor is given by a linear combination $R_{xy} + R_{xz}$ of the London's Raman scattering tensors.

In the following are given the Raman intensity matrices appropriate for the crystal orientations of Figs. 5.4 to 5.6:

$$(i) [110] \rightarrow Z, [001] \rightarrow Y, [\bar{1}\bar{1}0] \rightarrow X$$

$$\begin{bmatrix} 1 & 0 & 0 \\ 0 & 1 & 0 \\ 0 & 0 & 1 \end{bmatrix}$$

 A_{1g}

$$\begin{bmatrix} 1 & 0 & 3 \\ 0 & 4 & 0 \\ 3 & 0 & 1 \end{bmatrix}$$

 E_g

$$\begin{bmatrix} 1 & 1 & 0 \\ 1 & 0 & 1 \\ 0 & 1 & 1 \end{bmatrix}$$

 T_{2g}

$$Z(YY)X \rightarrow A_{1g} + 4E_g ; Z(XY)X \rightarrow T_{2g}$$

$$(ii) [11\bar{2}] \rightarrow Z, [111] \rightarrow Y, [\bar{1}\bar{1}0] \rightarrow X$$

$$\begin{bmatrix} 1 & 0 & 0 \\ 0 & 1 & 0 \\ 0 & 0 & 1 \end{bmatrix}$$

 A_{1g}

$$\begin{bmatrix} 1 & 2 & 1 \\ 2 & 0 & 2 \\ 1 & 2 & 1 \end{bmatrix}$$

 E_g

$$\begin{bmatrix} 1 & 1/3 & 2/3 \\ 1/3 & 4/3 & 1/3 \\ 2/3 & 1/3 & 1 \end{bmatrix}$$

 T_{2g}

$$Z(YY)X \rightarrow A_{1g} + 4/3 T_{2g} ; Z(XY)X \rightarrow 2E_g + 1/3 T_{2g}$$

$$(iii) [100] \rightarrow Z, [011] \rightarrow Y, [0\bar{1}1] \rightarrow X$$

$$\begin{bmatrix} 1 & 0 & 0 \\ 0 & 1 & 0 \\ 0 & 0 & 1 \end{bmatrix}$$

 A_{1g}

$$\begin{bmatrix} 1 & 3 & 0 \\ 3 & 1 & 0 \\ 0 & 0 & 4 \end{bmatrix}$$

 E_g

$$\begin{bmatrix} 1 & 0 & 1 \\ 0 & 1 & 1 \\ 1 & 1 & 0 \end{bmatrix}$$

 T_{2g}

$$Z(YY)X \rightarrow A_{1g} + E_g + T_{2g}; \quad Z(XY)X \rightarrow 3E_g$$

$$(iv) [11\bar{2}] \rightarrow Z, [1\bar{1}0] \rightarrow Y, [111] \rightarrow X$$

$$\begin{bmatrix} 1 & 0 & 0 \\ 0 & 1 & 0 \\ 0 & 0 & 1 \end{bmatrix}$$

 A_{1g}

$$\begin{bmatrix} 1 & 1 & 2 \\ 1 & 1 & 2 \\ 2 & 2 & 0 \end{bmatrix}$$

 E_g

$$\begin{bmatrix} 1 & 2/3 & 1/3 \\ 2/3 & 1 & 1/3 \\ 1/3 & 1/3 & 4/3 \end{bmatrix}$$

 T_{2g}

$$Z(YY)X \rightarrow A_g + E_g + T_{2g}; \quad Z(XY)X \rightarrow E_g + 2/3 T_{2g}$$

APPENDIX F

In this Appendix is shown how to calculate the splitting of the spin-orbit energy levels in the presence of uniaxial stress. The stress Hamiltonian, Eq. 5.1-15, is solved for the three different types of strain, i.e., tetragonal, trigonal and orthorhombic strain represented by Figs. 5-1 to 5-3, respectively.

The tetragonal strain

When an external pressure is applied along the $[100]$ -axis of the $\text{MgO}:\text{Fe}^{2+}$ sample, Fig. 5.1, a tetragonal strain occurs which lifts partially the orbital degeneracies of the energy levels prior to the deformation, see Table 5.1. The resulting splitting of the energy levels is calculated from the stress Hamiltonian for tetragonal strain

$$H^S(D_{4h}) = V_2 K_E (e_e/2) (3J_z^2 - J(J+1)) \quad (\text{F-1})$$

where the definition of the electronic operator, E_e , Eq. (3.1-10a), has been used. In the spin-orbit states, we must solve a secular determinant for each value of J . In agreement with Table 5.1, we obtain the following energy levels:

$$(i) \quad J = 1$$

$$\Gamma_{4g}: \quad -3\zeta + 9\mu + \frac{27}{5}\rho - K_E^{(1)} V_2 e_e \quad (\text{F-2a})$$

$$\Gamma_{5g}: \quad -3\zeta + 9\mu - \frac{27}{5}\rho + K_E^{(1)} V_2 \frac{e_e}{2} \quad (\text{F-2b})$$

(ii) $J = 2$

$$\Gamma_{1g}: -\zeta + \mu + 2\rho + 3K_E^{(2)}V_2 e_\theta \quad (\text{F-2c})$$

$$\Gamma_{3g}: -\zeta + \mu + 2\rho - 3K_E^{(2)}V_2 e_\theta \quad (\text{F-2d})$$

$$\Gamma_{2g}: -\zeta + \mu + 3\rho + 3K_E^{(2)}V_2 e_\theta \quad (\text{F-2e})$$

$$\Gamma_{5g}: -\zeta + \mu + 3\rho - 3K_E^{(2)}V_2 \frac{e_\theta}{2} \quad (\text{F-2f})$$

where the Ham reduction factors $K_E(J)$ are given in Appendix D. In section 5.3, these energy levels are used to fit the experimental results presented in Chapter 4.

The trigonal strain

A uniaxial force applied along the $[111]$ -axis of the MgO:Fe^{2+} sample, Fig. 5.2, causes a trigonal deformation of the lattice which lifts partially the degeneracy of the energy levels prior to the deformation, but leaves the Γ_{3g} level unsplit. The resulting splitting of the energy levels is calculated using the stress Hamiltonian for trigonal strain,

$$H^S(D_{3d}) = V_3 K_T (e_\xi (J_y J_z + J_z J_y) + e_\eta (J_z J_x + J_x J_z) + e_\zeta (J_x J_y + J_y J_x))$$

which can be rewritten in a more tractable form using the

raising and lowering operators,

$$H^S(D_{3d}) = V_3 K_T \frac{e(T_2)}{2i^2} (J_+^2 - J_-^2 + (1+i)(J_+ J_z + J_z J_+) + (i-1)(J_- J_z + J_z J_-)) \quad (F-3)$$

where we have used $e(T_2) = e_{\xi} = e_{\eta} = e_{\zeta}$, Eq. (5.1-10c) and the definition of the electronic operators T_{ξ} , T_{η} , T_{ζ} , Eqs. (3.1-10c) to (3.1-10e). Again, taking account of the second-order spin-orbit Hamiltonian, we must solve a secular determinant for each value of J which give, in agreement with Table 5.1, the following energy levels:

(i) $J = 1$

$$\Gamma_{1g}: -3\zeta + 9\mu + \frac{27}{5}\rho - 2K_T(1)V_3 e(T_2) \quad (F-4a)$$

$$\Gamma_{3g}: -3\zeta + 9\mu + \frac{27}{5}\rho + K_T(1)V_3 e(T_2) \quad (F-4b)$$

(ii) $J = 2$

$$\Gamma_{3g}: -\zeta + \mu + 3\rho - \frac{1}{4} \left(\beta + 2\rho + [(\beta - 2\rho)^2 + 8\beta^2]^{1/2} \right) \quad (F-4c)$$

$$\Gamma_{3g}: -\zeta + \mu + 3\rho - \frac{1}{4} \left(\beta + 2\rho - [(\beta - 2\rho)^2 + 8\beta^2]^{1/2} \right) \quad (F-4d)$$

$$\Gamma_{2g}: -\zeta + \mu + 3\rho - 6K_T(2)V_3 e(T_2) \quad (F-4e)$$

where $\beta = 6K_T(2)V_3 e(T_2)$. We observe that the stress Hamiltonian makes the two Γ_{3g} states interact and admixes their wavefunctions.

This interaction causes the two doublet energy levels issued from the Γ_{3g} and Γ_{4g} levels (O_h symmetry) to repel each other. Eventually, the singlet state issued from the Γ_{4g} level, Eq. (F-4e), will cross the doublet state Γ_{3g} , Eq. (F-4c), at sufficiently high stress. In fact, this accidental degeneracy is lifted if we account for the matrix elements between these levels and the $J = 1$ states. Again, this correction being small it can be neglected.

The orthorhombic strain

An appropriate stress applied along the $[110]$ -axis of an $MgO:Fe^{2+}$ samples causes a uniform orthorhombic strain, as shown in Fig. 5.3, which lifts completely the orbital degeneracy of all the energy levels considered. The orthorhombic strain is obtained schematically from a tetragonal expansion and a suitable component of a trigonal compression. The resulting splitting of the energy levels is calculated from the stress Hamiltonian for orthorhombic strain

$$H^S(D_{2d}) = K_E V_2 \left(\frac{e}{2} \right) (3J_z^2 - J(J+1)) + K_T V_3 e \left(J_x J_y + J_y J_x \right) \quad (F-5)$$

where the right hand side term can be written alternatively in terms of raising and lowering operators as

$$(J_x J_y + J_y J_x) = (1/2i) (J_+^2 - J_-^2).$$

The orthorhombic stress Hamiltonian and the second-order spin-orbit Hamiltonian are treated simultaneously to yield the following eigenvalues of the secular determinant for each value of J:

$$(i) \quad J = 1$$

$$\Gamma_{2g}: \quad -3\zeta + 9\mu + \frac{27}{5}\rho - K_E(1)V_2 e_0 \quad (F-6a)$$

$$\Gamma_{3g}: \quad -3\zeta + 9\mu + \frac{27}{5}\rho + K_E(1)V_2 \frac{e_0}{2} - K_T(1)V_3 e_\zeta \quad (F-6b)$$

$$\Gamma_{4g}: \quad -3\zeta + 9\mu + \frac{27}{5}\rho + K_E(1)V_2 \frac{e_0}{2} - K_T(1)V_3 e_\zeta \quad (F-6c)$$

$$(ii) \quad J = 2$$

$$\Gamma_{1g}: \quad -\zeta + \mu + 2\rho + 3K_E(2)V_2 e_0 \quad (F-6d)$$

$$\Gamma_{1g}: \quad -\zeta + \mu + \frac{5}{2}\rho - \frac{1}{2} \left[\rho^2 - 2\alpha \left(\rho - \frac{\alpha}{2} \right) + \frac{4}{3}\beta^2 \right]^{1/2} \quad (F-6e)$$

$$\Gamma_{2g}: \quad -\zeta + \mu + \frac{5}{2}\rho + \frac{1}{2} \left[\rho^2 - 2\alpha \left(\rho - \frac{\alpha}{2} \right) + \frac{4}{3}\beta^2 \right]^{1/2} \quad (F-6f)$$

$$\Gamma_{3g}: \quad -\zeta + \mu + 3\rho - 3K_E(2)V_2 \frac{e_0}{2} + 3K_T(2)V_3 e_\zeta \quad (F-6g)$$

$$\Gamma_{4g}: \quad -\zeta + \mu + 3\rho - 3K_E(2)V_2 \frac{e_0}{2} - 3K_T(2)V_3 e_\zeta \quad (F-6h)$$

where $\alpha = 6K_E(2)V_2 e_0$ and $\beta = 6K_T(2)V_3 e_\zeta$. In this case, we see that the Γ_{1g} level, Eq. (F-6e), issued from the Γ_{3g} level (0_h)

interacts with the Γ_{2g} level, Eq. (F-6f), issued from the Γ_{4g} level (O_h) and, effectively, repel each other.

It is interesting to note, as mentioned in subsection 4.4.2, that the energy levels preserve their center of gravity^{??} when split by either of the three different strain in the crystal if the split energy levels do not interact between them.

REFERENCES

- 1 A. Abragam and M.H.L. Pryce, Proc. Roy. Soc. A205, 135 (1951)
- 2 W. Low and M. Weger, Phys. Rev. 118, 1119 and 1130 (1960)
- 3 S. Sugano, Y. Tanabe and H. Kamimura, "Multiplets of Transition Metal Ions in Crystals", AP, 1970
- 4 Y. Tanabe and S. Sugano, J. Phys. Soc. Jpn. 2, 766 (1954)
- 5 C. Cohen-Tannoudji, B. Diü and F. Lalöë, "Mécanique Quantique", Hermann, 1973
- 6 W. Low, "Paramagnetic Resonance in Solids", Academic Press, N.Y., 1960
- 7 J. Kanamori, Progr. Theoret. Phys. (Kyoto) 17, 197 (1957)
- 8 M.H.L. Pryce, Phys. Rev. 80, 1107 (1950)
- 9 G.F. Koster, J.O. Dimmok, R.G. Wheeler and H. Statz, "Properties of the Thirty-Two Points Groups", M.I.T. Press, Cambridge, 1963
- 10 M. Born and J.R. Oppenheimer, Ann. Physik 84, 457 (1927)
- 11 H.A. Jahn and E. Teller, Proc. Roy. Soc. A161, 220 (1937)

References

- 12 H.A. Jahn, Proc. Roy. Soc. A164, 117 (1938)
- 13 J.H. Van Vleck, J. Chem. Phys. 7, 61 and 72 (1939)
- 14 J.H. Van Vleck, Phys. Rev. 57, 426 (1940)
- 15 J.C. Sloncjewski, Phys. Rev. 131, 1596 (1963)
- 16 J. des Cloizeaux, Phys. Rev. 129, 554 (1963)
- 17 P. Steggles, J. Phys. C 10, 2817 (1977)
- 18 M.C.M. O'Brien, J. Phys. C 5, 2045 (1972)
- 19 B. Halperin and R. Englman, J. Phys. C 8, 3975 (1975)
- 20 K.W.H. Stevens, Proc. Phys. Soc. (London) A65, 209
(1952)
- 21 E.P. Wigner, "Gruppentheorie", Vieweg, Braunschweig,
1931
- 22 C. Eckart, Rev. Mod. Phys. 2, 305 (1930)
- 23 M. Bacci, Phys. Stat. Sol. B92, 193 (1979)
- 24 C.J. Ballhausen and J. de Heer, J. Chem. Phys. 43,
4304 (1965)
- 25 A.D. Liehr, J. Phys. Chem. 67, 389 and 471 (1963)
- 26 F.S. Ham, Phys. Rev. A138, 1727 (1965)

References

- 27 B.R. Judd, Can. J. Phys. 52, 999 (1974)
- 28 U. Opik and M.H.L. Pryce, Proc. Roy. Soc. A238, 425 (1957)
- 29 M.C.M. O'Brien, J. Phys. C4, 2524 (1971)
- 30 N. Sakamoto and S. Muramatsu, Phys. Rev. B17, 868 (1978)
- 31 C.A. Bates, Phys. Rep. 35C, 187 (1977)
- 32 J.H. Van Vleck, Physica 26, 544 (1960)
- 33 J.H. Van Vleck, Discussions Faraday Soc. 26, 98 (1958)
- 34 K.W.H. Stevens, Proc. Roy. Soc. A219, 542 (1953)
- 35 F.S. Ham, W.M. Schwarz and M.C.M. O'Brien, Phys. Rev. 185, 548 (1969)
- 36 J. Owen and K.W.H. Stevens, Nature (London) 171, 836 (1953)
- 37 M.T. Hutchings, Solid State Physics 16, 227 (1964)
- 38 K.W.H. Stevens, Proc. Phys. Soc. (London) A65, 209 (1952)
- 39 M. Tinkham, "Group Theory and Quantum Mechanics", McGraw-Hill, 1964
- 40 P. Meyer, M. Regis and Y. Farge, Phys. Lett. 48A, 41 (1974)

References

- 41 J.Y. Wong and A.L. Schawlow, Bull. Am. Phys. Soc. 12, 655(1967)
- 42 J.Y. Wong, Phys. Rev. 168, 337 (1968)
- 43 A. Hjortsberg, B. Nygren and J.T. Vallin, Solid State Comm. 16, 105 (1974)
- 44 A. Hjortsberg, Ph.D. Thesis, Chalmers University, Sweden, 1975
- 45 N.B. Manson, J.T. Gourley, E.R. Vance, D. Sengupta and G. Smith, J. Phys. & Chem. Solids 37, 1145 (1977)
- 46 D.N. Pipkorn and H.R. Leider, Bull. Am. Phys. Soc. 11, 49 (1966)
- 47 F.S. Ham, Phys. Rev. 160, 328 (1967)
- 48 A.M. Stoneham, Proc. Phys. Soc. 89, 909 (1966)
- 49 R. Orbach, Proc. Roy. Soc. (London) A264, 458 (1961)
- 50 H.R. Leider and D.N. Pipkorn, Phys. Rev. 165, 494 (1968)
- 51 R.L. Hartman, E.L. Wilkinson and J.G. Castle, Jr., Bull. Am. Phys. Soc. 12, 642 (1967)
- 52 E.L. Wilkinson, R.L. Hartman and J.G. Castle, Jr., Phys. Rev. 171, 299 (1968)

References

- 53 P.J. King, D.J. Monk and S.G. Oates, J. Phys. C 11, 1067 (1978)
- 54 I.P. Morton and M.F. Lewis, Phys. Rev. B3, 552 (1971)
- 55 B.A. Young and H.J. Stapleton, Phys. Lett. 21, 498 (1966)
- 56 J.P. Mon, J. Phys. (Paris) 26, 611 (1966)
- 57 J.P. Mon, C.R. Acad. Sci. B263, 1018 (1966)
- 58 A. Billat, J.P. Mon and M. Voisin, Phys. Stat. Sol. B67, 335 (1975)
- 59 A. Billat, J.P. Mon and M. Voisin, J. Phys. C 9, 1337 (1976)
- 60 D.H. Martin, Adv. Phys. 14, 39 (1965)
- 61 G. Peckham, Proc. Phys. Soc. 90, 657 (1967)
- 62 M.J.L. Sangster, G. Peckham and D.H. Saunderson, J. Phys. C 3, 1026 (1970)
- 63 D.H. McMahon, Phys. Rev. 134, A128 (1964)
- 64 M.F. Lewis and A.M. Stoneham, Phys. Rev. 164, 271 (1967)
- 65 J. Lange, Phys. Rev. B12, 226 (1975)
- 66 M.M. Abraham, C.T. Butler and Y. Chen, J. Chem. Phys. 55, 3752 (1971)

References

- 67 A.M. Stoneham, J. Phys. C1, 565 (1968)
- 68 S. Guha and L.L. Chase, Phys. Rev. B12, 1658 (1975)
- 69 K. Das Gupta, Phys. Rev. Lett. 3, 38 (1959)
- 70 R.J. Elliot and R. Loudon, Phys. Lett. 3, 189 (1963)
- 71 M. Born and M. Bradburn, Proc. Roy. Soc. A188, 161 (1947)
- 72 J.A. Koningstein, "Introduction to the Theory of the Raman Effect", Reidel, 1972
- 73 R. Loudon, Adv. Phys. 13, 423 (1964)
- 74 H. Poulet, Ann. Phys. (Paris) 10, 908 (1955)
- 75 W.G. Nilson, Phys. Rev. 182, 838 (1969)
- 76 A. Hjortsberg, B. Nigren, J. Vallin and F.S. Ham, Phys. Rev. Lett. 39, 1233 (1972)
- 77 A.A. Kaplyanskii, Opt. Spectr. 16, 557 (1964)
- 78 A.L. Schawlow, A.H. Piksis and S. Sugano, Phys. Rev. 122, 1469 (1961)
- 79 A.E.H. Love, "A Treatise on the Mathematical Theory of Elasticity", Cambridge UP, N.Y. 1927
- 80 K. Marklund and S.A. Mahmouds, Phys. Scripta (Sweden) 3, 75 (1971)

References

- 81 C. Kittel, "Introduction to Solid State Physics",
Wiley 4 ed., 1971
- 82 G.D. Watkins and E. Feher, Bull. Am. Phys. Soc. 7,
29 (1962)
- 83 N.S. Shiren, Bull. Am. Phys. Soc. 7, 29 (1962)
- 84 J. Chappert, A. Misetich, R.B. Frankel and N.A. Blum,
Phys. Rev. B1, 1929 (1970)
- 85 M.D. Sturge, Solid State Phys. 20, 91 (1967)